AN ABSTRACT OF THE DISSERTATION OF

Justin Daniel Hall for the degree of Doctor of Philosophy in Biochemistry & Biophysics presented on May 14, 2010.

Title: Biophysical Basis of Macromolecular Assembly in the Dynein Cargo Attachment Complex.

Abstract approved: _____

Elisar J. Barbar

Cytoplasmic dynein is an ATP-dependent, microtubule-based molecular motor involved in the positioning and trafficking of cellular cargo. The cargo binding sub-domain of dynein contains the natively disordered intermediate chain (IC) and the homodimeric light chains (Tctex1, LC8 and LC7). The structure and stoichiometry of this complex, how the light chains interact with natively disordered IC and the role of the light chains in dynein assembly is not clear. The focus of these studies is to elucidate the interactions between IC and the light chains using dynamical, thermodynamical and structural biophysics techniques.

In chapters 2 and 3 we show changes in LC8 internal dynamics are important for partner binding. Furthermore we show the two binding sites on LC8 are allosteric, with both structural and dynamical changes apparent between binding events. These results demonstrate the importance of protein dynamics in LC8 binding.

In chapter 4 we determined the structure of the IC•Tctex1•LC8 complex and show multivalency between Tctex1 and LC8 results in a 50-fold affinity enhancement for IC binding despite no direct Tctex1•LC8 interaction. Interestingly, a purely entropic 1000-fold binding affinity enhancement exists for a designed IC construct containing two LC8 sites instead of a Tctex1 and LC8 site. These results demonstrate Tctex1 and LC8 multivalency is tailored to fit the association needs of the system instead of maximizing potential binding energy.

In chapter 5 we determine the structure of the IC•LC7 complex and show the LC7 recognition sequence on IC proposed in the literature is wrong, instead the LC7 recognition sequence overlaps residues previously thought to be the IC•IC self-association domain. Furthermore, we show Tctex1 and LC8 have a negligible effect on net IC•LC7 binding affinity, despite evidence that Tctex1 and LC8 affect the nature of the IC•LC7 interaction. Thus this work provides the first atomic-level structure of the IC•LC7 complex, corrects decade long misconceptions about IC•LC7 binding and demonstrates an interconnection between the light chains for IC association.

Individually these results provide detailed descriptions of IC and the light chains; together they strongly suggest the light chains structurally regulate IC assembly into the mature cargo binding sub-domain of dynein.

Biophysical Basis of Macromolecular Assembly in the Dynein Cargo Attachment Complex

by

Justin Daniel Hall

A DISSERTATION

submitted to

Oregon State University

in partial fulfillment of

the requirements for the

degree of

Doctor of Philosophy

Presented May 14, 2010

Commencement June 2011

Doctor of Philosophy dissertation of Justin Daniel Hall presented on May 14, 2010.

APPROVED:

Major Professor, representing Biochemistry & Biophysics

Chair of the Department of Biochemistry & Biophysics

Dean of the Graduate School

I understand that my dissertation will become part of the permanent collection of Oregon State University libraries. My signature below authorizes release of my dissertation to any reader upon request.

Justin Daniel Hall, Author

ACKNOWLEDGEMENTS

First I would like to acknowledge my mentor, Elisar Barbar, for providing me with an unparalleled encouragement to graduate. To my graduate committee members, Joseph Beckman, Larry Daley, Michael Freitag and Christopher Mathews, your help, advice and encouragement along the way has made a huge difference to me, thank you. I would like to thank Mike Schimerlik, for a time you were the only OSU Professor that would support my future, I stayed in science with your help. I thank my collaborators, Yujuan Song, for your personal and professional generosity; P. Andrew Karplus, for your tremendous scientific insights – even when wrong; and Andrea Hall, for your endless help on everything. Thank you.

I would like to thank Rick Faber and Dale Tronrud for distinct but overlapping X-ray crystallographic help. In particular, Rick's laid back approach to X-ray generator repair, and Dale's encyclopedic crystallography knowledge.

I am grateful to my friends for personal and professional help over these five years. Greg Benison, Russell Carpenter, Rick and Stacy Cooley, Camden Driggers, Andrea Hall, Trish Khuu, Sangeet Lal, Hui Nian, Afua Nyarko, Brian Sinnott and Andrea Voth, my network of friends has been my network of support.

I would like to thank my family for their love and patience, Cynthia Lynn Todd for gentle steerage; Sean Hall, for helping me laugh and keep perspective; and Tammy Ayyoub, for so much (mostly solicited) good advice.

Lastly, I would like to acknowledge the American Heart Association, the College of Science Student Travel Award program and the Yerex foundation for financial assistance.

CONTRIBUTION OF AUTHORS

Nathan Pursifull contributed to experiments in Chapter 2. Andrea Hall contributed to experiments and text for Chapter 2 and 3. P. Andrew Karplus contributed to crystallographic analysis and text for Chapter 4 and 5. Yujuan Song contributed to experiments in Chapter 5. Elisar Barbar was involved in the design, analysis and writing of all experiments and chapters.

TABLE OF CONTENTS

TABLE OF CONTENTS (Continued)

Page

TABLE OF CONTENTS (Continued)

LIST OF FIGURES

LIST OF FIGURES (Continued)

LIST OF TABLES

LIST OF APPENDIX FIGURES

LIST OF APPENDIX TABLES

Dedicated to my soulmate, Andrea Hall

I can’t find the way…
to you I owe everything…
where to even start?

Biophysical Basis of Macromolecular Assembly in the Dynein Cargo Attachment Complex

Chapter 1

Introduction

Dyneins are a class of ATP-dependent, microtubule-based molecular motors involved in ciliary/flaggelar motion (axonemal dynein) or transport/positioning of cellular components in eukaryotes (cytoplasmic dynein). In all contexts, dyneins function by holding onto a microtubule on one end, a variable cargo on the opposite end, and then coupling the chemical energy of ATP hydrolysis to the mechanical process of walking along a microtubule track.

Cilia and flagella are organelles capable of producing motility by repetitive episodes of bending, which are powered by axonemal dyneins. During an ATP turnover cycle, adjacent axonemal dynein motors coordinate to bind and move a single microtubule in a concerted direction. The coordinated motion of the microtubule creates a bend in the organelle, which returns to a relaxed state when released in preparation for the next cycle (Brokaw 1972; Sale *et al.* 1977; King 2010). Both cilia and flagella have the same internal arrangement of microtubules and associated axonemal dynein motors; thus, in both cases motion is the product of axonemal dyneins.

Cytoplasmic dynein, referred to simply as dynein here, has multiple cellular roles and is essential in animals. During interphase, dynein is involved in general cellular development and maintenance processes including minus-end directed intracellular transport (Mische *et al.* 2007), and the positioning of organelles (Varma *et al.* 2010). During metaphase, dynein is involved in mitotic spindle assembly and orientation (Echeverri *et al.* 1996), as well as being recruited to the kinetochore complex where it is thought to be involved in initial microtubule attachment (Pfarr *et al.* 1990). During anaphase, dynein is involved in the physical separation of chromosomes (Compton 2000; Yang *et al.* 2007). Consistent with its multiple cellular roles, dynein dysfunction is linked to several human diseases including lissencephaly (Faulkner *et al.* 2000), motor neuron disease (Hafezparast *et al.* 2003; Stokin *et al.* 2006), and male infertility (Zuccarello *et al.* 2008).

Dynein is a multi-protein complex which may be conceptually divided into two functional sub-domains; the first is the microtubule and ATP binding sub-

domain comprising of the heavy chain (HC) (Pfister *et al.* 1984) and the second is the cargo binding sub-domain comprising of the intermediate chain (IC) (Steffen *et al.* 1997), the light intermediate chains (LIC) (Gill *et al.* 1994) and the light chain proteins Tctex1, LC8 and LC7 (Dick *et al.* 1996; King *et al.* 1996; Harrison *et al.* 1998; Bowman *et al.* 1999; Susalka *et al.* 2002) (Figure 1.1).

Cargo attachment to dynein occurs either directly through interaction with proteins in the cargo binding sub-domain, or indirectly through a bridging interaction with an adaptor complex associated with the cargo binding sub-domain. Since the dynein cargo binding sub-domain is central to dynein cargo transport, understanding how it is assembled and regulated is important for understanding the greater process of dynein cargo transport. Our work has therefore been to biophysically characterized IC and the light chain proteins of the cargo binding sub-domain as a step towards understanding dynein mediated cargo transport.

The dynein heavy chain

The dynein HC is an unusually large (4,639 a.a. in *Drosophila melanogaster*) protein. Mutations in *D. melanogaster* HC result in larval lethality (Gepner *et al.* 1996). HC is responsible for the motor activity of dynein as well as containing the ATP and microtubule binding sites. Schematically, HC has an N-terminal domain involved in force generation and linkage to the cargo binding sub-domain (linker), a ring structure formed from six AAA+ domains which contain the ATP binding site (AAA+), and a microtubule-binding domain (MTBD) extending from the AAA+ ring (residues 3,285-3,373 in *D. melanogaster*) (Imamula *et al.* 2007) (Figure 1.2).

The main ATP binding site is the 1st AAA+ domain (Imamula et al. 2007), though domains 2-4 can also bind ATP and may play a regulatory role in ATP hydrolysis (Kon *et al.* 2004; Cho *et al.* 2008). During a mechanical cycle, ATP binding reduces microtubule affinity in the MTBD (Imamula et al. 2007). ATP hydrolysis is associated with motion in the linker domain, followed by ADP

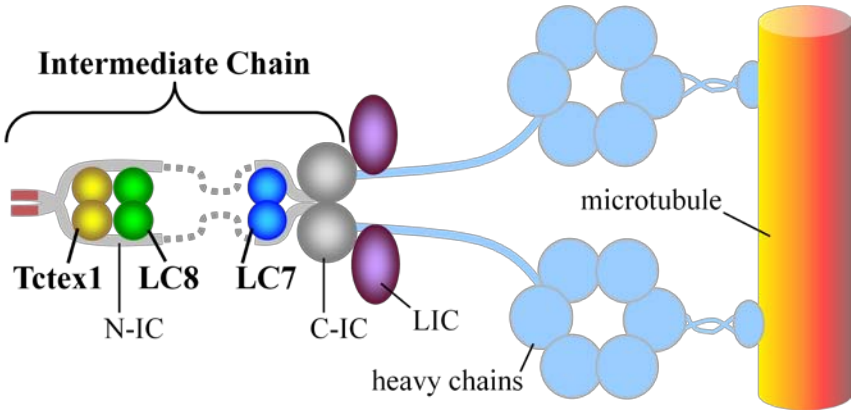

Figure 1.1: Schematic representation of cytoplasmic dynein. Cytoplasmic dynein is shown as an assembly of six proteins: the N-terminal domain of IC (N-IC, grey bars, predicted coiled-coil shown with red hashes, region of unknown structure shown as grey dashes) is natively disordered while the C-terminal domain of IC (C-IC, grey spheres) is predicted to be an ordered toroidal bladed β-propeller; the three homodimeric light chains are Tctex1 (yellow), LC8 (green) and LC7 (blue); the light intermediate chains (LIC, purple) and the heavy chain (light blue) bound to a microtubule (orange). The motor sub-domain of dynein consists of the heavy chain subunits which form a ring of AAA+ domains (Burgess *et al.* 2003) and a microtubule binding domain attached to the AAA+ ring by a flexible 15-nm coiled-coil stalk (Carter *et al.* 2008). The cargo binding sub-domain is comprised of IC (Steffen et al. 1997), LIC, Tctex1, LC8 and LC7 (Bowman et al. 1999; Susalka et al. 2002). Figure adapted from Figure 1 of Hall *et. al* 2009 (Hall *et al.* 2009).

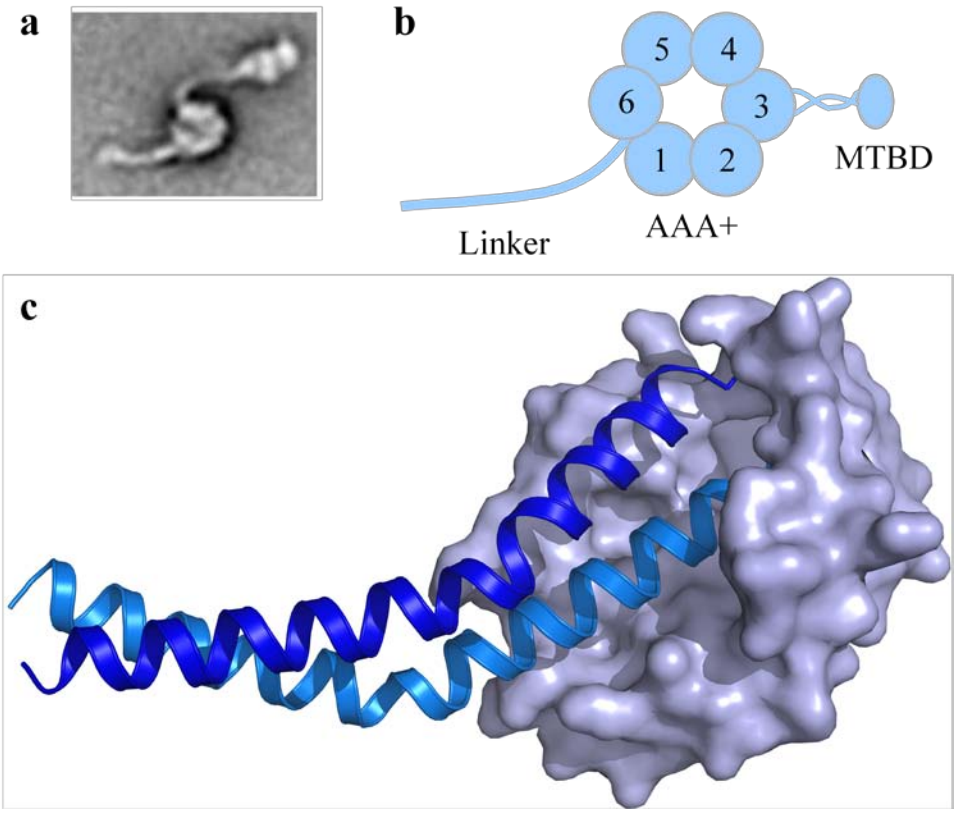

Figure 1.2: The dynein heavy chain. a) Electron microscopic image of the mean conformation of the dynein heavy chain. Image reprinted with permission from Figure 4a of Burgess et al., 2003 (Burgess et al. 2003). b) Schematic representation of the heavy chain (light blue) with the linker, AAA+ and MTBD labeled. c) Structure of the MTBD with coiled-coil 1 (dark blue), coiled-coil 2 (bright blue) and a surface representation of the microtubule binding region (light blue). Images were produced with PyMol (DeLano 2002) using PDB code 3ERR.

into the mechanism by which changes in the AAA+ domain are propagated to the MTBD (Carter et al. 2008) (Fig 1.2c). The MTBD is connected to the AAA+ domain by an anti-parallel coiled-coil, changes in the registry of the coiled-coil modulate the MTBD affinity for the microtubule (Gibbons *et al.* 2005; Kon *et al.* 2009). These results suggest ATP-dependent changes in coiled-coil registry at the AAA+ proximal end could be the mechanism by which microtubule affinity is modulated. Similarly, ATP-dependent structural changes in the AAA+ domain are communicated to the linker connecting HC to the cargo binding sub-domain, though the details of the mechanism are not yet understood (Carter et al. 2008). The linker contains the IC binding site (residues 629-730 in *D. melanogaster*) (Habura *et al.* 1999) and as such provides a link to the cargo binding sub-domain of IC.

The dynein intermediate chain

IC is a medium sized (642 a.a. in *D. melanogaster*) protein. Mutations in *D. melanogaster* IC result in larval lethality (Boylan *et al.* 2002). IC has two structurally distinct regions corresponding to a disordered first half (N-IC, residues 1-289 in *D. melanogaster*) (Makokha *et al.* 2002; Nyarko *et al.* 2004) followed by a predicted toroidal bladed β-propeller (C-IC, residues 290-642 in *D. melanogaster*) (Wilkerson *et al.* 1995; Nurminsky *et al.* 1998). C-IC is the site of binding to the heavy chains (Habura et al. 1999) and N-IC contains the binding sites for multiple proteins including the $p150^{Glued}$ subunit of dynactin (Vaughan *et al.* 1995), an interaction thought to mediate many dynein-related activities including Golgi complex and endosome organization (King *et al.* 2000; Kardon *et al.* 2009), and other proteins presumed to be cellular cargo such as the herpes simplex virus protein (Ye *et al.* 2000), the ClC-2 chloride channel (Dhani *et al.* 2003) and β-catenin (Ligon *et al.* 2001). In addition to these partners, the dynein light chains Tctex1, LC8, and LC7 bind to distinct sites on N-IC (Susalka *et al.* 2000; Makokha et al. 2002). Binding of each of these light chains causes the light

chain recognition sequence on IC to undergo a local disorder-to-order transition (Makokha et al. 2002; Nyarko et al. 2004; Benison *et al.* 2006) to form a β-strand for Tctex1 or LC8 (see Figure 4.3a, chapter 4) (Benison et al. 2007; Williams *et al.* 2007; Hall et al. 2009) or an α-helix for LC7 (see Figure 5.2b, chapter 5) while the rest of N-IC remains disordered.

The dynein light chains Tctex1 and LC8

Tctex1 and LC8 are both small (111 and 89 a.a. in *D. melanogaster*, respectively) homodimeric proteins (Barbar *et al.* 2001; Talbott *et al.* 2006). In *D. melanogaster* Tctex1 mutants result in male sterility (Caggese *et al.* 2001; Li *et al.* 2004) and LC8 null mutants are lethal in late pupal stages (Phillis *et al.* 1996). Despite negligible sequence identity (Figure 1.3), structures of apo-Tctex1 and the nNOS•LC8 complex show Tctex1 and LC8 are paralogs (Liang et al. 1999; Williams *et al.* 2005), with both proteins adopting the same fold with a distinct crossover β-strand (β_3) at the dimer interface (Figure 1.4a, b).

Both Tctex1 and LC8 separately bind to a large number of proteins (fourteen and twenty different partners for Tctex1 and LC8, respectively) (Table 1.1 and 1.2) with approximately 60% of cellular LC8 interacting with non-dynein partners (King et al. 1996); of these partners only IC binds both Tctex1 and LC8. Because they are known to bind within the dynein cargo attachment sub- complex, Tctex1 and LC8 were once presumed to act as cargo adaptors between dynein and their other binding partners. However, structures were determined showing IC binds LC8 at the same site as other LC8 binding partners *(*Benison *et al.* 2007; Williams *et al.* 2007), leading to the suggesting that LC8 regulates partner dimerization instead of acting as cargo adaptors (Barbar 2008). This functional model has been extended to Tctex1 as well, though no structures exist yet for Tctex1 bound to any partner but IC. A regulatory role for Tctex1 and LC8 is supported by evidence that LC8 binding induces IC•IC self-association *in vitro* (Benison et al. 2006), *in vivo* studies showing IC lacking the Tctex1 and LC8

Figure 1.3: Dynein light chain sequences from model organisms. Sequences for a) Tctex1, b) LC8 and c) LC7 are shown for *Homo sapiens* (*Hsa*), *Rattus norvegicus* (*Rno*), *Gallus gallus* (*Gga*), *Xenopus (Silurana) tropicalis* (*Xta*), *Danio rerio* (*Dre*), *Drosophila melanogaster* (*Dme*), *Caenorhabditis elegans* (*Cel*), and *Chlamydomonas reinhardtii* (*Cre*). Identical residues between *Dme* and other organisms are highlighted in yellow. Tctex1, LC8 and LC7 from *Dme* and *Hsa* are 71.4, 96.6 and 81.3% identical, respectively.

Figure 1.3: (*Continued*).

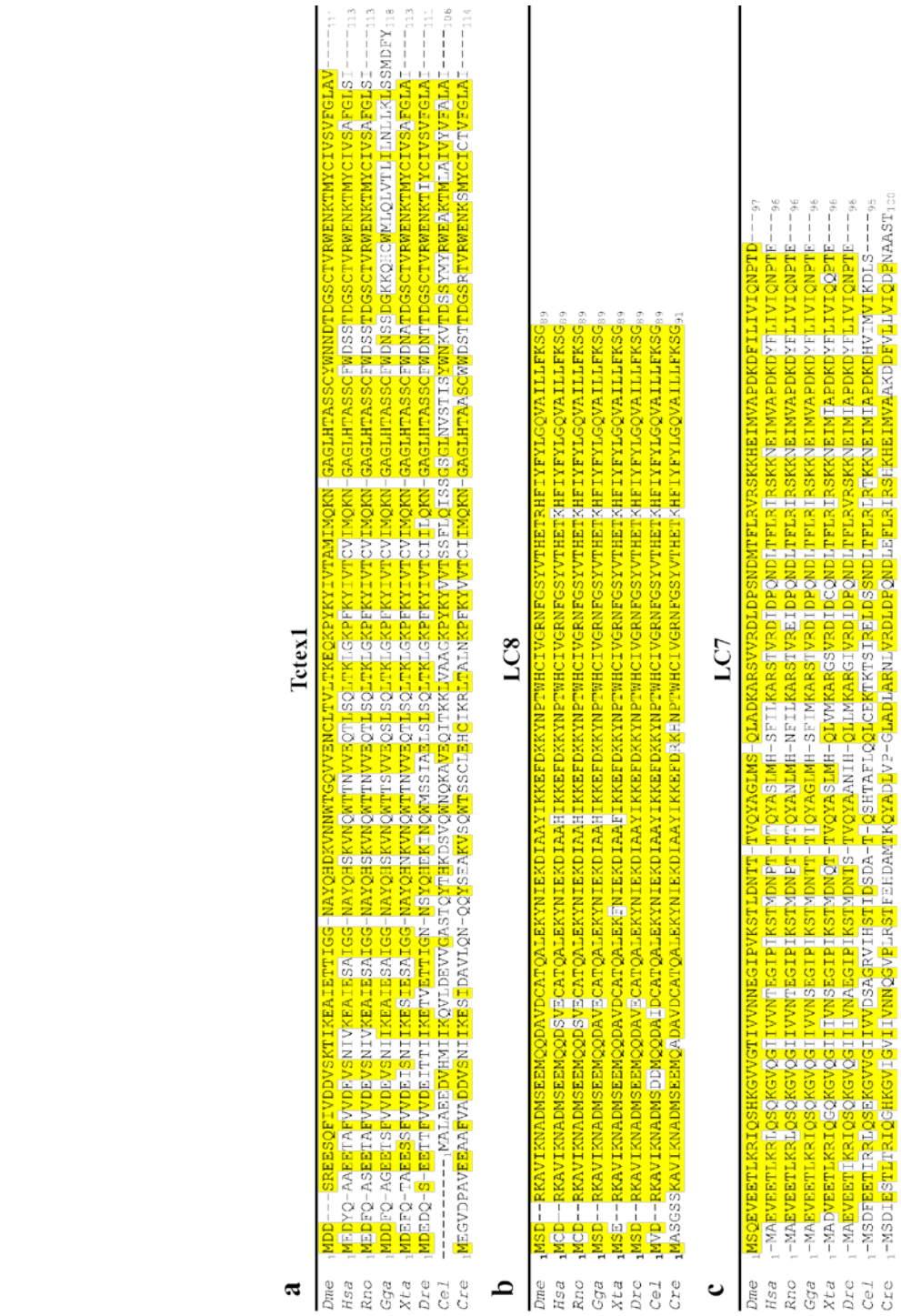

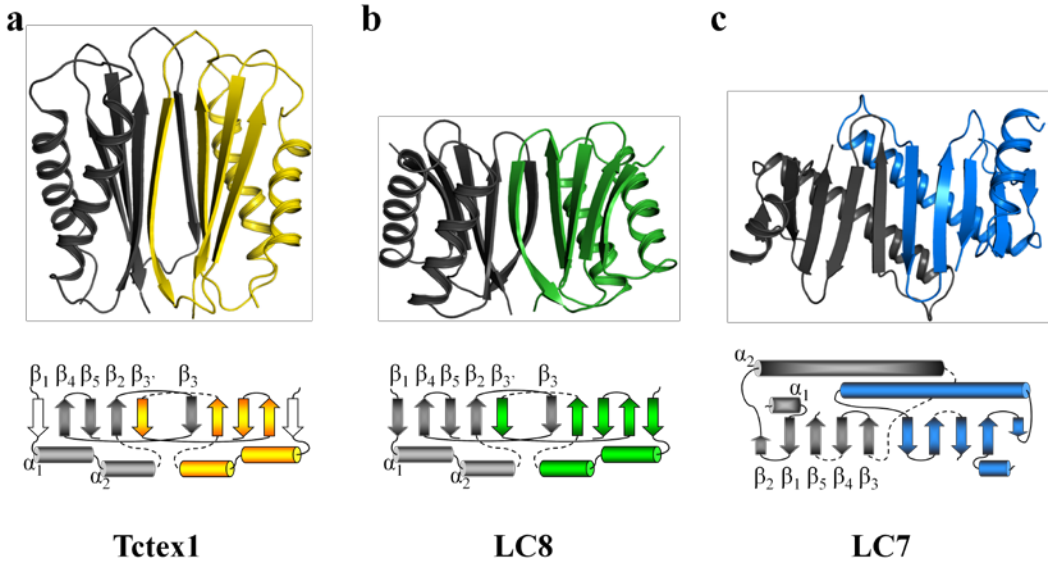

Figure 1.4: Secondary structure and fold of the dynein light chains. Secondary structure (top) and fold (bottom) of a) Tctex1 (yellow), b) LC8 (green) and c) LC7 homodimers with one protomer of each light chain colored grey. β_1 of Tctex1 is involved in non-specific crystallographic contacts in the structure (not shown), but is included in the fold (white) for clarity. Images were produced with PyMol (DeLano 2002) using PDB codes 1YGT, 3BRI and 2HZ5 for Tctex1, LC8 and LC7, respectively.

Table 1.1: Tctex1 and binding partners.

Protein	Method of detection	Role in interaction	Reference
BMPR-II[a]	Y2H[b], CoImm, GST-PD	Phosporylation of Tctex1	Machado, Rudarakachana et al. 2003
CaM-KII	Y2H, CoImm, GST-PD	Dynein transport/unspecified	Bauch, Campbell et al. 1998
CD155	Y2H, CoImm, GST-PD	Dynein transport/unspecified	Mueller, Cao et al. 2002
Doc2	Y2H, CoImm, GST-PD	Dynein transport/unspecified	Nagano, Orita et al. 1998
Fip-1	Y2H, CoImm, GST-PD	Dynein transport/unspecified	Lukashok, Tarassishin et al. 2000
Gβγ	CoImm, GST-PD	Regulation of neurite outgrowth	Sachdev, Menon et al. 2007
IC	Structure - pdb accession 2PG1	IC Dimerization	Harrison, OldsClarke et al. 1997; Williams, Roulhac et al. 2007
p59fyn	Y2H, CoImm, GST-PD	Dynein transport/unspecified	Campbell, Cooper et al. 1998
PTH/PTH-RPR	Y2H, CoImm, GST-PD	Dynein transport/unspecified	Sugai, Saito et al. 2003
Rhodopsin	Y2H, CoImm, GST-PD	Dynein transport/unspecified	Yeh, Peretti et al. 2006
SATB1	Y2H	Dynein transport/unspecified	Yeh, Chuang et al. 2005
Tastin	Y2H, CoImm, GST-PD	Affects Tastin/microtubule adhesion	Nadano, Nakayama et al. 2002
Trk-NR	Y2H, CoImm, GST-PD	Dynein transport/unspecified	Yano, Lee et al. 2001
VDAC	Y2H, CoImm, GST-PD	Affects VDAC channel voltage	Schwarzer, Barnikol-Watanabe et al. 2002

[a]Tctex1 binding protein abbreviations are: bone morphogenetic receptor type II protein (BMPR-II), Ca/calmodulin-dependent kinase II (CaM-KII), the polio virus receptor (CD155), Ad E3-14.7K-interacting protein (Fip-1), G protein beta gamma (Gβγ), tyrosine kinase P59fyn (p59fyn), class B G-protein coupled receptor PTH/PTH-related protein receptor (PTH/PTH-RPR), transcription factor SATB1 (SATB1), the Trk neurotrophin receptors (Trk-NR) and voltage-dependent anion-selective channel (VDAC).

[b]Method abbreviations are: Yeast 2-hybrid (Y2H), coimmunoprecipitation (CoImm) and glutathione S-transferase-pull down (GST-PD).

Table 1.2: LC8 binding partners.

Protein	Method of detection	Role in interaction	Reference
Bim[a]	Structure - pdb accesion 1F95	Regulates proapoptotic activity	Puthalakath, Huang et al. 1999; Fan, Zhang et al. 2001
Dazl	Y2H[b], CoImm, GST-PD	Transports mRNA in male germ cells	Lee, Lee et al. 2006
Egalitarian	Y2H, CoImm	Transports macromolecules to the oocyte	Navarro, Puthalakath et al. 2004
EWG	Y2H, CoImm	Dynein transport/unspecified	Herzig, Andersson et al. 2000
Gephyrin	Y2H, CoImm, GST-PD	Dynein transport/unspecified	Fuhrmann, Kins et al. 2002
IC	Structure - pdb accession 2P2T	IC dimerization	King, Barbarese et al. 1996; Benison, Karplus et al. 2007
IκBα	Y2H, CoImm, GST-PD	Dynein transport/unspecified	Crepieux, Kwon et al. 1997
LV Phosprotein P	Y2H, CoImm	Dynein transport/unspecified	Jacob, Badrane et al. 2000
Myosin Va	NMR titration, GST-pull down,	Myosin Va dimerization	Hodi, Nemeth et al. 2006
nNOS	Structure - pdb accession 1CMI	Transport along axons in neuron cells	Jaffrey and Snyder 1996; Liang, Jaffrey et al. 1999
NRF1	Y2H, CoImm	Dynein transport/unspecified	Herzig, Andersson et al. 2000
Nup159	CoImm, electron microscopy	Nup159 dimerization	Stelter, Kunze et al. 2007
P53-BP	Y2H, CoImm, GST-PD	Transports p53 in response to DNA damage	Lo, Kan et al. 2005
Pak1	Structure - pdb accession 3DVT	Pak1 dimerization	Vadlamudi, Bagheri-Yarmand et al. 2004; Lightcap, Sun et al. 2008
PTH mRNA	CoImm	Dynein transport/unspecified	Epstein, Sela-Brown et al. 2000
Rabies Phosprotein P	Y2H, CoImm	Phosphoprotein P dimerization	Poisson, Real et al. 2001
RasGRP3	Y2H, CoImm, GST-PD	Regulates RasGRP3 subcellular localization	Okamura, Oki-Idouchi et al. 2006
Swa	Structure - pdb accession 3E2B	Bicoid mRNA localization	Schnorrer, Bohmann et al. 2000; Benison, Karplus et al. 2007
Syntaphilin	CoImm, GST-PD	Enhances Syntaphilin•microtuble binding	Chen, Gerwin et al. 2009
TRPS1	Y2H, CoImm, GST-PD	Suppresses transcriptional repression activity	Kaiser, Tavassoli et al. 2003

[a]LC8 binding protein abbreviations are: proapoptotic Bcl2 family protein BimL (Bim), transcription factor EWG (EWG), Lyssavirus phosphoprotein P (LV Phosprotein P), neuronal nitric oxide synthase (nNOS), transcription factor NRF1 (NFR1), yeast nuclear pore complex protein 159 (Nup159), P53 binding protein (P53-BP), p21-activated kinase-1 (Pak1), parathyroid hormone mRNA (PTH mRNA), rabies phosphoprotein P (Rabies Phosprotein P), Ras guanyl-releasing protein (RasGRP3), swallow protein (Swa), transcription factor (TRPS1).

[b]Method abbreviations are: Yeast 2-hybrid (Y2H), coimmunoprecipitation (CoImm) and glutathione S-transferase-pull down (GST-PD).

recognition sequences binds less efficiently to $p150^{Glued}$ (King *et al.* 2003), and that C-IC does not efficiently bind to the dynein heavy chains without the light chain binding sites (Ma *et al.* 1999).

The dynein light chain LC7

LC7 is a small (97 a.a. a.a. in *D. melanogaster*) homodimeric protein. In *D. melanogaster* LC7 mutants are larval lethal (Bowman et al. 1999). X-ray and NMR structures of apo-LC7 from *Homo sapiens* or *Rattus norvegicus* (Ilangovan *et al.* 2005; Song *et al.* 2005; Liu *et al.* 2006) show it is not a paralog of Tctex1 or LC8, but instead belongs to an ancient protein superfamily involved in NTPase regulation (Koonin *et al.* 2000) (Figure 1.4c). In addition to IC, LC7 binds to three other partners: members of the Rab6 family, where LC7 is thought to modulate Rab6 intrinsic GTPase activity (Wanschers *et al.* 2008); the human reduced folate carrier, where LC7 facilitates folate uptake (Ashokkumar *et al.* 2009); and the transforming growth factor-β (TGF-β) receptor complex, where LC7 binding is required for Smad-dependent downstream signaling (Tang *et al.* 2002; Jin *et al.* 2007; Jin *et al.* 2009). No structure of LC7 in complex to IC or its other partners exist, nor are the molecular details of these interactions known, but mutation in LC7 (Ding *et al.* 2005) or changes in LC7 isoform expression levels (Jiang *et al.* 2001) have been observed in ovarian and hepatic cancers suggesting LC7 may have an important cellular role regulating interactions with the TGF-β receptor complex.

Understanding biological observations using biophysical methods

The scientific approach to understanding any process involves experiments in a controlled environment with limited variables; this is not always possible in the complicated environment of an intact cell. Necessarily, *in vitro* methods have been developed to understand *in vivo* observations, where components of a biological system are individually isolated and functions assayed through

hypothesis driven experiments. In this way *in vivo* observations can be tested using *in vitro* methods, and insights from *in vitro* methods can also be applied back to *in vivo* test systems.

To probe protein•protein interactions in the dynein cargo binding sub-domain, I have isolated and characterized proteins using a variety of biochemical and biophysical techniques. In these studies I have used a total of fifteen different protein constructs, the majority of which were already available in the Barbar lab, including wild-type Tctex1, LC8 and LC7, a H55K mutant of LC8 that is an obligate monomer, four synthesized peptides, and seven protein constructs of IC (Figure 1.5). Proteins used were from *D. melanogaster* gene products engineered to contain a His or His-SUMO-tag, and expressed using *Escherichia coli* host cell lines before tag removal. Proteins were initially purified using a nickel-NTA column, and polished using size-exclusion chromatography or high performance liquid chromatography. The three main biophysical techniques used in these studies were nuclear magnetic resonance (NMR) spectroscopy to measure conformational dynamics (Figure 1.6), isothermal titration calorimetry (ITC) to measure thermodynamic association parameters (Figure 1.7), and X-ray crystallography for structure determination (Figure 1.8).

These three techniques can give unique information. For our system, I have used a battery of NMR pulse sequences to probe per residue dynamics on timescales from h to ps. Within these timescales I have characterized motions as small as bond vibrations (ns-ps) or rotamer motions (ns-ms), to larger scale “breathing” motions for entire protein domains (min-h).

While there are many techniques capable of measuring the association strength ($\Delta G°$) between two proteins, ITC is unique in its ability to additionally provide a direct measurement of the enthalpy ($\Delta H°$) and entropy ($-T\Delta S°$) contributions to binding. Access to $\Delta H°$ and $-T\Delta S°$ values invites comparison of thermodynamic parameters between multiple partners, which has provided us with insight into the molecular basis of interactions in our system.

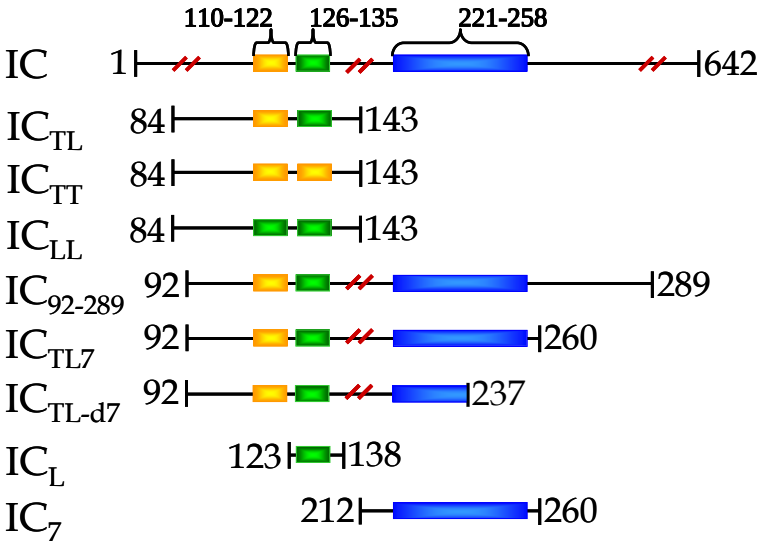

Figure 1.5: IC light chain binding regions and constructs used in these studies. The upper IC diagram locates the binding sites for Tctex1 (yellow), LC8 (blue) and LC7 (blue) with red hashes noting breaks in the sequence. Numbering is relative to amino acids from the *D. melanogaster Cdic*2b genes, subscripts **T**, **L**, **7** and **-d7** stand for **T**ctex1, **L**C8, LC**7** and **d**isrupted LC**7** recognition sequences**,** respectively.

Figure 1.6: Macromolecular NMR spectroscopy can provide information about protein motion on a wide range of timescales. a) Determining residue assignments is the first step in NMR, an HSQC correlating ^{15}N and ^{1}H resonances is shown with each residue resonance already assigned. b) Information on the dynamics of each residue can be determined from pulse sequence-specific time-dependent changes in resonance intensity. A representative curve and best-fit are shown for a single residue in a spin-spin relaxation (T_2) experiment. Motions seen in a T_2 experiment can contain important information on both small and large domain protein motions. c) Large scale "breathing" motions of entire domains often occur on the μs-ms timescale. Chemical exchange rate (R_{ex}) measurements describe protein motions on this timescale, and are determined in part from T_2 experiments. Representative data shown here highlight two regions (residues 5-15 and 63-75) of a protein with large R_{ex} contributions to motion. Panel "a" and "c" are adapted from Figure 5 and 7 of Hall *et al.* 2008 (Hall *et al.* 2008).

Figure 1.6: (*Continued*).

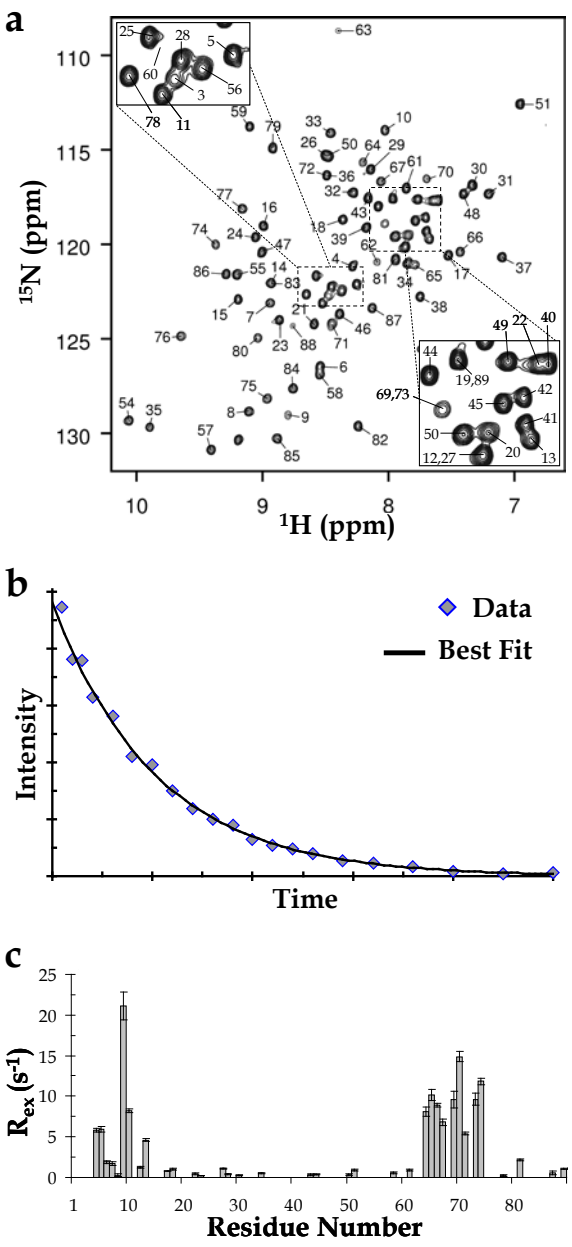

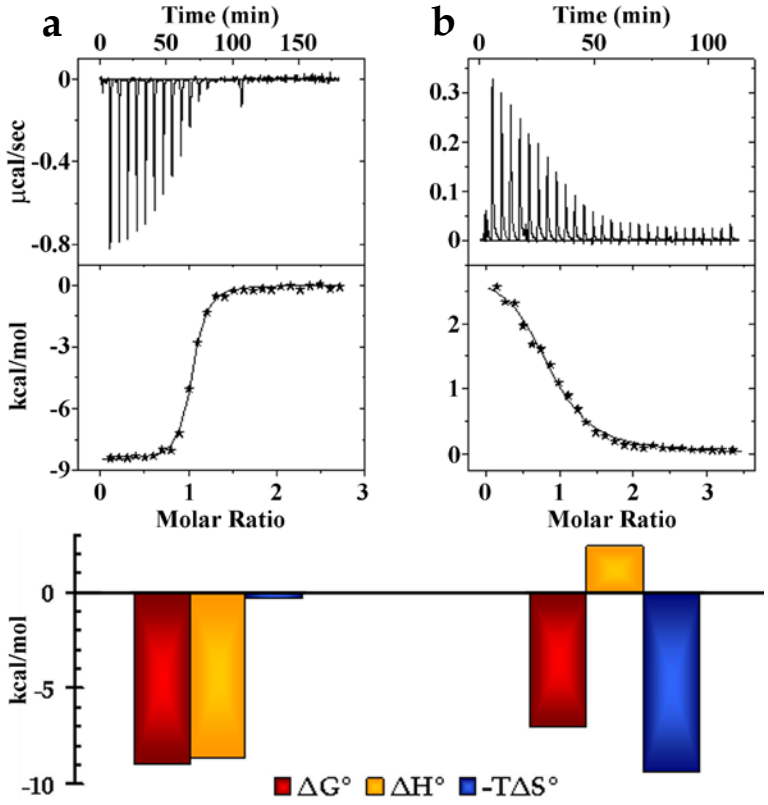

Figure 1.7: ITC can determine the thermodynamic association parameters governing binding. For proteins that bind multiple partners, changes in enthalpy (ΔH°) or entropy (-TΔS°) can provide valuable insight into the nature of the interactions governing binding, particularly for partners with similar binding affinities (ΔG°). a) Representative ITC data with binding isotherms (top panel), integrated heats (middle panel) and complete thermodynamic association parameters (bottom panel) for LC8 binding to peptides from Swa and b) nNOS at 10 °C. Though both have similar overall affinity at these conditions, Swa binding is exothermic and enthalpically driven (ΔH° = -8.6 kcal/mol), while nNOS binding is endothermic and entropically driven (-TΔS° = -9.4 kcal/mol).

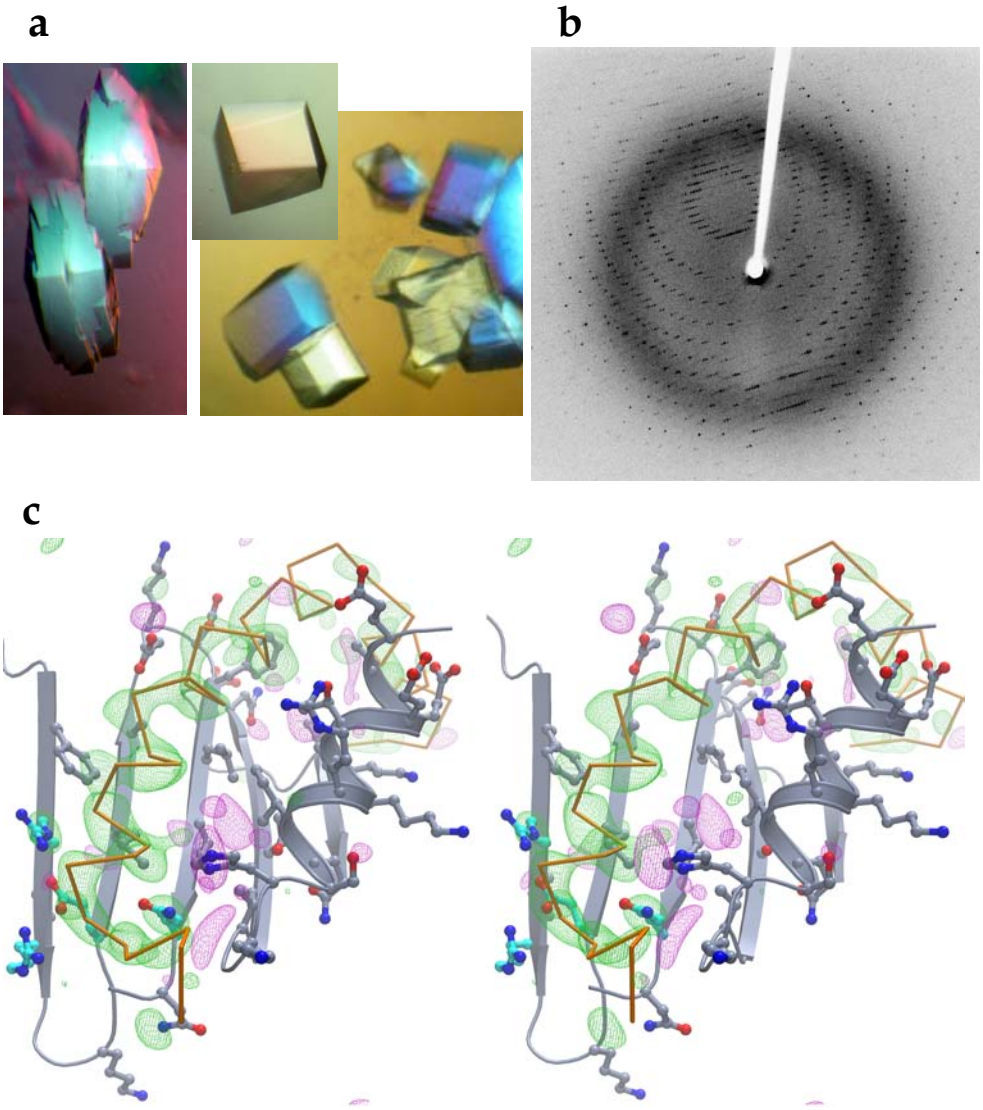

Figure 1.8: X-ray crystallography can provide 3D protein structures. a) Example of protein crystals. Finding conditions in which a protein will crystallize is the first and often rate limiting step in protein crystallography. b) Representative diffraction pattern for a protein crystal. Diffraction intensities are used to calculate electron density maps into which protein models are built. c) Stereo view of an incomplete protein model with some side chains included for reference. Missing (green) or extra (magenta) electron density unaccounted for by the model is shown, through which a helical backbone atom trace (orange) has been added to guide the eye. Panel "c" adapted from Figure 5.3a.

X-ray crystallography is unparalleled in its ability to provide structural information on proteins. Typical X-ray crystal structures contain atom positions accurate to greater than 0.1 nm, and have allowed us to determine the constellation of hydrogen bonds and hydrophobic interactions that stabilize partner binding.

For any system, the combination of NMR, ITC and X-ray crystallography provides unique but complementary lines of information. For example, measurements from ITC provide a link between protein dynamics measured by NMR and the $-T\Delta S°$ of binding. Similarly, structures of protein complexes can provide a foundation for interpreting dynamic and thermodynamic results. Thus if tractable by all three techniques, an unparalleled understanding of the molecular details of a biological system may emerge. To understand how the dynein cargo binding sub-domain is assembled and regulated, I have used these techniques to characterize the components of the cargo binding sub-domain separately and together.

Work presented in this study

Tctex1 and LC8 both bind to a large number of proteins (fourteen and twenty different partners for Tctex1 and LC8, respectively, Table 1.1 and 1.2). Work published by the Barbar lab proposes the function of Tctex1 and LC8 is to regulate partner dimerization (Barbar 2008). Phosporylation of Tctex1 or LC8 directly disrupts IC binding, and in the case of LC8 results in dimer dissociation (Song *et al.* 2007). Since LC8 binds all its partners at the same site as IC, monomerization of LC8 is expected to similarly affect LC8 association with other partners. Consistent with this, increased pools of phosphorylated LC8 have been observed in human breast cancer cells, where LC8 is no longer able to bind the apoptotic protein Bim, resulting in reduced apoptosis (Song et al. 2007; Song *et al.* 2008). To understand the molecular interactions governing LC8•partner recognition, I assayed changes in LC8 internal dynamic between monomer and

dimer forms, as well as dynamic and thermodynamic differences between LC8 in complex to multiple binding partners (see Chapters 2, 3).

Tctex1 and LC8 are paralogs which bind separate partners and a single common partner, IC, to which they bind to at adjacent sites and in an analogous manner. To understand the function of adjacent Tctex1 and LC8 binding sites on IC, I employed structural and thermodynamic characterization of the IC•Tctex1•LC8 ternary complex (see Chapter 4).

LC7 is an integral components of both cytoplasmic and axonemal dyneins (Wickstead *et al.* 2007) and is known to bind IC in response to phosphorylation *in vivo* (Ding et al. 2005). To understand the molecular basis for the IC•LC7 interaction, I determined the structures of apo-LC7 and the IC•LC7 complex (see Chapter 5).

The results of these studies provide evidence for a dynamic and thermodynamic basis for LC8•partner recognition; for Tctex1, LC8 and LC7 affecting each others' binding to IC despite no direct light chain•light chain interactions; and for the light chains fulfilling a regulatory role for IC dimerization and assembly into dynein (see Chapter 6).

Chapter 2

Differences in dynamic structure of LC8 monomer, dimer and dimer-peptide complexes

Justin Hall, Andrea Hall, Nathan Pursifull and Elisar Barbar

Published in *Biochemistry*,
2008, 47 (46), 11940-11952

Summary

Dimerization of dynein light chain LC8[1] creates two symmetric grooves at the dimer interface with diverse binding capabilities. In addition to pH and protein concentration, dimerization is affected by phosphorylation, as illustrated by a phosphomimetic mutation that promotes dissociation of LC8 to a monomer and subsequent dissociation from the dynein complex *in vitro*. In this work we characterize the dynamic structure and unfolding profiles of an LC8 mutant, H55K, as a model for monomeric LC8 at neutral pH. Backbone ^{15}N relaxation experiments show that the monomer, while primarily ordered, has more heterogeneous dynamics relative to the LC8 dimer, predominantly in residues that ultimately form the binding groove, particularly those in β_1 and β_3 strands. This heterogeneity suggests that conformations that are primed for binding are sampled in the inactive monomer and favored in the active dimer. Further changes of LC8 backbone dynamics upon binding to short peptides from Swallow (Swa) and dynein intermediate chain (IC) were elucidated. The conformational heterogeneity apparent in the LC8 dimer is retained in LC8•IC but is lost in LC8•Swa, suggesting that the degree of ordering upon binding is ligand dependent. The reduced complexity of motion in LC8•Swa correlates with the less favorable entropy of binding of LC8 to Swa relative to IC. We propose that the conformational motility of β_3 has functional significance in dimerization and in ligand binding. In the latter, β_3 flexibility apparently accommodates different binding modes for different ligands resulting in ligand-specific conformational

[1]The abbreviations used are: LC8, 10 kDa dynein light chain; H55K and S88E are LC8 mutants with His 55 changed to Lys and Ser 88 changed to Glu, respectively; Bim, peptide corresponding to residues 48-64 from proapoptotic Bcl2 family protein Bim; IC, peptide corresponding to residues 123-138 of cytoplasmic dynein intermediate chain; Swa, peptide corresponding to residues 281-297 from Swallow protein; CaM, calmodulin; CD, circular dichroism; HSQC, heteronuclear single quantum correlation; NOE, nuclear Overhauser effect; H/D, hydrogen/deuterium exchange; H/H, hydrogen/hydrogen exchange; ITC, isothermal titration calorimetry; DSS, 2, 2-dimethylsilapentene-5-sulfonic acid; DTT, dithiothreitol; GdnCl, Guanidinium chloride.

dynamics of the binding site that may impact other processes such as accessibility to phosphorylation.

Introduction

Dynein light chain LC8 (also referred to as DYNLL) was first discovered as an essential component of the microtubule-based molecular motor dynein (King et al. 1996) and as such is involved in fundamental processes associated with minus-end directed trafficking. As a component of the dynein complex, LC8 associates directly with dynein intermediate chain (IC) (Lo *et al.* 2001; Makokha et al. 2002). A large fraction of LC8, however, is not associated with dynein (King et al. 1996) suggesting alternate functions for LC8 independent of its function in dynein. LC8 interacts with non-dynein proteins in diverse systems, including neuronal nitric oxide synthase, nNOS (Jaffrey et al. 1996), the proapoptotic Bcl2 family protein Bim (Puthalakath et al. 1999), Swallow protein which is involved in bicoid mRNA localization in *Drosophila* (Schnorrer et al. 2000; Wang *et al.* 2004), the rabies virus phosphoprotein (Tan *et al.* 2007), and Nup159 of the nuclear-pore complex in yeast (Stelter et al. 2007). Based on the diversity of these interactions, and the fact that all known LC8 binding partners share a common binding groove on LC8 with the dynein intermediate chain (Liang et al. 1999; Fan et al. 2001; Benison et al. 2007; Williams et al. 2007), we have proposed that the wide array of LC8 binding partners reflects its role as an essential hub protein (Barbar 2008). In this capacity, LC8 functions not simply as a dynein cargo adaptor, as more widely viewed, but as a promoter of dimerization of its monomeric, partially disordered binding partners (Nyarko et al. 2004; Wang et al. 2004; Benison *et al.* 2008).

LC8 is an 89 amino acid homodimer (Liang et al. 1999) with each protomer composed of a β-sheet packed against two helices. In the dimer structure complexed with the consensus peptide of a binding partner (Figure 2.1, left) (Liang et al. 1999; Fan et al. 2001; Benison et al. 2007), each 5-stranded β-sheet

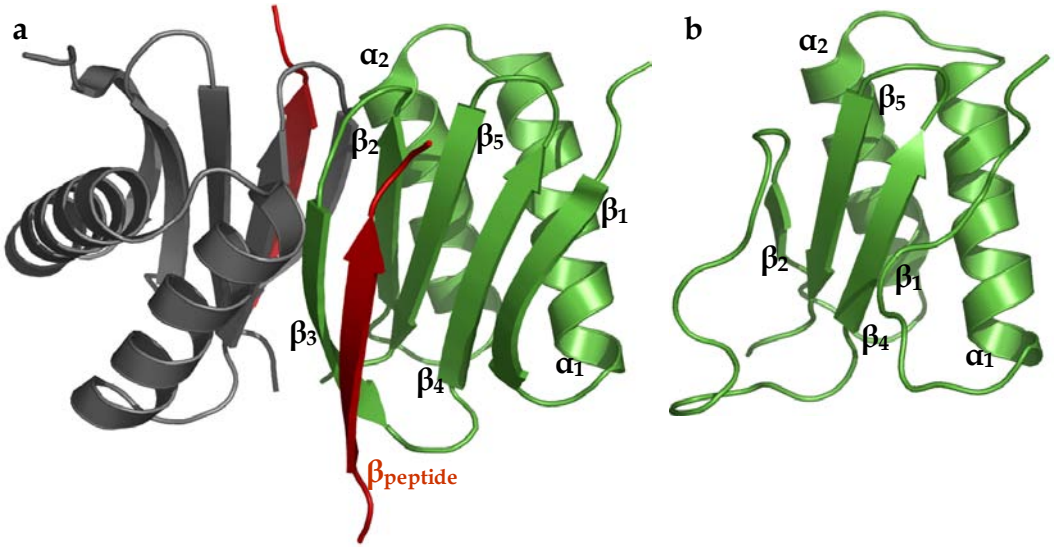

Figure 2.1: Structure of LC8 dimer and monomer. A ribbon diagram of a) dimeric LC8 bound to Swa peptide with the two protomers shown in grey and green and Swa peptide in red ($\beta_{peptide}$), and b) pH 3 monomer of LC8. Secondary structure elements are labeled. For the pH 3 monomer, β_1 and β_2 much shorter and β_3 is disordered. Images were produced with PyMol (DeLano 2002) using PDB codes 2P1K and 1RHW for LC8•Swa and pH 3 monomer, respectively.

includes one strand (β_3) that is contributed by the other protomer. The two β_3 strands are at the protomer-protomer interface where they form the symmetrical binding grooves of the dimer. Binding of ligands to LC8 dimer involves residues in the binding grooves, primarily those of the β_3 strands. Interestingly, binding leads to further extension of the same β-sheet, as the recognition sequence of the binding partner ($\beta_{peptide}$ in Figure 2.1a) forms a sixth strand. Sequence analyses of the binding partners show that they are intrinsically disordered in the vicinity of their recognition sequence (Barbar 2008), suggesting that disorder in these partners may underlie the pleiotropic binding of LC8. Binding is accompanied by disorder to order transition as the ligand partner forms a β-strand ($\beta_{peptide}$). Dissociation of the LC8 dimer at low pH (Barbar *et al.* 2001) eliminates the requisite groove at the dimer interface by disrupting the two β_3 strands (Figure 2.1b) and thereby prevents binding to IC and other LC8 partners that interact in the groove (Wang *et al.* 2003; Makokha *et al.* 2004). Phosphorylation of LC8 at Ser 88 is proposed to be involved in vesicle formation, trafficking functions and cell survival (Song et al. 2008). The interaction of phosphorylated LC8 with the apoptotic protein Bim is abolished, resulting in reduced apoptosis specifically in human breast cancer cells (Song et al. 2007; Song et al. 2008). Experiments with a phosphomimetic Ser 88 to Glu (S88E) mutant suggest that phosphorylation acts *in vitro* as a molecular switch by promoting dissociation of the LC8 dimer and subsequent dissociation from dynein (Song et al. 2007). The phosphomimetic mutant S88E does not bind Bim *in vitro* and *in vivo* (Song et al. 2008), corroborating the idea that phosphorylation results in an inactive LC8 monomer that does not bind any ligand that occupies the binding grooves at the dimer interface.

Interactions involving the β_3 strands are crucial for stabilizing both the dimer and the LC8•target interfaces, and therefore play primary roles in both regulation of activity, and binding diversity. To investigate both processes, we focus on changes in the structure and dynamics of β_3 strands upon LC8 dimer dissociation and upon LC8•target complex formation. Our model for

phosphorylated LC8 monomer at neutral pH is the mutant H55K which is a pure monomer at high protein concentration (Nyarko *et al.* 2005; Song et al. 2007). The single mutation of a buried histidine at position 55 at the dimer interface is sufficient to dissociate the dimer at physiological pH (Barbar *et al.* 2004).

In this work we examine the structure and dynamics of the β_3 region in the model LC8 monomer (H55K), which mimics the biologically relevant phosphorylated form, in LC8 dimer, and in complexes of LC8 dimer bound to consensus peptides of LC8 partners (Figure 2.2). The results support a critical role of β_3 flexibility in the molecular-level functioning of LC8. We find that, in solution, residues of the β_3 strand in apo-LC8 dimer (no bound ligand) are highly flexible, even though these residues are organized into the β-sheet in the apo-LC8 dimer NMR (Fan et al. 2001) and crystal (Benison 2008) structures. The thermodynamics of LC8 binding to three peptides, and the dynamics of the LC8-peptide complexes, reveal a correlation between the flexibility of the binding groove and the entropic cost of binding, and demonstrate that the change in flexibility of LC8 is ligand-dependent.

Results

Stability and Two-State Unfolding of H55K.

Far-UV CD (Figure 2.3) and fluorescence spectra (data not shown) of H55K are similar to those of the WT LC8 dimer, indicating that there is no measurable change upon dissociation of CD-detected secondary structure and of Trp 54 local packing. Near-UV CD spectra, dominated by the signal of Tyr 65 at the dimer interface (Barbar et al. 2001), are different (Figure 2.3b) as expected, consistent with dimer dissociation.

Unfolding profiles for monomeric H55K followed by changes in both fluorescence and far-UV CD at increasing GdnCl concentration are similar (Figure 2.4), suggesting a two-state unfolding transition. Similar thermodynamic parameters were obtained using a two-state unfolding model for fitting both data

$Bim_{48\text{-}64}$ MSCD**KSTQT**PSPPCQAF

$IC_{123\text{-}138}$ KETIVYT**KQTQT**TSTG

$Swa_{281\text{-}297}$ MYHIRSATSA**KATQT**DF

Figure 2.2: Amino acid sequences of peptides used in this study. The sequence of Bim, IC and Swa with KXTQT motif in bold and the segment that forms a $\beta_{peptide}$ underlined.

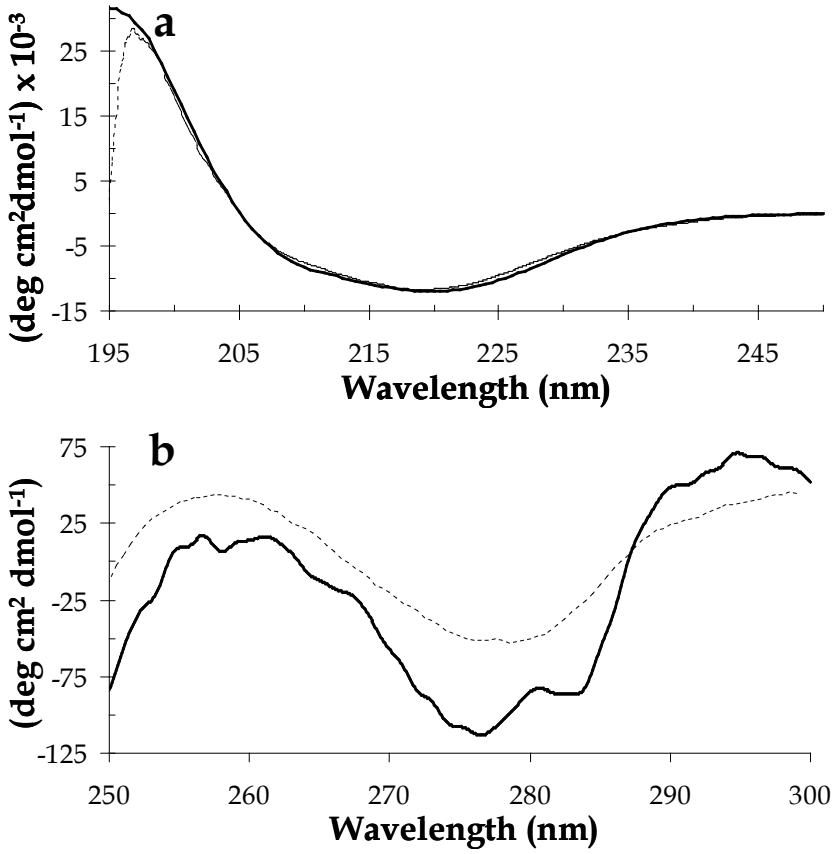

Figure 2.3: H55K and LC8 dimer have similar secondary structure. a) Far- and b) near- UV CD spectra of H55K (light) and WT LC8 (dark). Data were collected at pH 7.0 and monomeric protein concentration of 14 μM for both proteins.

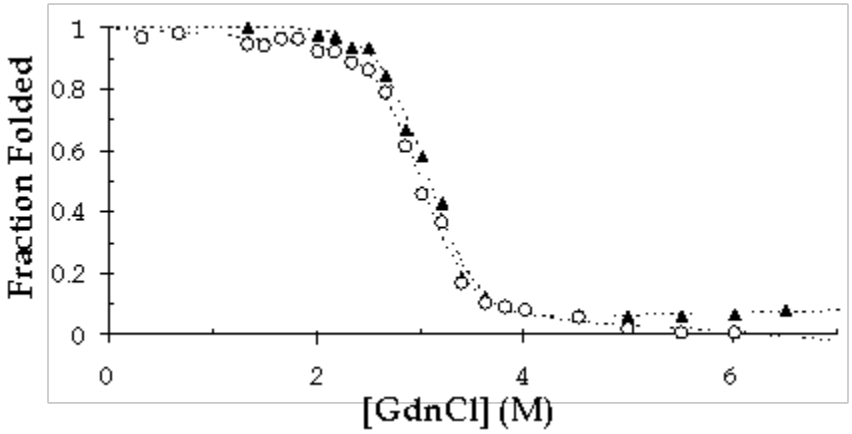

Figure 2.4: GdnCl unfolding profiles of H55K. Loss of intensity in far-UV CD spectra was monitored at 222 nm (circles) and loss of fluorescence intensity was monitored at 327 nm (triangles). Protein concentration was 14 μM for both experiments. Data were acquired at pH 7 and 30 °C using a batch-type experiment to ensure that equilibrium was achieved before data acquisition. A 2-state unfolding model best fits the data (dashed line).

sets (Table 2.1). Equilibrium denaturation experiments carried out over the protein concentration range of 0.4 – 14 μM show similar unfolding profiles, consistent with H55K being a pure monomer (data not shown).

NMR Structural Characterization of H55K.

Resonance assignments of H55K were determined for residues 3-89 from analysis of 3D experiments collected on uniformly ^{15}N and ^{13}C labeled protein (Figure 2.5a). Comparison of the N, H, Cα and Cβ chemical shifts between H55K and LC8 shows that the largest changes occur for residues 55 through 74 and for residue 88 (Figure 2.5b, c, d). In the dimer, these residues primarily correspond to β_3 (residues 63-67), which aligns antiparallel to the opposing protomer's β_2 (residues 53-58). Thus, dissociation of the LC8 dimer results in small changes in chemical shifts for residues in β_2 and large changes for residues in β_3. The change in residue 88 is attributed to being buried at the dimer interface, and fully solvent exposed in the monomer.

Dynamics of H55K and Comparison to WT LC8 Dimer.

Backbone relaxation dynamics were measured from ^{15}N R_1, R_2 and steady-state heteronuclear NOEs for H55K and dimeric LC8 at similar solution conditions (Figure 2.6). For H55K, the average R_1 rate is 2.0 s^{-1} with the largest deviation for residues 4-6, 35, 36 and residues 62-73. The average R_2 rate is 11.3 s^{-1} with the largest deviation for residues 9, 35, 36 and 62-74. The average NOE value is 0.78 with the largest deviation for residues 4-6 and 62-73. Deviation from the average dynamics behavior in H55K is clearly reflected in R_2/R_1 ratios for residues 9, 10, 64, 70 and 74. Except for residues 73 and 74, dimeric LC8 shows more homogeneous dynamics.

Relaxation data were analyzed using the axially symmetric anisotropic diffusion model (Table 2.2). A correlation time of 6.36 ns for H55K compared to the 10.61 ns for the LC8 dimer is consistent with the smaller size of the monomer.

Table 2.1: Thermodynamic parameters obtained from equilibrium denaturation of H55K at pH 7.

	ΔG° (kcal/mol)	**C_m (M)**	**slope (kcal/mol/M)**
CD	7.80	2.99	-2.61
fluorescence	7.45	3.06	-2.44

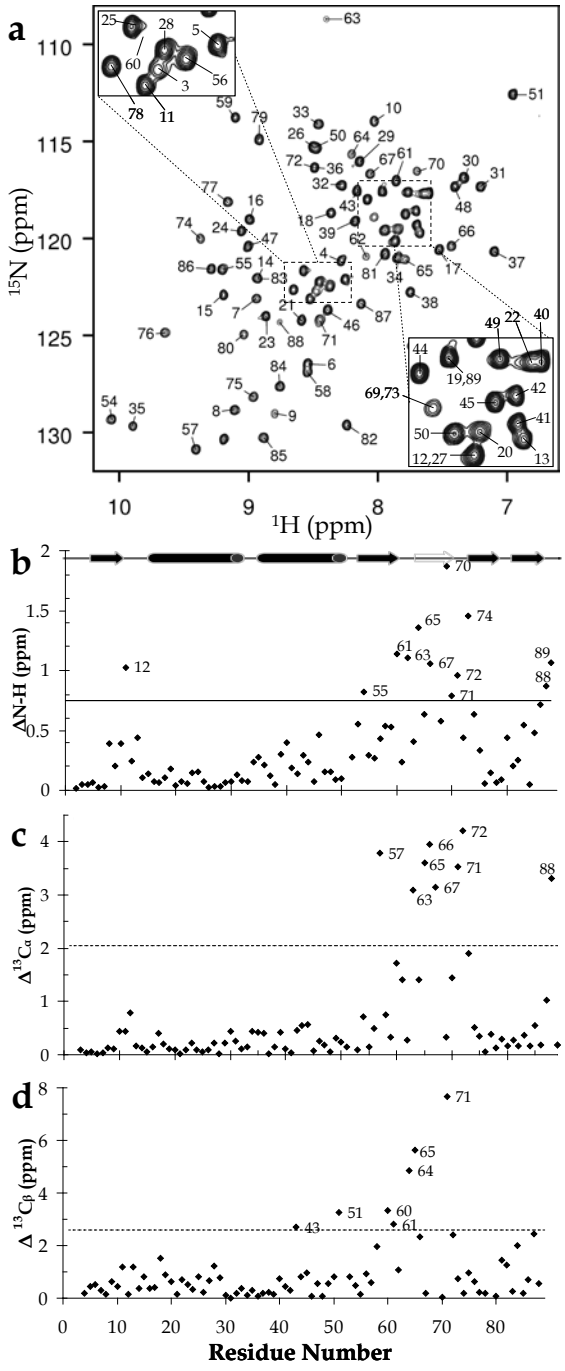

Figure 2.5: NMR analysis of H55K. a) ^{1}H-^{15}N HSQC spectrum with backbone assignments, and absolute b) ^{1}H-^{15}N, c) ^{13}Cα and d) ^{13}Cβ chemical shift differences between H55K and LC8 are shown. Residues greater than two standard deviations (dashed line) above the average chemical shift difference are labeled. The majority of labeled residues are in the segment which forms β_3 at the dimer interface. The secondary structure of LC8 without β_3 is shown above the plots.

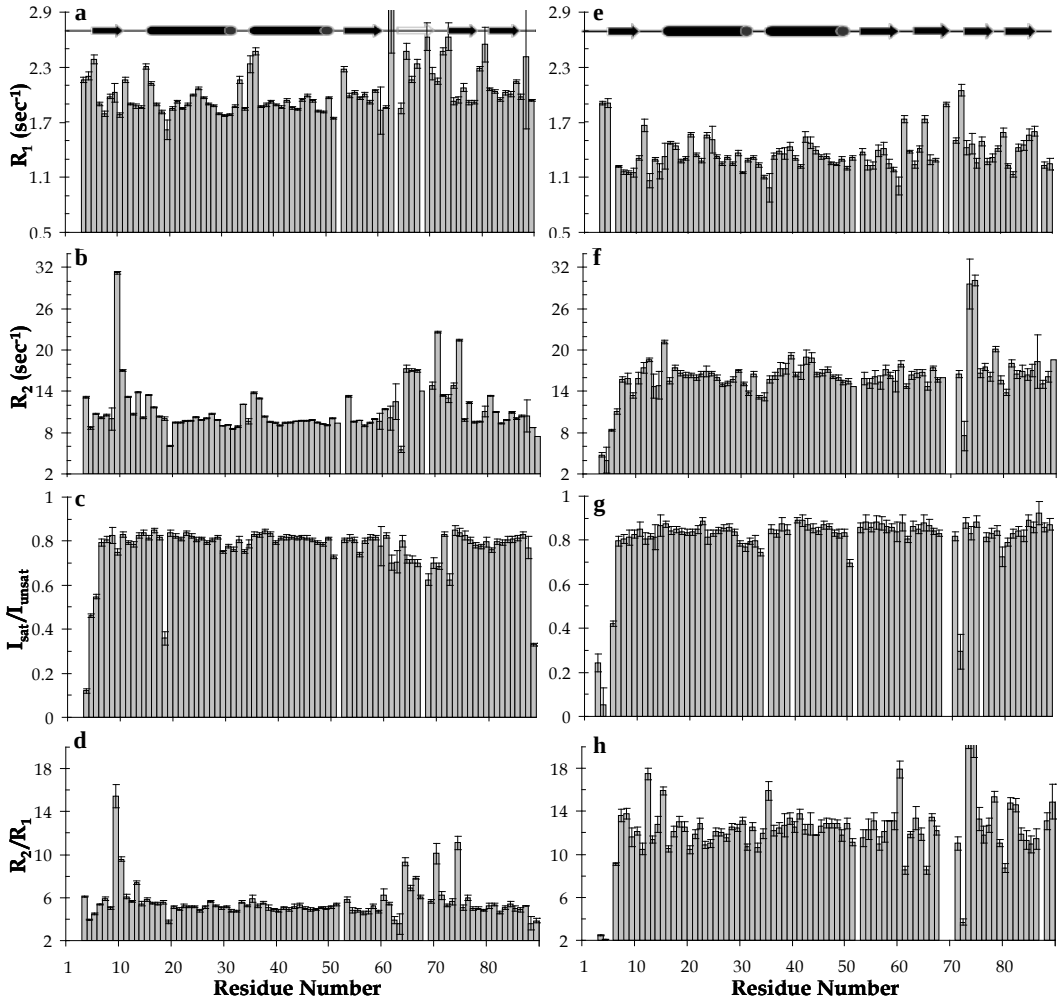

Figure 2.6: Dynamics analysis of H55K and LC8 dimer. Plots of ^{15}N R_1, R_2 and steady-state ^{1}H-^{15}N NOE recorded for H55K (a, b, c) and LC8 (e, f, g) at pH 6.7 and 30 °C. R_2/R_1 ratios are shown in d and h for H55K and LC8, respectively. There is more heterogeneity in R_2 measurements in H55K relative to the LC8 dimer. Protein secondary structure is shown above the plots.

Table 2.2: Principal axis ratios and axially symmetric diffusion tensor summary.

	principal axis ratio				
protein	I_{xx}	I_{yy}	I_{zz}	τ_m[a] **(ns)**	D_{ratio} $(D_{\parallel}/D_{\perp})$
H55K	1.00	0.89	0.71	6.36 ± 0.03	1.07
LC8	1.00	0.93	0.52	11.31 ± 0.07	1.39
LC8/IC	1.00	0.94	0.59	14.07 ± 0.04	1.28
LC8/Swa	1.00	0.93	0.58	13.16 ± 0.06	1.11

[a]Calculated average correlation time.
[b]pH 6.7 values.
[c]pH 5.5 values.

The $D_{\parallel}/D_{\perp}$ of LC8 (1.27) is larger than H55K (1.07) indicating that the LC8 dimer is more oblate.

Model free parameters and model type distribution are shown in Figure 2.7 for H55K and LC8 dimer. A higher percentage of residues in H55K were fit by models 3 or 4 than by model 1 (Figure 2.7a). Two stretches of residues in H55K contain significant R_{ex} terms compared to the average (Figure 2.7d) suggesting conformational heterogeneity. These include residues 4-13, which correspond to the N-terminus and β_1 and residues 64-74, which correspond to β_3 (disordered in monomer), the loop connecting β_3 to β_4 and the first two residues of β_4.

Residues in LC8 dimer were fit primarily by models 1 and 3. The large R_{ex} term at the N-terminus, β_1 and β_3 regions observed in H55K has decreased significantly in the LC8 dimer. A small R_{ex} term was necessary to improve the fit of some residues, which are primarily located in either α_1 or α_2 with the largest corresponding to residue 74 in β_4.

Comparison of S^2 values between H55K and LC8 shows little difference between residues that have ordered secondary structure elements in LC8, with the exception of β_3. In H55K, the S^2 values for residues 65-73 display significantly lower values than the same residues in the dimer (Figure 2.7b, f).

Dynamics of LC8•IC and LC8•Swa Complexes.

Backbone relaxation dynamics were measured for LC8 and compared to LC8 bound to two KXTQT-motif containing peptides: the intermediate chain residues 123-138 (IC) and the Swallow residues 281-297 (Swa) (Figure 2.8). The average R_2 values for apo-LC8, LC8•IC and LC8•Swa are 15.2, 18.1 and 16.9 s^{-1}, respectively. The lower value for apo-LC8 is consistent with its smaller size relative to the complexes, and the lower value for LC8•Swa relative to LC8•IC suggests faster tumbling due to a more compact structure (there is a negligible difference in the size of IC and Swa peptides: Swa is 142 Da greater in mass than IC). Lower R_2 values relative to the average are observed for residues 29-34 and

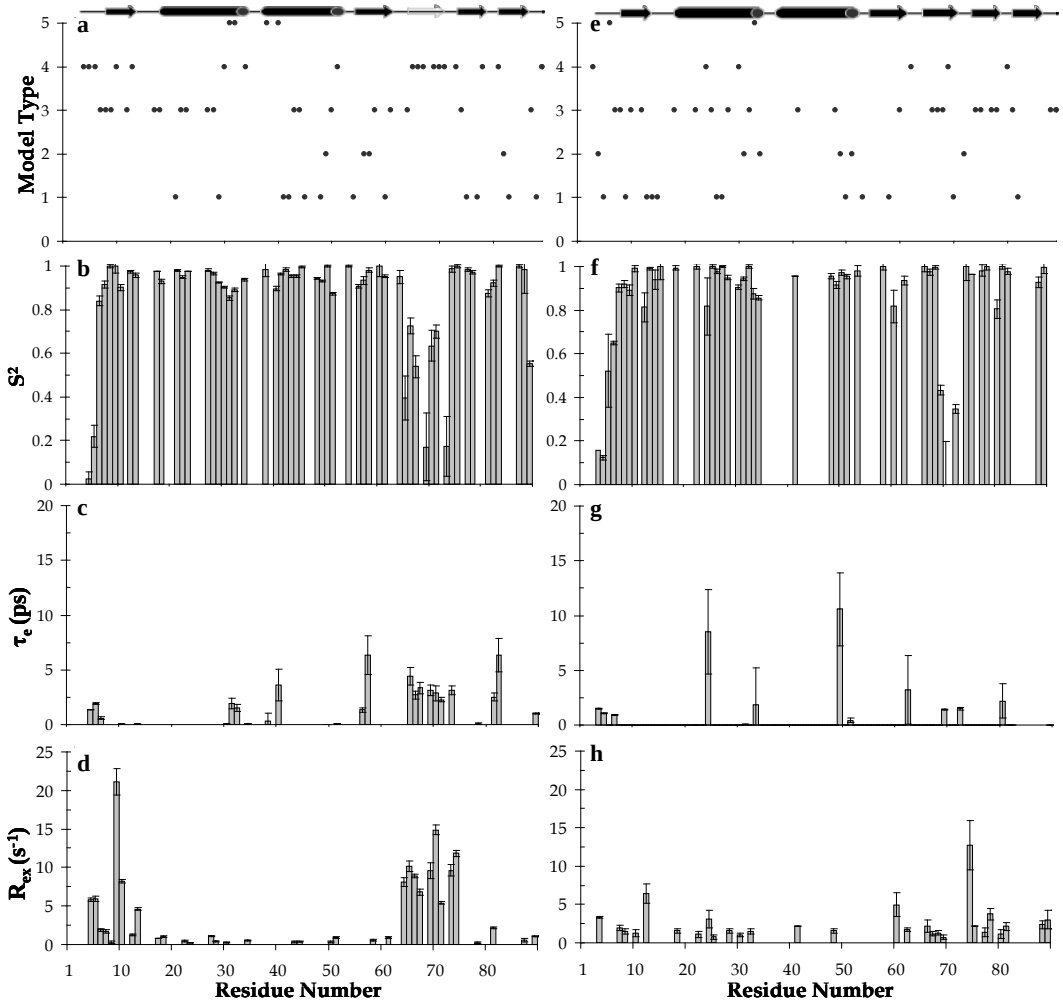

Figure 2.7: Model free analysis of H55K and LC8 dimer. Comparison of model free analysis between H55K (a, b, c, d) and LC8 (e, f, g, h). Residues in β_3 have lower order parameters (S^2) (b, f) in the monomer relative to the dimer. R_{ex} terms are more prominent in H55K, particularly in residues 9,10 and 64-74 (d). R_{ex} is distributed along the sequence in LC8 dimer (h).

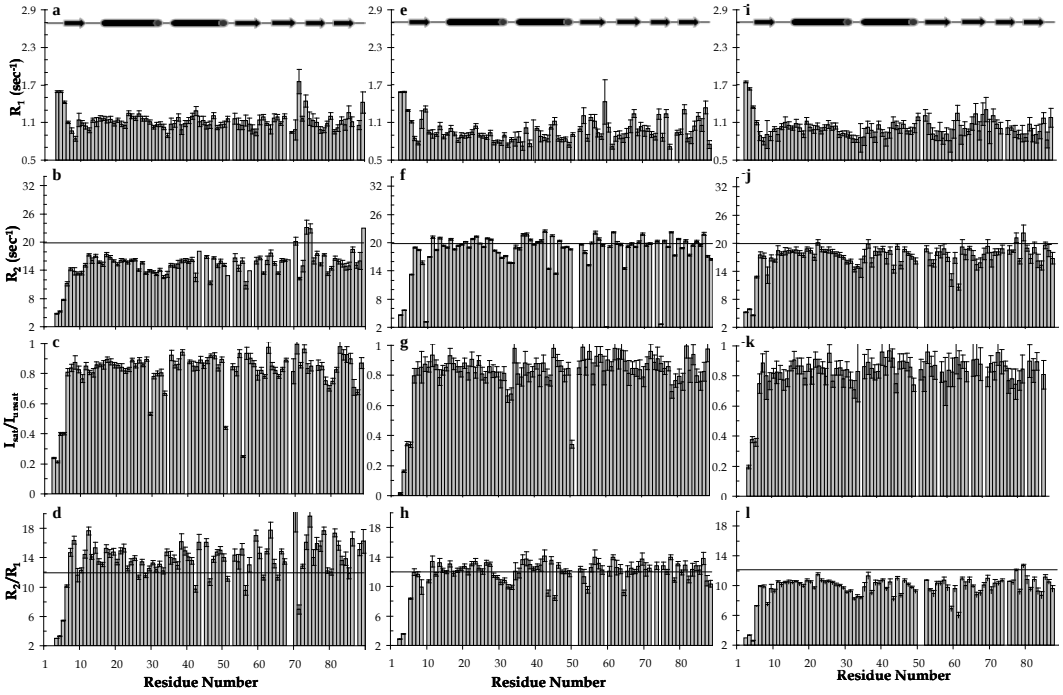

Figure 2.8: Dynamics analysis of apo-LC8 and LC8 complexes. Plots of ^{15}N R_1, R_2 and steady-state ^{1}H-^{15}N NOE recorded for apo-LC8 (a, b, c) LC8•IC (e, f, g) and LC8•Swa (i, j, k) at pH 5.5 and 25 °C. R_2/R_1 ratios are shown in d, h and l for apo-LC8, LC8•IC and LC8•Swa, respectively. A line is drawn in b, d, f, h, k and l to aid visual comparison. Higher R_2 and R_2/R_1 for LC8•IC indicate more heterogeneous dynamics than for LC8•Swa. Protein secondary structure is shown above the plots.

31-35 for LC8•IC and LC8•Swa, respectively. Both LC8•IC and LC8•Swa have similar average steady state NOE values with residues 4-6 having the largest deviations from the average. R_2/R_1 average ratio is lower for LC8•Swa relative to LC8•IC and apo-LC8, consistent with more isotropic tumbling and homogeneity of motion in LC8•Swa.

Relaxation data analysis (Table 2.2) shows that both LC8•peptide complexes have slower tumbling times compared to apo-LC8 of 11.3 ns; 14.1 ns for LC8•IC and 13.2 ns for LC8•Swa. The faster tumbling time of LC8•Swa relative to LC8•IC is consistent with it being more compact. In accord with this, the $D_{\parallel}/D\perp$ of LC8•Swa (1.11) is smaller than that of LC8•IC (1.28), and both are smaller than that of the apo- LC8 dimer (1.39) suggesting that peptide binding results in a more spherical structure.

As with apo-LC8, residues in LC8•IC were mostly fit by models 1 or 3 (Figure 2.9a, e). A general comparison of the S^2 values, model type and level of heterogeneous motions in apo-LC8 and LC8•IC suggests a little change in the overall magnitude and type of backbone motions. In contrast, residues in LC8•Swa were fit almost exclusively by model 1, indicating near homogenous motion for the whole molecule (Figure 2.9i).

Hydrogen Exchange Measurements.

LC8 dimer is more protected from hydrogen exchange than H55K. Eleven amide protons in LC8 and none in H55K have H/D exchange rates that are too slow for accurate determination by H/D experiments under our experimental conditions. There are 41 amide protons in LC8 and 48 in H55K that exchange in the deadtime of the experiment. The additional 7 residues in H55K are located at the ends of secondary structure elements of the LC8 dimer. Only residues involved in secondary structure in LC8 have H/D exchange rates measurable in both WT LC8 and H55K under these conditions. Interestingly, residues in β_3 at the dimer interface are *not* protected in the dimer in this time window.

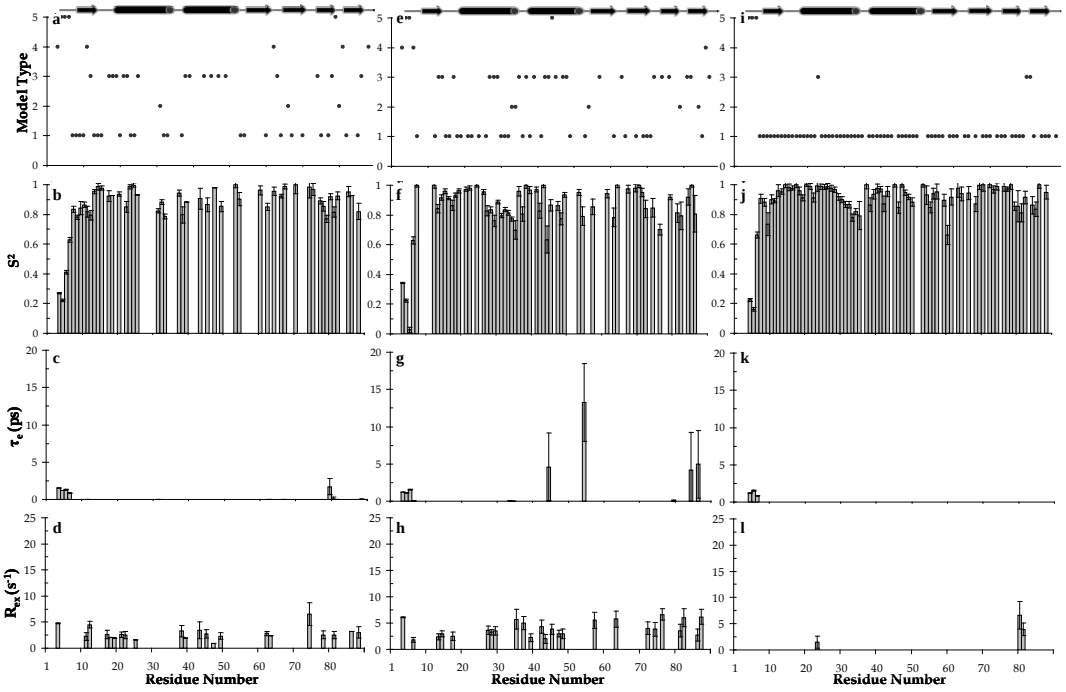

Figure 2.9: Model free analysis of apo-LC8 and LC8 complexes. Comparison of model free analysis between apo-LC8 (a, b, c, d), LC8•IC (e, f, g, h) and LC8•Swa (i, j, k, l). Less then half of the residues in apo-LC8 or LC8•IC were adequately fit by model 1, whereas residues in LC8•Swa were fit almost exclusively by model 1, indicating a greater heterogeneity of motion for apo-LC8 (a) or LC8•IC (e) relative to LC8•Swa (i). Loss of the R_{ex} term is observed only with LC8•Swa.

H/H experiments provide exchange rates within the 1 to 100 millisecond timescale and are thus complementary to H/D exchange experiments for fast exchanging residues. CLEANEX HSQC spectra for H55K and LC8 are presented in Figure 2.10. At a 20 millisecond exchange time, H55K spectra show more peaks corresponding to fast exchanging amide protons consistent with more exposed residues in the monomer. For both proteins, the fast exchanging protons observed in H/H experiments are in the loops and at the ends of secondary structure elements (Figure 2.11, red). The stretch of residues 63-67 which correspond to β_3 are observed only in the monomer. Only loop residues 61-62 preceding β_3 are observed in the dimer indicating that residues in β_3 are more protected in the dimer at this timescale and therefore not observed. In the LC8•Swa complex, only residues 3, 4 and 5 at the flexible N-terminus are observed at similar conditions, consistent with diminished flexibility of LC8 upon binding to Swa peptide. Figure 2.11 summarizes the H/D and H/H exchange boundaries mapped onto the structures of monomeric and dimeric LC8.

Thermodynamics of LC8 Binding to Diverse Peptides.

Isothermal titration calorimetry (ITC) measurements of LC8 binding to Bim, IC and Swa peptides performed at 30 and 35 °C show a lower association constant for LC8•IC relative to LC8•Bim or LC8•Swa (Figure 2.12). Interestingly, while all three peptides share the same binding site on LC8, the thermodynamic parameters governing association are different. At 30 °C, binding to IC is entropically favorable (K_d of 3.0 μM, $\Delta H°$ of -4.0 and $-T\Delta S°$ of -3.8 kcal/mol), while the binding to Bim or Swa is entropically unfavorable (K_d of 0.6 μM, $\Delta H°$ of -10.4 kcal/mol and $-T\Delta S°$ of 1.8 kcal/mol for Bim; K_d of 0.6 μM, $\Delta H°$ of -10.7 kcal/mol and $-T\Delta S°$ of 2.0 kcal/mol for Swa). A similar pattern for thermodynamic parameters is observed at 35 ˚C (Figure 2.13).

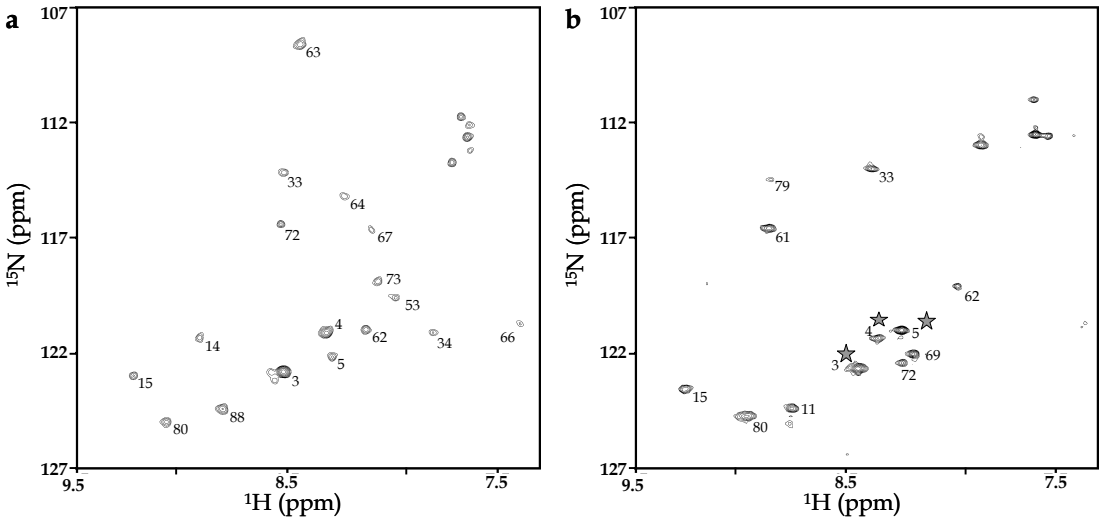

Figure 2.10: H/H exchange spectra for H55K and dimeric-LC8 show differences at the dimer interface. ^{1}H-^{15}N CLEANEX HSQC spectra for (a) H55K and (b) LC8 collected at pH 6.7 and 30 °C with a mixing time of 20 milliseconds. Peaks shown in the spectra correspond to amide protons that rapidly exchange with water, and are colored red on the corresponding structures in Figure 11. Only residues 3, 4 and 5 are observed in LC8•Swa (star).

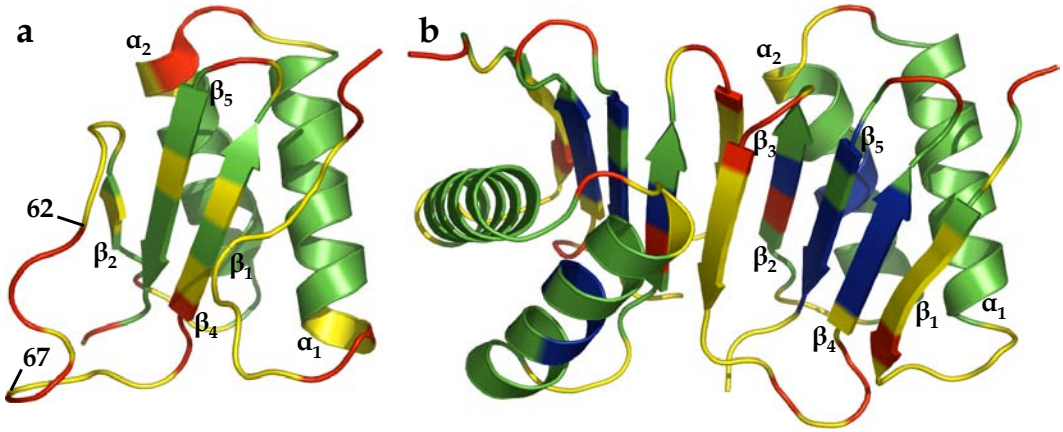

Figure 2.11: Comparison of H/D and H/H exchange between LC8 dimer and H55K monomer. Amino acids are colored with respect to amide proton exchange rates, the slowest exchanging protons are shown in blue, those that are measured by H/D exchange are shown in green, and the protons that are too fast to measure by H/D exchange but too slow to measure by H/H exchange are shown in yellow. The fastest exchanging protons are shown in red. Images were produced with PyMol using PDB codes 1RHW and 2P1K as models for a) monomeric and b) dimeric LC8, respectively.

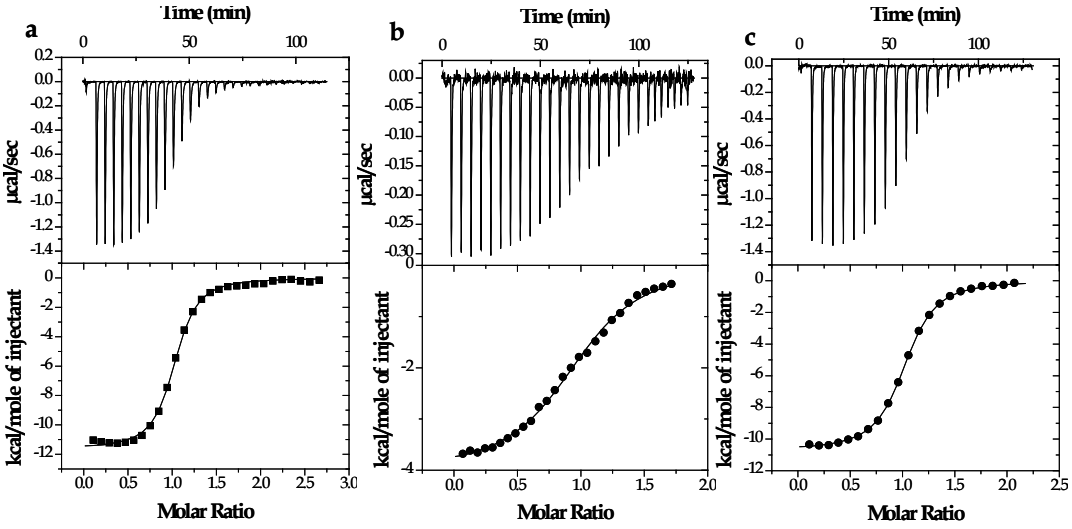

Figure 2.12: LC8 binds peptides from Bim, IC and Swa with distinct thermodynamic parameters. ITC raw data (top panels) and binding isotherms (bottom panel) for the titration of LC8 with a) Bim, b) IC and c) Swa peptides at 30 °C. Solid lines in the bottom charts represent the theoretical fit for **A** + **B** → **AB** binding model where **A** corresponds to the peptide and **B** corresponds to one protomer of LC8. The transition region of the curves is well fit indicating accurate determination of association constants. LC8 binds IC with the lowest affinity.

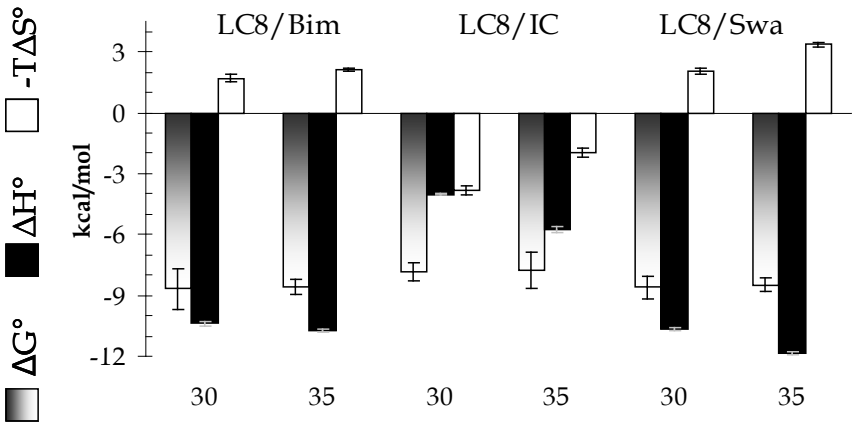

Figure 2.13: Plot of thermodynamic association parameters for LC8•Bim, LC8•IC and LC8•Swa at 30 and 35 °C. The dissociation constants (K_d) at 30 and 35 °C for LC8•Bim are 0.6 and 0.8 μM, for LC8•IC are 3.0 and 3.3 μM and for LC8•Swa are 0.6 and 1.0 μM.

Discussion

H55K Is a Model for Monomeric LC8 at Neutral pH.

H55K is a stable monomer with an average structure similar to one chain of the LC8 dimer as demonstrated by similar CD and fluorescence spectra. Unfolding profiles of H55K show a two-state transition with unfolding free energy of 7.45 kcal/mol. This value is similar to the 7.5 kcal/mol obtained for the monomer unfolding step in the three-state unfolding transition of WT dimeric LC8 at pH 7 (Barbar et al. 2001).

The pH 3 WT LC8 is also a stable monomer whose structure is similar to one chain of the LC8 dimer except that β_3 is disordered (Figure 2.1b) and more flexible than the rest of the protein. (Barbar et al. 2001; Makokha et al. 2004). The β_3 strand in H55K is also disordered as indicated by random coil-like secondary chemical shifts and relatively low order parameters. A minor population of ordered conformations for β_1 and β_3, however, is inferred from higher steady state NOEs and more heterogeneous dynamics than in those observed in the pH 3 WT monomer (Makokha et al. 2004). The heterogeneity in residues 62-73 may be partially due to protonated-deprotonated states of His 68 and His 72 as previously suggested (Mohan *et al.* 2006) which in H55K have pKa values of 6.5 and 6.2, respectively (Nyarko et al. 2005). However, both residues are exposed to solvent in the monomer structure**,** and therefore we do not anticipate their ionization state to significantly influence conformational heterogeneity. The disorder in β_3 argues against a domain swapping mechanism of assembly (Makokha et al. 2004) since the β_3-β_2' contacts of the dimer are not replicated in analogous β_3-β_2 contacts in the monomer, as expected for domain swapping (Schlunegger *et al.* 1997).

The two-state unfolding mechanism for H55K at pH 7 is in contrast to the complex global unfolding profiles reported for the pH 3 WT monomer (Chatterjee *et al.* 2007). The differences in unfolding mechanisms and backbone dynamics between pH 3 and pH 7 monomers suggest that further unfolding occurs at low pH in addition to dimer dissociation and argue against the suitability of pH 3 WT as a

model for monomeric LC8 at neutral pH, as in previous literature (Mohan et al. 2006; Chatterjee et al. 2007; Krishna Mohan 2007; Krishna Mohan *et al.* 2008).

Heterogeneity in H55K Is Specific to Residues that Form the Binding Groove in the Dimer.

Three groups of residues in H55K show non-uniform backbone dynamics at intermediate (millisecond-microsecond) and fast (nanosecond-picosecond) timescales: *1)* Residues 62-73 exhibit conformational heterogeneity at both the fast timescale (higher R_1, lower steady state NOE, lower S^2) and intermediate timescale (higher R_2, and higher R_{ex}); *2)* Residues 9 and 10 show conformational heterogeneity at the intermediate timescale (higher R_2 and higher R_{ex}); *3)* Residues 35 and 36 in the loop connecting helix 1 and 2 show more flexibility at the fast timescale (higher R_1, lower steady state NOE). In the dimer, while some overall heterogeneity is retained, it is considerably less pronounced than in the monomer.

In crystal structures of LC8 complexes with IC and Swa peptides, residues 9, 35, 36 and 62-73 are directly involved in peptide binding. The side chain of Lys 9 in LC8 makes electrostatic interactions with Asp 296 of Swa. The side chain of Asp 35 and the amide proton of Lys 36 in LC8 form hydrogen bonds with the highly conserved Gln of the KXTQT-motif in IC and Swa. Residues 62-73, corresponding to β_3 and the loop connecting β_3 to β_4, make direct contacts with the peptide at the dimer interface ($\beta_{peptide}$, Figure 2.1). Thus, the residues that exhibit heterogeneous backbone dynamics in H55K ultimately form the binding grooves at the dimer interface. These data suggest that in the inactive monomer residues in strands β_1, β_3 and loop connecting β_3 to β_4, while on average disordered, also sample a minor population of conformations that are primed for dimerization and ligand binding, and are favored upon dimerization.

Hydrogen Exchange Differences upon Dimerization.

All residues in β_1 and β_3 in the dimer exchange much faster than the rest of the secondary structure. While the susceptibility to exchange is not surprising for β_1 at the flexible N-terminus, it is surprising for β_3, whose stabilization is inferred from the dimer NMR structure (Fan et al. 2001) and from higher S^2 and steady state NOE values relative to the monomer (Figures 2.6 and 2.7). The apparent mobility of this region in the solution structure is in contrast to the ordered crystal structure. Amide protons of residues 63, 65 and 67 in β_3, and 69 and 72 in the loops are completely buried in the crystal structure of the apo-LC8 dimer, and their low temperature factors suggest a high degree of order (Benison 2008). It is possible that the higher H/D exchange rates in β_3 is due to the presence of a minor population of the monomer, which has a disordered β_3 in equilibrium with the dimer. This possibility cannot be ruled out but lack of protection in β_3 is also observed at neutral pH (Fan *et al.* 2002) and a high protein concentration where the population of a monomer is minimal (Barbar et al. 2001; Nyarko et al. 2005).

While β_3 residues are more flexible by hydrogen exchange criteria than residues in other secondary structure elements in the dimer, they are more ordered than residues in the adjacent loops, residues 61- 62 and 69-72. All residues within β_3 have slower exchange rates than those of the same sequence position in the monomer. Taken together, the data at neutral pH suggest that in the monomer, β_3 is primarily disordered but also samples native-like conformations, while in the solution dimer, β_3 is primarily native-like but also samples disordered conformations. Further, in the solution dimer, β_3 is apparently more flexible than in either the apo-LC8 dimer crystal structure or in the dimer•peptide complex.

Another interesting difference is in Ser 88, which packs against β_3 residues at the dimer interface. The amide NH of Ser 88 shows no protection in H/D exchange in the dimer, exchanges too slowly to be observed in H/H exchange in the dimer but exchanges fast enough to be observed in the H/H of the monomer. Slowing the exchange of 88 NH is consistent with ordering of the interface and

possible formation of a transient hydrogen bond as reported in (Mohan *et al.* 2008).

Changes in Conformational Heterogeneity of LC8 Are Ligand Dependent.

Most known LC8 binding partners have either a KXTQT or a less common GIQVD sequence that is considered to be an LC8 binding motif (Lo et al. 2001; Rodriguez-Crespo *et al.* 2001). In crystal and NMR structures of LC8 with Bim, IC and Swa peptides, all containing the KXTQT recognition sequence, these ligands share a common site on LC8. The backbone atoms for the bound IC and Swa peptides and the adjacent β_3 from LC8 can be overlaid with an RMSD of 0.2 Å (Benison et al. 2007). Despite average structure similarities, dynamics analysis of LC8 in complex with IC or Swa peptides shows a striking difference in the complexity of motion. These experiments were performed with a large excess of the ligand, at conditions where the protein is > 99.9% bound. For both apo-LC8 and LC8•IC, models containing $\boldsymbol{\tau}_e$ and R_{ex} parameters are required for more than half of the residues being fit. In contrast, residues in LC8•Swa were analyzed almost exclusively by model 1, consistent with higher homogeneity of motion relative to apo-LC8 or LC8•IC. The difference in complexity of motion suggests a significant ordering of LC8 backbone dynamics only upon binding to Swa.

The greater order in LC8•Swa relative to LC8•IC inferred from backbone relaxation dynamics is consistent with the increased protection from hydrogen exchange observed for LC8•Swa relative to LC8•IC (Benison et al. 2007). ^{15}N backbone dynamics of LC8•Bim reported earlier show that as with Swa, Bim binding to LC8 causes an increase in the homogeneity of the motion particularly in the binding groove, and led to the proposal that the flexibility of the binding grooves in LC8 underlies its binding diversity (Fan et al. 2002). Comparison of the dynamics of LC8 with the three peptide partners suggests that the extent of ordering of the binding groove is not the same for all peptides. There is an increase in homogeneity of the whole protein with Swa and Bim but not with IC. Since all

three peptides share the KXTQT recognition motif, residues that flank the recognition motif must dictate the ordering of the groove upon binding.

Correlation between Thermodynamics and Dynamics of Binding.

LC8 binds many diverse partners and fits the definition of an ordered hub for disordered partners (Barbar 2008). As has been demonstrated for calmodulin, CaM, (Frederick *et al.* 2007), another primarily ordered hub protein (Dunker *et al.* 2005), LC8 can bind to a large number of different proteins in the same groove, with roughly the same affinity but with different thermodynamic association parameters. Similar to CaM, the flexibility of the binding groove may allow accommodation of significantly different peptide sequences for high affinity binding (Lee *et al.* 2000; Fan et al. 2002).

The association between LC8 and IC is entropically favorable, while the association between LC8 and Bim or Swa is enthalpically driven and entropically disfavored. A difference of 5.5 kcal/mol in $T\Delta S°$ between IC and Bim or Swa binding is compensated by a difference of 6.5 kcal/mol in $\Delta H°$ at 30 ˚C. A recent study by Leung *et al.* shows rearrangement of solvent hydrogen bond networks may provide the driving force for non-specific binding interactions (Leung *et al.* 2008). In principle, the finding of Leung *et al.* can be applied to the LC8•ligand system; however the differences between non-specific host•guest and a pre-organized protein•ligand binding system make it difficult to interpret the magnitude of solvent contributions to the measured LC8•ligand thermodynamic binding parameters.

The LC8•IC and LC8•Swa crystals structures show similar burial of hydrophobic surface area (Benison et al. 2007). Differences in side chain electrostatic interactions are observed in the crystal structures of LC8•IC and LC8•Swa, and are consistent with the larger enthalpy of binding for LC8•Swa. Asp 296 of Swa and Lys 9 of LC8 form an electrostatic bridge, which is absent in IC (the corresponding residue in IC is Thr 135). There is also an intrachain

hydrogen bond between the carboxyl oxygen of Swa Thr 288 and the side chain of Ser 289, whereas there is no such interaction between the corresponding residues of IC (Val 127 and Tyr 128). Thus the differences in binding enthalpies correlate with electrostatic differences between LC8•IC and LC8•Swa interactions.

^{15}N backbone order parameters are similar for both complexes but conformational heterogeneity measured as deviations from the simplest model is quite different. The entropically favored IC binding to LC8 shows a minimal change in the backbone dynamics relative to apo-LC8, while the entropically disfavored Swa and Bim binding are consistent with the increase in homogeneous dynamics in LC8•Swa and LC8•Bim relative to both apo-LC8 and LC8•IC. Thus the differences in binding entropies correlate with changes in backbone dynamics occurring upon binding.

Based on the available data it is our conclusion that a significant contribution to the difference in enthalpic and entropic binding energies can be explained by differences in LC8•ligand electrostatics and changes in protein dynamics. As has been observed for CaM association with several of its binding partners (Frederick et al. 2007), changes in LC8's internal dynamics are ligand dependent and illustrate the importance of conformational entropy in high affinity protein-protein interactions (Lee et al. 2000; Frederick et al. 2007).

Dynamics and Regulation.

In crystal structures of apo-LC8 and LC8•peptide complexes, the side chain of Ser 88 is buried and not apparently accessible to phosphorylation. This raises the question of how Ser 88, the putative phosphorylation site (Vadlamudi et al. 2004), becomes phosphorylated in the cell. The studies presented here show an overall conformational heterogeneity in apo-LC8 that is not restricted to the binding groove, but spans the sequence and is retained with IC binding but not with Swa binding. This raises the possibility that the conformational heterogeneity in apo-LC8 permits transient exposure of Ser 88 side chain for phosphorylation.

Using the same reasoning, it is also possible that the flexibility in the LC8•IC complex is retained to allow phosphorylation in the bound form, while no such regulation may be required for the LC8•Swa or LC8•Bim complexes.

Summary.

H55K is a model for monomeric LC8 at neutral pH and shows considerable conformational heterogeneity relative to the pH 3 WT monomer, primarily for residues that ultimately form the binding grooves at the dimer interface. The presence in the monomer of a few mostly disordered residues that sample ordered conformations suggests that dimerization and ligand binding selects for minor populations of native-like conformations in the inactive monomer ensemble. In both the monomer and dimer, β_3 is highly disordered, but is nevertheless more ordered on average in the dimer, and becomes considerably more ordered in the complex. Upon binding, β_3 makes contacts with the peptide that is itself intrinsically disordered but forms the 6^{th} strand in the complex (Barbar 2008), making this an example of two highly flexible segments (β_3 and $\beta_{peptide}$) that fold upon specific binding. Comparison of backbone dynamics between the two bound forms shows a more dynamic fit of IC relative to Swa in the binding groove and suggests that the increase in ordered structure observed in LC8 upon binding is peptide dependent. The difference in the entropic energetic cost associated with LC8 binding correlates with the large difference in LC8 backbone dynamics upon association with peptide partners and suggests that the conformational entropy of the protein modulates its affinity to diverse ligands. This raises the possibility that there are functional pressures on LC8 to tailor changes in its internal dynamics for different binding partners. Conformational heterogeneity may also underlie selective regulation by phosphorylation.

Materials and Methods

Protein Preparation.

Both unlabeled and uniformly ^{15}N or $^{15}N/^{13}C$ labeled LC8 and H55K were prepared from *Drosophila* gene products following methods described earlier (Makokha et al. 2004). Purity of > 95% was verified by SDS-PAGE and analytical size exclusion chromatography.

Synthetic peptides (Biosynthesis inc., Lewisville, TX) corresponding to Bim residues 48-64 (Bim), intermediate chain residues 123-138 (IC) and Swallow residues 281-297 (Swa) (Figure 2.2) were purified by high performance liquid chromatography on a YMC C-18 column in 0.1% trifluoroacetic acid with a linear gradient (10-30%) of acetonitrile with Bim, IC and Swa elution at 25%, 15% and 20%, respectively. Purity and molecular weight were verified by MALDI-TOF mass spectrometry: Bim M.W. = 1827.9 Da (1828.0 Da theoretical), IC M.W. = 1786.1 Da (1785.9 Da theoretical), and Swa M.W. = 1928.1 Da (1928.1 Da theoretical).

Unfolding Studies.

CD experiments were conducted on a JASCO 715 spectropolarimeter in a 1 mm cell for a protein concentration of 14 μM in 10 mM sodium phosphate buffer, 0.1 M NaCl, 5 mM TCEP at pH 7. Data were acquired at 310 °C following procedures and experimental conditions published elsewhere (Barbar et al. 2001). Intrinsic fluorescence emission spectra of the single tryptophan residue were determined on a Jobin Yvon/Spex spectrofluorometer at 30 ˚C.

The denaturation curves were analyzed using a two-state unfolding model (Santoro *et al.* 1988; Cheng *et al.* 1993; Fan *et al.* 1998):

$$M \overset{K_u}{\Leftrightarrow} U \qquad \text{(eq.1)}$$

where M and U are the folded and unfolded monomer, respectively. The two-state process was modeled by calculation of K_u and $\Delta G°$ at each point in the unfolding transition phase. K_u was calculated using equations 2 and 3:

$$K_u = \frac{[U]}{[M]} = \frac{f_u}{1 - f_u} \qquad \text{(eq.2)}$$

$$f_u = \frac{y_m - y}{y_m - y_u} \qquad \text{(eq.3)}$$

where f_u is the fraction of unfolded protein and y_m and y_u are the observed spectroscopic signals for the monomer and unfolded monomer, respectively. ΔG° was calculated as $-RT \ln K_u$, and linear extrapolation of ΔG° to 0 M guanidinium chloride (GdnCl) gives $\Delta G°_{H2O}$, the free energy of unfolding under standard conditions. The midpoint of the transition (C_m) was determined using the relation $C_m = \Delta G°_{H_2O} / m$. The fits were performed using a χ^2 procedure implemented in Microsoft Excel.

NMR Spectroscopy.

All NMR spectra were collected on a 600 MHz Bruker DRX spectrometer. LC8 and H55K samples were prepared at 1 mM protein concentration in 50 mM sodium phosphate and 50 mM sodium chloride at pH 6.7, and contained 1 mM DTT, maleic acid, sodium azide and protease inhibitor cocktail (Roche), 10 % (v/v) D_2O and 3% (v/v) glycerol. Experiments were collected at 30˚C. For LC8 and LC8•peptide comparison experiments, the protein concentration was 1 mM in 50 mM sodium phosphate, 50 mM sodium citrate and 100 mM sodium chloride at pH 5.5 and experiments were collected at 25˚C. The peptide to protein concentration ratio was greater than two-fold. The pH was measured before data acquisition and verified using an internal maleic acid standard. ^1H chemical shifts were referenced from an internal DSS signal at zero ppm (Wishart *et al.* 1995).

^1H-^{15}N HSQC spectra were recorded using States-TPPI phase discrimination of 256 increments defined by 128 scans and 1024 points. HNCA and CBCACONH experiments for H55K backbone assignments were performed with 1024 (H), 64 (C) and 20 (N) points. Resonance assignments were deposited in the BMRB with accession number 15953.

R_1, R_2 and steady state heteronuclear NOE spectra were recorded using the pulse sequence described by Farrow *et al.* (Farrow *et al.* 1994). R_1 relaxation

delays were 0.05, 0.1, 0.15, 0.02, 0.3, 0.5 and 1 s. R_2 relaxation delays were 15.8, 31.7, 63.4, 79.2, 95.0, 126.7 and 142.6 ms. At least one redundant data point was collected for R_1 and R_2 experiments. Steady state heteronuclear NOE experiments were recorded in the presence and absence of amide proton saturation with 240 complex points. Spectra with proton saturation used a 3 s period of saturation and an additional delay of 1.5 s.

Spectra were processed with NMRPipe (Delaglio *et al.* 1995) and analyzed with Burrow-Owl (Benison *et al.* 2007). Change in ^{1}H-^{15}N HSQC chemical shifts (ΔN-H) between LC8 and H55K was determined using the equation $\Delta N\text{-}H = [(\Delta^{1}H)^2 + (\Delta^{15}N)^2]^{½}$ after multiplying the ^{1}H chemical shift by 6.4 (fractional difference in ^{15}N:^{1}H spectral widths) to eliminate ^{15}N chemical shift bias (Wishart *et al.* 1992).

Dynamics Analysis.

Peak intensities were measured as peak heights with uncertainty estimated from baseline standard deviation within a 1.4×5 ppm rectangle of the spectrum. R_1 and R_2 data were fit using CurveFit version 1.3. Errors reported include both uncertainty in the peak height and the error of the exponential fit.

Peak intensities (I) as a function of delay time for R_1 and R_2 were fit to a single exponential $I=I_0 \mathbf{x} e^{-Rate \mathbf{x} t}$, where I_0 is the peak intensity extrapolated to time 0. NOE values were obtained from the ratios of peak intensities in the presence and absence of amide proton saturation. Uncertainty in the NOE value (σ) was determined using the equation $\sigma/NOE = [(\delta_{unsat}/I_{unsat})^2 + (\delta_{sat}/I_{sat})^2]^{1/2}$, where *I* and δ correspond to the peak intensity and the baseline noise, respectively.

Backbone amide relaxation parameters were analyzed with the extended Lipari-Szabo formalism (Lipari 1982; Clore 1990) using the program TENSOR2 (Dosset *et al.* 2001) to assess global tumbling and internal motions. The ^{15}N CSA was set to -170 ppm and the N-H bond length to 1.02 Å. For each data set, a global tumbling correlation time ($\boldsymbol{\tau}_m$) was calculated from the R_2/R_1 ratio of residues

assumed to have a negligible exchange contribution to ^{15}N relaxation following the criteria described by Tjandra *et al.* (Tjandra N. 1995). Residues in α_1 commonly failed the acceptance criteria as well as residues 87-89 for all five systems studied. For H55K, LC8 and LC8•IC, additional residues corresponding to the loop connecting α_2/β_2 (51-53), β_3 (61-69) and the loop connecting β_3/β_4 (70-74) were removed from global tumbling calculations, while for LC8•Swa only residue 62 was additionally omitted. Correlation times and rotational diffusion parameters were determined using Gaussian Monte Carlo simulations.

Internal motions were determined using Monte Carlo sampling methods and F-tests validation incorporated in TENSOR2 (Dosset et al. 2001). Five standard models were used to describe internal mobility with motion complexity increasing with model number. Model 1 motion is described by S^2; model 2 by S^2 and $\boldsymbol{\tau}_e$; model 3 by S^2 and R_{ex}; model 4 by S^2, $\boldsymbol{\tau}_e$ and R_{ex}; model 5 by S^2, $S_f{}^2$ and $\boldsymbol{\tau}_s$. S^2 is the order parameter and describes the amplitude of the N-H vector motion on the nanosecond-picosecond timescale, $\boldsymbol{\tau}_e$ is the effective correlation time for the internal motions and R_{ex} describes slow chemical exchange type motions on the millisecond-microsecond timescale (Mandel *et al.* 1995). Model 5 can account for internal motions occurring at two distinct timescales; $\boldsymbol{\tau}_s$ is the effective correlation time for the slow internal motions (Clore 1990). A model for the internal motions was rejected if the experimental χ^2 value was higher than the simulated χ^2 value at the 90% confidence limit. Residues in H55K, LC8, LC8•IC and LC8•Swa that were not adequately fit by any of the five models were omitted from further analysis. For anisotropic analyses, pdb codes 1RHW (Makokha et al. 2004), 2P2T (Benison et al. 2007) and 2P1K (Benison et al. 2007) were used for H55K, LC8•IC and LC8•Swa respectively, and a recent apo-LC8 crystal structure was used for the LC8 dimer (pdb 3BRI) (Benison 2008). To check for bias introduced from the structure, H55K, apo-LC8 and LC8•IC were reanalyzed using alternate structures: a single chain from the dimeric LC8 crystal structure (pdb 3BRI) for H55K, the NMR dimer structure (pdb 1F3C) (Fan et al. 2001) for apo-LC8, and the LC8•Swa

structure (pdb 2P1K) (Benison et al. 2007) for LC8•IC. For all cases the resultant D_{ratio} ($D_{\parallel}/D_{\perp}$), calculated global tumbling time and internal motions were the same within error as the values obtained using original structures (data not shown).

H/D and H/H Exchange.

Hydrogen/deuterium exchange (H/D) experiments for H55K and LC8 were collected at 25˚C in 50 mM sodium phosphate, 50 mM sodium citrate, 100 mM sodium chloride at pH 5.5. Samples prepared for H/D were flash frozen and lyophilized prior to addition of 100% D_2O. ^{1}H-^{15}N HSQC spectra were collected continuously for the first 18 hours and then once every day for 14 days. The deadtime of the experiment, defined as time between first exposure to D_2O and the middle of the first HSQC experiment, was 30 min. Peak intensities as a function of time were fit to $I = I_0 \times e^{-k \times t} + \Omega$, where t is the time following deuteration, k is the exchange rate, and Ω is a correction factor for baseline distortion and residual H_2O in the sample.

Hydrogen/Hydrogen (H/H) exchange spectra for H55K, LC8 dimer, and LC8•Swa were collected using the CLEANEX-PM-FHSQC pulse sequence (Hwang *et al.* 1998) at 30 ˚C in 50 mM sodium phosphate and 50 mM sodium chloride at pH 6.7 with a mixing time of 20 millisecond.

Isothermal Titration Calorimetry.

Bim, IC and Swa peptides and LC8 were prepared in buffer containing 50 mM sodium phosphate, 50 mM sodium citrate, 100 mM sodium chloride, 1 mM sodium azide at pH 5.5. The concentration of Bim was determined by weight of dry peptide on a CAHN 25 automatic elecrobalance, accurate to a thousandth of a milligram. The concentrations of IC and Swa were determined using sequence-based calculated ε_{280} of 1490 $M^{-1}\times cm^{-1}$. The concentration of LC8 was determined using ε_{280} of 13370 $M^{-1}\times cm^{-1}$.

Thermodynamics of binding were obtained using a VP-ITC isothermal titration calorimeter from MicroCal (Northampton, MA). Data were processed using the software package Origin 7.0 (OriginLab Corp., Northampton, MA). For each experiment, an initial injection of 2 µl was performed followed by 27 injections of 10 µl with a 300 s equilibration time between injections. The heat of dilution determined from titrating peptide into buffer at 30 and 35 °C was subtracted from the binding data prior to data fitting.

The stoichiometric number (n) was 1.00 ± 0.08 for all experiments using a syringe/cell concentration of 0.5/0.03 mM. The "c value" ($c = [protein]_{sample\ cell} \times K_d^{-1}$) was within the 5 to 500 value required for reliable determination of association constants (Turnbull *et al.* 2003). The error reported for Bim, IC and Swa associations to LC8 is based on deviation from the theoretical best fit.

Acknowledgements

We acknowledge the support of the nucleic acid and protein core and the mass spectrometry facilities and services core in the OSU Environmental Health Sciences Center (NIH/NIEHS 00210). The authors thank Serena Mills and Yujuan Song for sample preparation, Greg Benison for help with NMR data collection and analysis, and the rest of the Barbar lab for valuable discussion. The authors gratefully acknowledge advice from Professors Martin Blackledge and Art Palmer regarding model free analysis.

Chapter 3

Allostery and conformational entropy in LC8 binding

Justin Hall, Andrea Hall, and Elisar Barbar

Summary

Dynein light chain LC8[2] is a highly conserved protein which binds at least twenty different partners. Binding studies of LC8 in complex to short peptides from different partners show overall similar crystal structures and affinities, yet NMR measurements show distinct changes in LC8 backbone dynamics for these same partners. Here we present ITC and NMR data supporting an allosteric binding model for LC8 and a correlation between changes in binding entropy from ITC and changes in LC8 backbone dynamics, consistent with LC8 conformational entropy playing an important role in partner recognition.

Introduction

LC8 is a highly conserved and ubiquitous protein, it was first identified as a component of the dynein motor protein complex (Dick et al. 1996; King et al. 1996) where it binds to the intermediate chain (IC) of dynein (Lo et al. 2001; Makokha et al. 2002). Approximately 60% of cellular LC8 is not dynein bound (King et al. 1996), instead LC8 associates with at least twenty different partners where it is thought to aid in partner dimerization (Barbar 2008). LC8 is itself a homodimer, a cross over β-strand from each protomer creates two identical binding sites on opposite sides of LC8 at which binding partners associate as a β-strand (Benison et al. 2008) (Figure 3.1).

Structures have been determined for LC8 bound to peptides from IC, the proapoptotic Bcl2 family protein Bim, neuronal nitric oxide synthase (nNOS), p21-activated kinase-1 and the bicoid mRNA localization protein Swallow (Swa)

[2] LC8, 10 kDa dynein light chain; Bim, peptide corresponding to residues 48-64 from proapoptotic Bcl2 family protein Bim; IC, peptide corresponding to residues 123-138 of cytoplasmic dynein intermediate chain; nNOS, peptide corresponding to residues 233-249 of neuronal Nitric oxide synthase 1; Swa, peptide corresponding to residues 281-297 from Swallow protein; NMR; nuclear magnetic resonance; NOE, nuclear Overhauser effect; ITC, isothermal titration calorimetry; DSS, 2, 2-dimethylsilapentene-5-sulfonic acid.

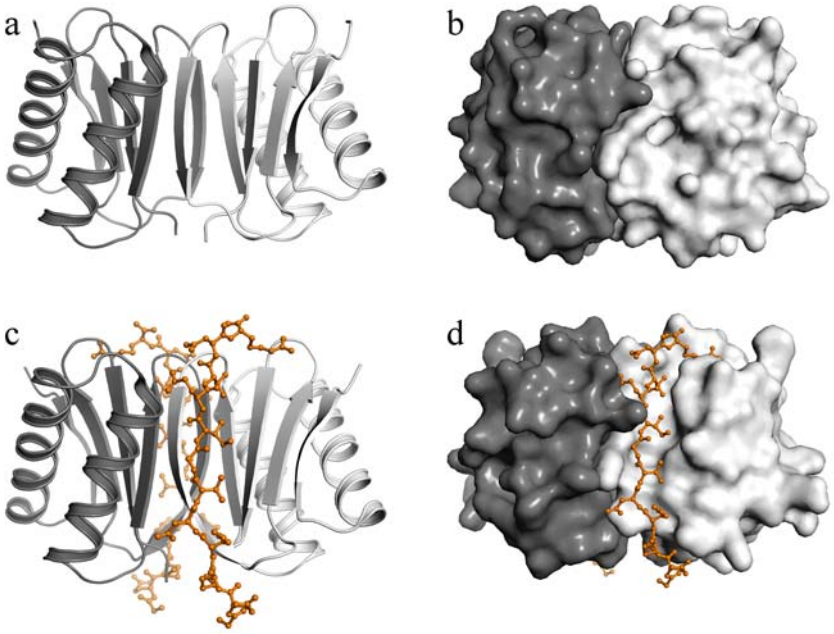

Figure 3.1: LC8 is a homodimer with two binding sites created by the LC8 dimer interface. a) Secondary structure and b) surface representation of homodimeric apo-LC8 (the two chains of LC8 are colored black and white). c) Secondary structure and d) surface representation of the nNOS•LC8 complex with nNOS (orange) shown as a ball and stick model. nNOS binds parallel to the LC8 2-fold symmetry axis at equivalent LC8 residues. The two nNOS peptides are 15 Å separate. Figures generated using Pymol (DeLano 2002) with pdb structures 3BRI (apo-LC8) (Benison et al. 2008), 1CMI (nNOS•LC8) (Liang et al. 1999).

(Liang et al. 1999; Fan et al. 2001; Benison et al. 2007; Williams et al. 2007; Lightcap et al. 2008). Each of these peptide•LC8 complexes has overall similar conformations despite different LC8 recognition sequences (Figure 3.2). Conversely, changes in LC8 backbone dynamics between apo-LC8 and LC8 bound to these same partners are distinct (Fan et al. 2002; Hall et al. 2008) and involve communication between the first and second binding site (Benison et al. 2008), suggesting changes in internal LC8 conformational entropy as well as allosteric interaction between the two binding sites may play an important role in partner recognition. To address the role of LC8 conformational dynamics in partner recognition, we used ITC and NMR to determine entropic changes between different peptides as well as between the first and second binding events for the same peptide. Our results show a correlation between changes in entropy from ITC and changes in LC8 backbone dynamics for Bim, IC, nNOS and Swa, and a large change in entropy between the first and second binding events for Bim and Swa. Altogether these results suggest changes in entropy measured by ITC may be due to peptide specific changes in LC8 conformational entropy.

Results and Discussion

LC8 binds its partners with distinct thermodynamic parameters.

For a protein with multiple binding partners, ITC can illuminate important thermodynamic differences between partners. There are twenty different partners known to associate with LC8; comparison of thermodynamic association parameters for LC8 binding to peptides from four of these partners (Bim, IC, nNOS and Swa) shows that while each of these partners binds with similar affinities, the thermodynamic contributions of each are distinct (Table 3.1).

LC8 is a homodimer with two symmetric binding sites parallel to the LC8 2-fold axis (Figure 3.1). When two peptides bind to LC8, they interact with equivalent LC8 residues on opposite sides of the LC8 homodimer, and are held 15 Å apart at their closest point. Thus based on structural analysis of LC8 in complex

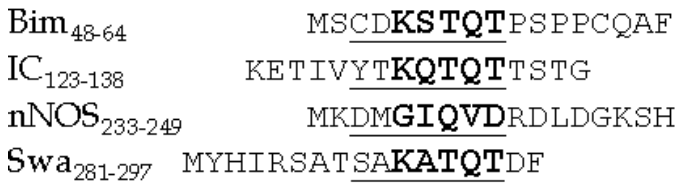

Figure 3.2: Peptide sequences used in this study. The sequence of Bim, IC, nNOS and Swa peptides are shown with the KXTQT or GIQVD motif in bold and the segment that forms a β-strand underlined.

Table 3.1: Thermodynamic association parameters for LC8 binding to Bim, IC, nNOS and Swa peptides at 10 °C.

Interaction		K_{d1}	K_{d2}	$\Delta G°_1$	$\Delta G°_2$	$\Delta H°_1$	$\Delta H°_2$	$-T\Delta S°_1$	$-T\Delta S°_2$
Syringe	**Cell**	**(μM)**	**(μM)**	**(kcal/mol)**	**(kcal/mol)**	**(kcal/mol)**	**(kcal/mol)**	**(kcal/mol)**	**(kcal/mol)**
Bim[a]	LC8	0.4 ±0.1	0.3 ±0.1	-8.3 ±0.2	-8.4 ±0.2	-6.3 ±0.8	-9.8 ±1.0	-2.0 ±0.7	1.4 ±1.1
IC[b]	LC8	4.3 ±0.9		-7.0 ±1.5		1.1 ±0.1		-8.1 ±1.5	
nNOS[b]	LC8	3.9 ±0.3		-7.0 ±0.6		2.4 ±0.1		-9.4 ±0.5	
Swa[c]	LC8	0.2 ±0.1	0.3 ±0.1	-8.6 ±0.2	-8.5 ±0.1	-6.9 ±0.3	-11.2 ±0.6	-1.7 ±0.5	2.7 ±0.7
LC8[d]	Bim	0.2 ±0.1		-8.8 ±0.2		-8.3 ±0.3		-0.5 ±0.2	
LC8[d]	Swa	0.2 ±0.1		-8.9 ±0.1		-8.6 ±0.1		-0.3 ±0.1	

[a]Values are the average of six experiments with error estimation from standard deviation between repeats.
[b]Values are from one experiment with error estimation based on data deviation from the theoretical best fit.
[c]Values are the average of seven experiments with error estimation from standard deviation between repeats.
[d]Values are the average of two experiments with error estimation based on data deviation from the theoretical best fit.

to peptides from Bim, IC, nNOS and Swa, LC8 may bind the two peptide chains independently, with no communication between first and second binding events.

To test for independent binding, ITC experiments capable of measuring the thermodynamic association parameters of the first and second peptide binding events were performed. In the first experiments, peptides from Bim, IC, nNOS and Swa were titrated into a sample cell containing LC8. During the first few injections of these experiments, the initial concentration of apo-LC8 in the sample cell was significantly higher than the concentration of singly-bound LC8, allowing measurement of the apo-LC8 to singly-bound LC8 transition (first binding event). Subsequent injections contained increasing concentrations of singly-bound LC8, allowing measurement of the singly-bound to doubly-bound transition (second binding event). In these experiments, if the two binding events are independent, no thermodynamic difference will be observed between the first few injections and subsequent injections (Figure 3.3a) (Houtman *et al*. 2006; Popovych *et al*. 2006; Houtman *et al.* 2007). Interestingly, both IC and nNOS titrated into LC8 at 10 °C are entropically driven ($-T\Delta S° = -8.1$ and -9.4 kcal/mol, respectively) with seemingly independent binding events (Figure 3.4b, c) whereas Bim and Swa are enthalpically driven ($\Delta H° = -8.3$ and -8.6 kcal/mol, respectively) with thermodynamic differences between the first few injections and subsequent injections. These results suggest allosteric communication may occur between the first and second binding events for Bim and Swa (Figure 3.4a, d) (Gorshkova *et al.* 1995; Popovych et al. 2006; Toke *et al.* 2006).

To ensure the differences observed for Bim and Swa were due to thermodynamic difference between the first and second binding events, orthogonal control experiments were performed with LC8 and peptide positions reversed (Houtman et al. 2006; Houtman et al. 2007). In these experiments LC8 is titrated into a sample cell containing saturating concentrations of peptide, thereby preventing the accumulation of singly-bound LC8 (Figure 3.3b). Since the first and second binding events are not resolved in these experiments, the thermodynamic

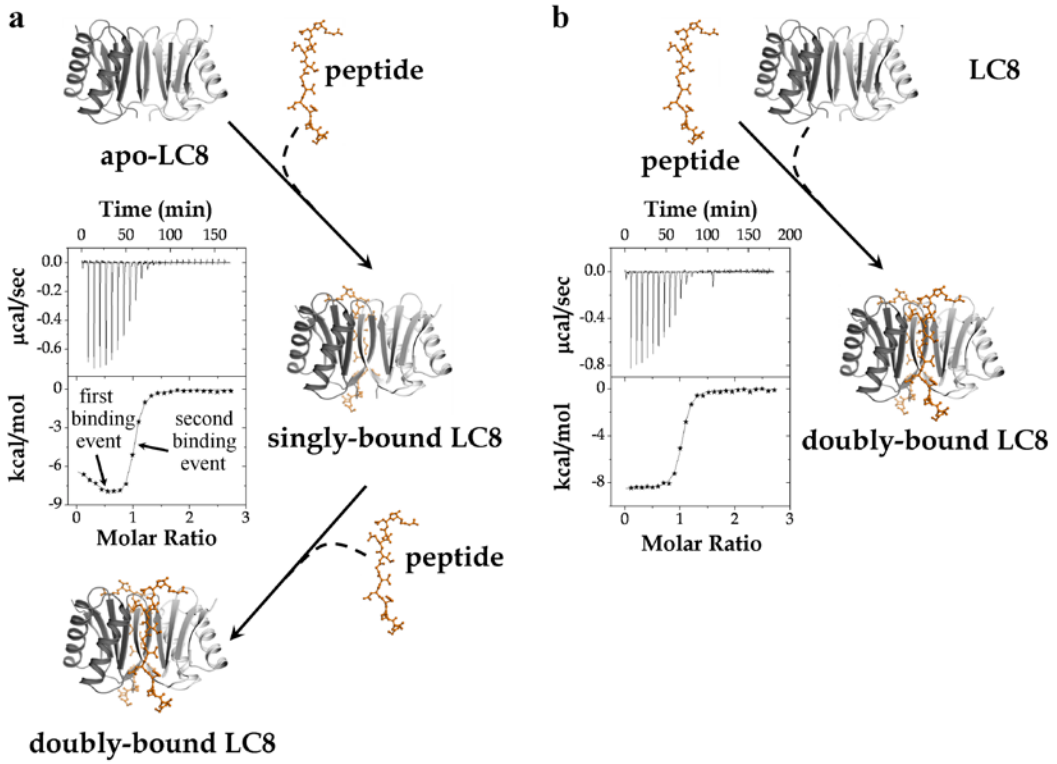

Figure 3.3: ITC can resolve individual steps for sequential binding. a) For a monomeric peptide (orange) titrated into a sample cell containing LC8 (the two protomers of LC8 are colored black and white), binding creates a singly-bound LC8 in the first injection, followed by formation of doubly-bound LC8 in subsequent injections. b) For the orthogonal experiment where LC8 is titrated into a sample cell containing peptide, singly-bound LC8 is not accumulated; instead measured thermodynamic association parameters are an average of the first and second binding events. Figures generated using Pymol (DeLano 2002) with pdb structures 3BRI for apo-LC8 (Benison et al. 2008) and 1CMI for singly and doubly-bound LC8 (Liang et al. 1999).

association parameters are an average of the first and second binding events. Consistent with theoretical expectations, the orthogonal ITC data for Bim and Swa show no thermodynamic differences between the first few injections and subsequent injections (Figure 3.4f, h).

To determine the thermodynamic association parameters for the first and second binding event for Bim or Swa binding to LC8, ITC data for Bim or Swa titrated into LC8 were globally fit by a two-site binding model of the **A + A + B → A + AB → ABA** type (where **A** and **B** refer to a single chain of peptide and a dimer of LC8, respectively) which allows for allosteric interactions between the first and second binding events (Figure 3.4e, g) (Houtman et al. 2007). For Bim and Swa, the second binding event occurs with a favorable increase in enthalpy of the system ($\Delta\Delta H°$ = -3.5 and -4.3 kcal/mol, respectively) consistent with the more negative enthalpy observed after the first injection, but an unfavorable decrease in enthalpy of the system ($\Delta(-T\Delta S°)$ = 3.4 and 4.4 kcal/mol, respectively) resulting in equivalent affinities for the first and second binding events ($\Delta\Delta G°$ = 0.1 kcal/mol). The average of the thermodynamic association parameters of the first and second binding events are in good agreement with values from the orthogonal experiments (Table 3.1). The differences in thermodynamic association parameters between the first and second peptide binding events show that despite no direct peptide•peptide contact for Bim and Swa, the first and second peptide binding events are communicated to each other.

LC8 retains much of its backbone heterogeneity upon nNOS binding.

Changes in ^{15}N-backbone dynamics between apo and bound-LC8 are a direct measure of changes in entropy upon peptide binding. $\boldsymbol{\tau}_e$ and R_{ex} are two separate measures of protein entropy occurring on fast and intermediate timescales respectively. $\boldsymbol{\tau}_e$ describes contributions to motion between states separated by small energetic barriers with fast exchange rates (ps-ns), such as might exist within a broad energy well, while R_{ex} describes contributions to motion between states

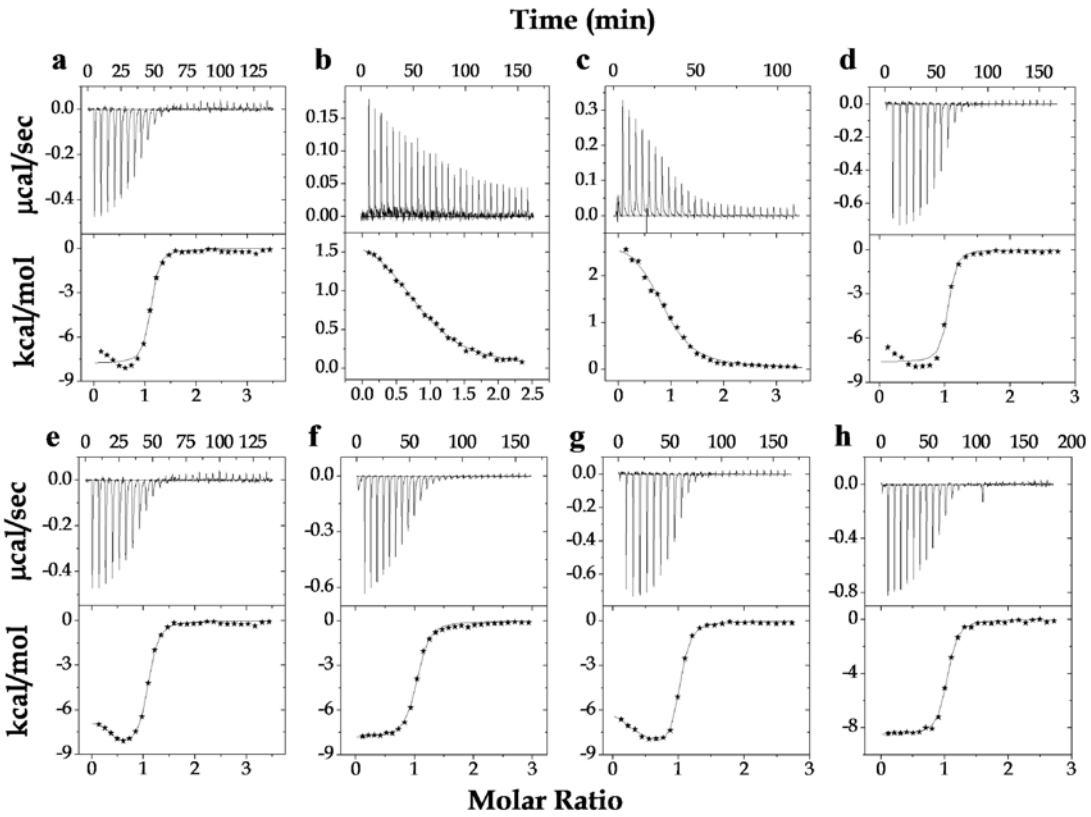

Figure 3.4: LC8 binds different partners with distinct thermodynamic association parameters. a) Representative ITC thermograms (top panels) and binding isotherms (bottom panels) for Bim, b) IC, c) nNOS and d) Swa peptides titrated into LC8 at 10 °C. Bim and Swa data are not well fit by a single-site binding model (solid line in the bottom panel) indicating the first and second binding event have different binding enthalpies. e) Orthogonal experiments with Bim titrated into LC8, f) LC8 titrated into Bim, g) Swa titrated into LC8 and h) LC8 titrated into Swa at 10 °C show biphasic and monophasic binding profiles for peptide titrated into LC8 and LC8 titrated into peptide, respectively. Data in panels e) and h) are the same data shown in a) and d), but are well fit here using a two-site binding model (solid line in the bottom panel).

separated by larger energetic barriers with slow exchange rates (μs-ms), such as might exist between two equally stable energy wells.

When IC binds to LC8, only a small decrease in $\boldsymbol{\tau}_e$ and R_{ex} contributions to backbone heterogeneity are observed (Hall et al. 2008), but a large decrease in $\boldsymbol{\tau}_e$ and R_{ex} contributions to backbone heterogeneity occurs for Bim (Fan et al. 2002) or Swa binding (Hall et al. 2008), with Swa binding causing a cessation of almost all $\boldsymbol{\tau}_e$ and R_{ex} motions. Similar to IC binding, the nNOS•LC8 complex retains some $\boldsymbol{\tau}_e$ and R_{ex} contributions to backbone heterogeneity, particularly in residues of β_1 and β_3 (Figure 3.5). The retention of fast and intermediate timescale motion in the nNOS•LC8 complex is therefore consistent with ITC thermodynamics measurements showing IC and nNOS binding is entropically favorable relative to Bim or Swa binding.

Conclusions.

There is a strong correlation between total system entropy measured by ITC, and LC8 specific changes in entropy measured by NMR (Table 3.1). Thermodynamic association parameters measured by ITC are for all components of a system, therefore there is no *a priori* reason why changes in entropy of the system for different LC8 binding partners should necessarily correlate to changes in LC8 backbone dynamics. Nevertheless, the correlation observed here indicates changes in total entropy of the system may be largely due to changes in the internal entropy of LC8 between different binding partners, as has been observed for other proteins (Frederick et al. 2007).

For Bim and Swa binding, NMR shows a large decrease in LC8 backbone entropy. ITC data for these two peptides shows the first and second binding events to be distinct, with a large unfavorable entropic change occurring for the second binding event. These results therefore suggest the NMR measured decrease in LC8 conformational entropy may occur during the second binding event for these peptides. Since a favorable change in enthalpy accompanies the unfavorable

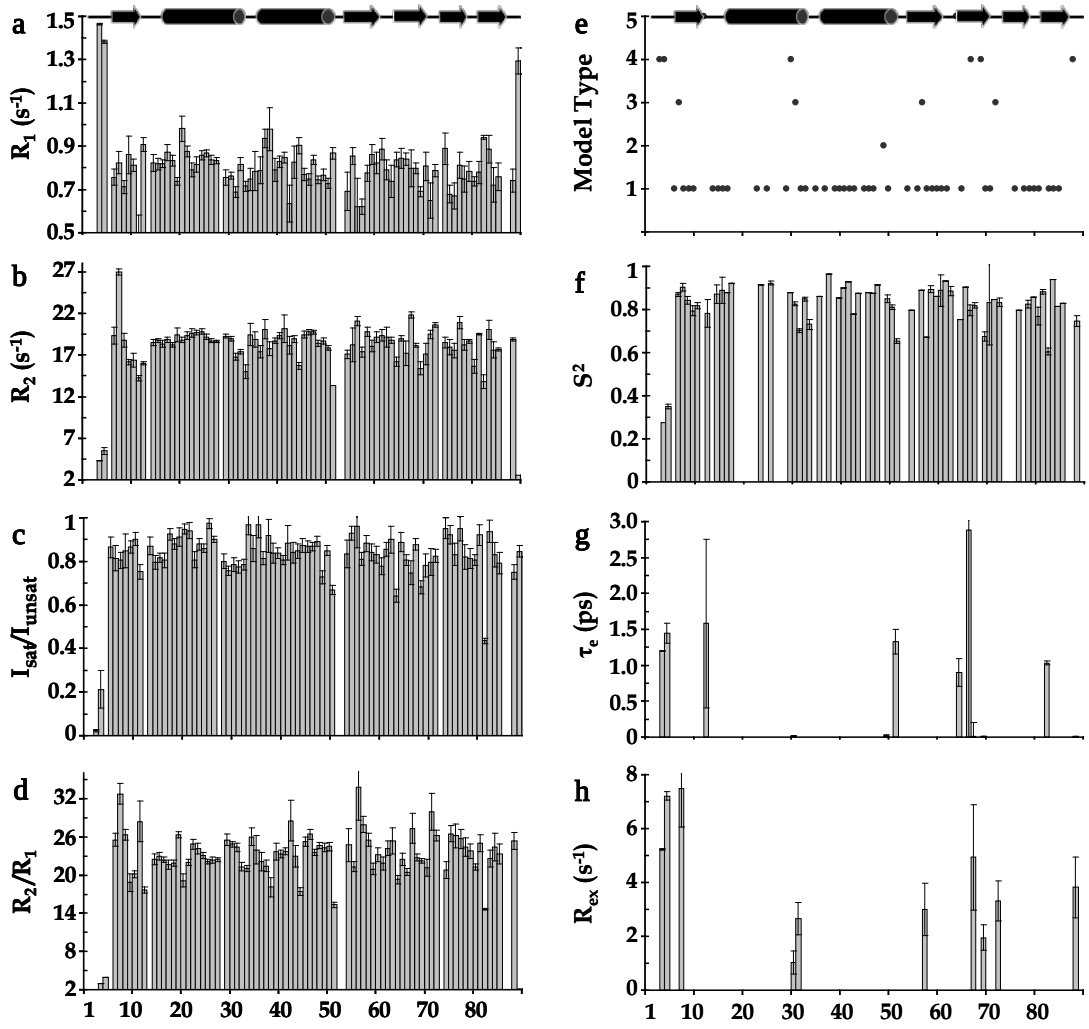

Figure 3.5: LC8 retains τ_e and R_{ex} contributions to backbone heterogeneity after nNOS binding. Plots of a) R_1, b) R_2, c) steady-state ^1H, ^{15}N-NOE and d) R_2/R_1 dynamics data verses residue. Model free analysis with e) model type, f) S^2, g) τ_e and h) R_{ex} parameters verses residue. Secondary structure elements of LC8 are shown above the graphs. Data for the nNOS•LC8 complex was collected at 25 °C, pH 5.5.

change in entropy of the second binding event, the parsimonious interpretation is that the second binding event maybe locking LC8 into a lower entropic state as a consequence of formation of favorable electrostatics satisfied in fewer LC8 conformations.

Materials and Methods

LC8 was prepared following methods described earlier (Makokha et al. 2004). Synthetic peptide (Biosynthesis Inc., Lewisville, TX) corresponding to residues 48-64 (numbering relative to *Homo sapiens*) of BCL2L11 (Bim), residues 123-138 (numbering relative to *Drosophila melanogaster Cdic*2b gene form) of the intermediate chain (IC) of dynein, residues 233-249 (numbering relative to *H. sapiens*) of neuronal nitric oxide synthase 1 (nNOS) and residues 281-297 (numbering relative to *D. melanogaster*) of Swallow protein (Swa) were purified following methods previously described (Hall et al. 2008).

Binding enthalpy experiments were carried out using a VP-ITC isothermal titration calorimeter from MicroCal (Northampton, MA). Data were processed using the manufacturer's supplied software package, Origin 7.0 (OriginLab Corp., Northampton, MA). Heats of dilution, determined from titrating protein into buffer, were subtracted from the binding data prior to fitting.

Experiments with IC or nNOS in the syringe and LC8 in the sample cell, and experiments with LC8 in the syringe and Bim or Swa in the sample cell, displayed monophasic binding behavior and were accurately fit using the SEDPHAT single-site binding model: $\mathbf{A + B \rightarrow AB}$, where **A** refers to a single protein chain in the syringe and **B** refers to a single protein chain in the cell (Houtman et al. 2007). Experiments with Bim or Swa titrated into the sample cell containing LC8 displayed biphasic binding behavior and were accurately fit using the SEDPHAT two-site binding model: $\mathbf{A + A + B \rightarrow A + AB \rightarrow ABA}$, where **A** refers to a single chain of Bim or Swa and **B** refers to a dimer of LC8. For all experiments the "c value" ($c = [\text{protein}]_{\text{sample cell}} \times K_d^{-1}$) was within the 5 to 500

range required for reliable determination of association constants using a syringe/cell concentration of 0.5/0.03 mM (Turnbull et al. 2003). Thermodynamic association parameters for LC8 binding to Bim, IC, nNOS and Swa in 50 mM sodium phosphate, 50 mM sodium citrate, 50 mM sodium chloride, 1 mM sodium azide, pH 5.5 at 10 °C are reported in Table 3.1.

NMR spectra for the nNOS•LC8 complex were collected and analyzed following methods previously described to allow direct comparison to LC8 in complex with other peptides (Hall et al. 2008). Briefly, nNOS•LC8 samples were prepared with 5 mM unlabelled nNOS and 1 mM ^{15}N-labeled LC8 at pH 5.5. Experiments were conducted at 25 ˚C and ^{1}H chemical shifts were referenced from an internal DSS signal at zero ppm (Wishart et al. 1995). HNCA and CBCACONH experiments for nNOS•LC8 backbone assignments were performed with 1024 (H), 64 (C) and 20 (N) points and have been deposited in the BMRB with accession code 16847. R_1, R_2 and steady state heteronuclear NOE spectra were recorded using the pulse sequence described by Farrow *et al.* (Farrow et al. 1994), processed with NMRPipe (Delaglio et al. 1995) and analyzed with Burrow-Owl (Benison et al. 2007). R_1 and R_2 were fit using CurveFit v1.3.

Relaxation parameters were analyzed with the extended Lipari-Szabo formalism (Lipari 1982; Clore 1990) using TENSOR2 (Dosset et al. 2001). The global tumbling correlation time ($\boldsymbol{\tau}_m$) was calculated from the R_2/R_1 ratio for qualifying residues (Tjandra N. 1995). Correlation times and rotational diffusion parameters were determined using Gaussian Monte Carlo simulations. A model for internal motions was rejected if the experimental χ^2 value was higher than the simulated χ^2 value at a 90% confidence level. For anisotropic analyses, pdb code 1CMI (Liang et al. 1999) was used to fit nNOS•LC8 data.

Acknowledgements

The authors thank Peter Schuck for help with SEDPHAT data analysis.

Chapter 4

Multivalency in the assembly of intrinsically disordered dynein intermediate chain

Justin Hall, P. Andrew Karplus and Elisar Barbar

Published in *Journal of Biological Chemistry*,
2008, 284 (48), 33115-33121

Summary

Dynein light chains are thought to increase binding efficiency of dynein intermediate chain to both dynein heavy chain and dynactin, but their exact role is not clear. Isothermal titration calorimetry and x-ray crystallography reported herein indicate that multivalency effects underlie efficient dynein assembly and regulation. For a ternary complex of a 60-amino acid segment of dynein intermediate chain (IC)[3], bound to two homodimeric dynein light chains Tctex1 and LC8, there is a 50-fold affinity enhancement for the second light chain binding. For a designed IC construct containing two LC8 sites, the 1000-fold enhancement observed reflects a remarkably pure entropic chelate effect of a magnitude commensurate with theoretical predictions. The lower enhancement in wild-type IC is attributed to unfavorable free energy changes associated with incremental interactions of IC with Tctex1. Our results show assembled dynein IC as an elongated, flexible polybivalent duplex, and suggest that polybivalency is an important general mechanism for constructing stable yet reversible and functionally versatile complexes.

Introduction

Cytoplasmic dynein is a 1.2 MDa microtubule-associated motor protein complex involved in Golgi maintenance, nuclear migration, mitotic spindle formation, and organelle positioning and transport (Vallee *et al.* 2004). Dynein has multiple subunits in the 10-500 kDa molecular weight range (Pfister *et al.* 2006): two heavy chains, two light intermediate chains (LIC), two intermediate chains (IC), and three light chains known in *Drosophila melanogaster* as Tctex1, LC8,

[3]The abbreviations used are: Tctex1; the 12 KDa dynein light chain corresponding to gene *dynlt1*; LC8, the 10 kDa dynein light chain corresponding to gene *dynll*; IC, the 74 kDa dynein intermediate chain corresponding to gene *dync1i2*; IC_L, IC residues 123-138; IC_{TL}, IC residues 84-143; IC_{LL}, IC residues 84-143 with residues 111-120 (SVYNVQATNI) replaced with residues 126-135 (LVYTKQTQTT); ITC, isothermal titration calorimetry.

and LC7. The three light chains are homodimers when active, and each binds at a separate site on the N-terminal domain of IC (Figure 4.1a).

Molecular genetic analyses in *D. melanogaster* indicate that IC serves an essential function (Boylan et al. 2002), consistent with its multiple roles in dynein assembly, regulation, and binding to cargo. Its C-terminal domain (C-IC) provides the sites for assembly of heavy chains, whereas its N-terminal domain (N-IC) provides binding sites for diverse light chains, for the $p150^{Glued}$ subunit of dynactin (King et al. 2000; Kardon et al. 2009), and for several other proteins presumed to be cellular cargo such as herpes simplex virus capsid protein (Ye et al. 2000), the ClC-2 chloride channel (Dhani et al. 2003) and β-catenin (Ligon et al. 2001). *In vivo* disruption of dynein dynactin interaction affects Golgi complex and endosome organization (Ma et al. 1999; Vaughan *et al.* 2001). *In vitro* studies of various segments of N-IC indicate that it is natively disordered and monomeric (Makokha et al. 2002; Nyarko et al. 2004); two N-IC chains bind to both Tctex1 and LC8, and within each chain the 10-12 amino acid recognition sequence undergoes a disorder-to-order transition (Benison et al. 2006) to form a β-strand incorporated into a β-sheet at the light chain dimer interface (Figure 4.1 and Appendix Figure A1.1) (Benison et al. 2007; Williams et al. 2007).

Tctex1 and LC8 are homologs (Appendix Figure A1.1) that bind at adjacent highly conserved IC recognition sequences (Appendix Table A1.1). In addition to binding IC, both associate with a wide variety of proteins once presumed to be dynein cargo linked by Tctex1 or LC8 to the dynein motor. However, recent structural data (Benison et al. 2007; Williams et al. 2007) challenge this view because the LC8 dimer (and by analogy the Tctex1 dimer (Williams et al. 2007)) binds either two chains of IC *or* two chains of putative cargo proteins at the same location (Wang et al. 2004; Benison et al. 2007), making the adaptor hypothesis much less attractive. An alternative hypothesis is that LC8 is a hub protein essential for promoting the dimerization and physiological activity of its diverse protein partners, including IC (Barbar 2008).

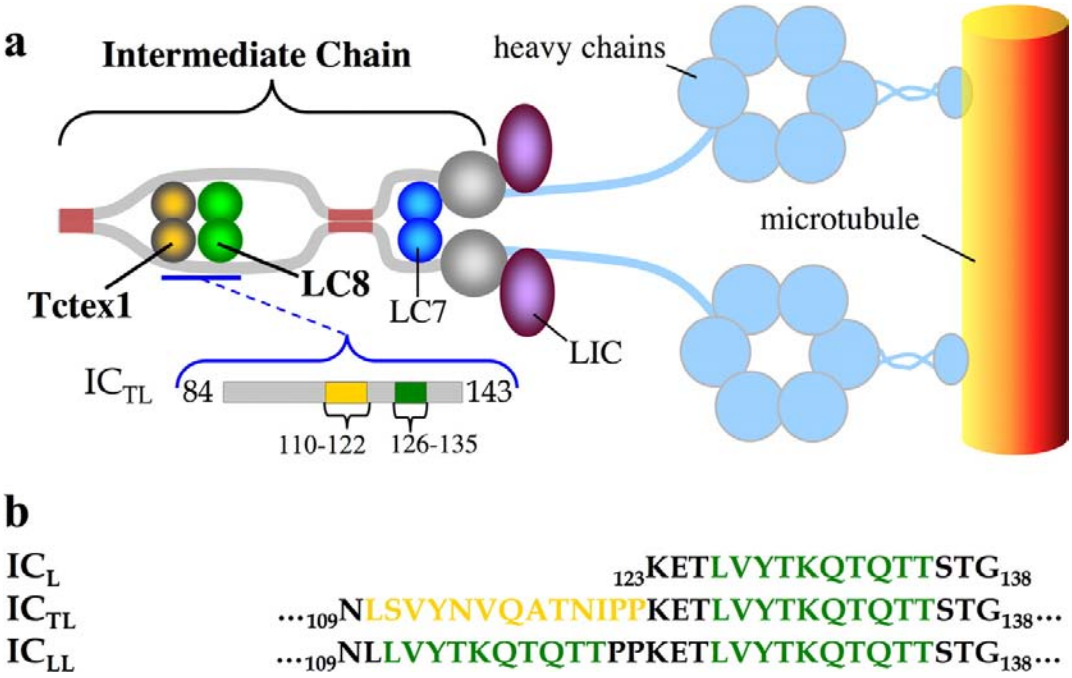

Figure 4.1: Schematic representation of cytoplasmic dynein and of IC constructs used in this study. a) The cytoplasmic dynein core is shown as an assembly of six proteins: the N-terminal domain of IC (grey bars, predicted coiled-coils shown with red hashes) is natively disordered; the C-terminal domain of IC (grey spheres) is predicted to be ordered; three homodimeric light chains are Tctex1 (yellow), LC8 (green) and LC7 (blue). In mammals, the corresponding light chains are DYNLT, DYNLL and DYNLRB, respectively (Pfister *et al.* 2005). Also shown are the light intermediate chains (LIC, purple), the heavy chain (light blue) and a microtubule (orange). The motor region of dynein consists of the heavy chain subunits which form a ring of AAA+ domains (Burgess et al. 2003) and a microtubule binding domain attached to the AAA+ ring by a flexible 15-nm coiled-coil stalk (Carter et al. 2008). An enlargement of the IC segment from residue 84-143 (dark blue brackets) has residues colored yellow and green indicating the recognition sequences for Tctex1 and LC8, respectively. b) The three IC constructs IC_L, IC_{TL} and IC_{LL} are, respectively, IC residues 123-138, IC residues 84-143, and IC residues 84-143 with the residues 111-120 replaced by a second copy of the LC8 binding sequence.

Such a regulatory role for these light chains in dynein assembly has been suggested based on the evidence that LC8 binding induces IC•IC self-association (Benison et al. 2006), and that the binding affinity of LC8 to IC is enhanced when Tctex1 is present (Williams et al. 2007). *In vivo* studies (King et al. 2003) of various truncations of N-IC show that an IC lacking the light chains recognition sequences binds less efficiently to $p150^{Glued}$ and is less effective at inhibiting dynein-based transport than a longer IC containing the light chain recognition sequences and the second predicted coiled-coil. In such experiments, overexpressed IC is presumed to bind free dynactin and competes with endogenous dynein IC resulting in perturbed microtubule organization and centrosome integrity. A similar experiment with deletions of N-IC shows the intact C-IC is not sufficient for efficient binding to the heavy chain, but requires both light chain binding sites and the second coiled-coil (Ma et al. 1999). The importance of both light chains for dynein function is documented; unknown are the mechanisms by which the two light chains work together to enhance the binding of IC to $p150^{Glued}$ on one end and to the dynein heavy chain on the other.

To determine the potential role of Tctex1 and LC8 in IC assembly and regulation, we measured the thermodynamics of formation of the IC•Tctex1•LC8 system, along with the model system IC•LC8•LC8. Mutual enhancement was expected as prior binding of IC to either light chain produced a bivalent IC duplex. The thermodynamics of these complexes and the structural organization of IC promote the formation of an IC duplex that serves as a poly-bivalent scaffold for dynein assembly and illustrate a novel aspect of the LC8 driven dimerization of a new class of intrinsically disordered proteins.

Results

Design of IC constructs.

Three IC constructs were used (Figure 4.1b): IC_{TL} – a wild-type sequence corresponding to IC residues 84-143 with both Tctex1 and LC8 recognition

sequences (T and L refer to sites for binding Tctex1 and LC8, respectively); IC_{LL} – a mutated version of the same segment with the Tctex1 recognition sequence replaced by the LC8 recognition sequence; and IC_L – a shortened sequence corresponding to IC residues 123-138 with only one LC8 recognition sequence. The IC_{TL}, IC_{LL} and IC_L constructs do not include the IC regions predicted to be coiled-coils (Benison et al. 2006). LC8 and Tctex1 bind the longer IC constructs that contain either predicted coiled-coil with similar affinity as IC_{TL} (data not shown) and therefore for simplicity and for ease of comparison of ITC and X-ray crystallography data, these studies focus on IC_{TL}. The apo-IC constructs used are all monomeric and disordered, whereas both Tctex1 and LC8 are dimeric and bind two monomers of IC. When fully assembled, the complexes formed by the IC constructs are, respectively, IC_{TL}•Tctex1•LC8, IC_{LL}•LC8•LC8, and IC_L•LC8.

Thermodynamics of IC_{TL}•Tctex1•LC8 complex formation.

Representative isothermal titration calorimetry (ITC) data are shown in Figure 4.2. Association parameters ($\Delta G°$, $\Delta H°$, $-T\Delta S°$) and the related heat capacity change (ΔCp_{exp}) are given in Table 4.1 and Appendix Figure 1.2. For IC_{TL}, we measured the binding of Tctex1 to both apo-IC_{TL} and to the pre-bound IC_{TL}•LC8 complex and similarly the binding of LC8 to apo-IC_{TL} and to pre-bound IC_{TL}•Tctex1. Control experiments showed that in the absence of IC there is no interaction between Tctex1 and LC8 (data not shown).

Apo-IC_{TL} binds Tctex1 or LC8 with similar affinity (K_d of 8 μM), and a ΔCp_{exp} of -0.42 and -0.26 kcal/mol/K, respectively (Table 4.1, Appendix Figure A1.2b, c). When IC_{TL} is pre-bound to either Tctex1 or LC8, the second light chain binds with higher affinity (K_d of 0.2 μM), and results in a more negative ΔCp_{exp} of -0.59 and -0.41 kcal/mol/K, for Tctex1 and LC8 respectively (Table 4.1, Appendix Figure A1.2d, e). Between the first and second binding events, there is a 50-fold ($\Delta\Delta G°$ of -2.4 kcal/mol) binding affinity enhancement accompanied by a change in ΔCp_{exp} ($\Delta\Delta Cp_{exp}$ of -0.16 kcal/mol/K). The more negative ΔCp_{exp} suggests

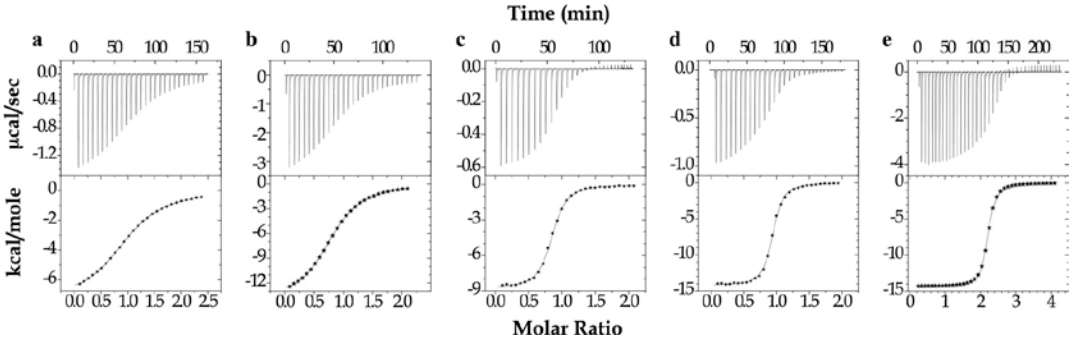

Figure 4.2: Representative ITC data for IC constructs binding to Tctex1 and LC8. Thermograms (top panels) and binding isotherms (bottom panels) are shown for the titration of apo-IC_{TL} with a) Tctex1 and b) LC8, the titration of pre-bound IC_{TL} with c) Tctex1 and d) LC8, and e) the titration of IC_{LL} with LC8. Solid lines correspond to the non-linear least squares fit for an **A + B→ AB** binding model. Data were collected at 25 °C in 50 mM sodium phosphate, 50 mM sodium chloride, pH 7.5.

Table 4.1: Thermodynamic parameters for association of IC constructs with dimeric LC8 and Tctex1 at 25 °C[a].

Interaction		K_d	$\Delta G°$	$\Delta H°$	$-T\Delta S°$	ΔCp_{exp}	ΔCp_{calc}[b]
Protein	**Ligand**	**(μM)**	**(kcal/mol)**	**(kcal/mol)**	**(kcal/mol)**	**(kcal/mol/K)**	**(kcal/mol/K)**
LC8	IC_L	8.0 ±2.1	-7.0 ±0.1	1.1 ±0.3	-8.1 ±0.4	-0.26	-0.27
Tctex1	IC_{TL}	9.6 ±3.6	-6.8 ±0.2	-6.9 ±0.8	0.1 ±0.5	-0.42	-0.56[c]
LC8	IC_{TL}	8.0 ±1.5	-7.0 ±0.1	-13.7 ±0.6	6.7 ±0.2	-0.26	-0.27
Tctex1	IC_{TL}/LC8	0.21 ±0.09	-9.1 ±0.2	-8.8 ±0.3	-0.3 ±0.7	-0.59	-0.56
LC8	IC_{TL}/Tctex1	0.13 ±0.09	-9.4 ±0.3	-14.5 ±0.3	5.2 ±0.4	-0.41	-0.25
LC8	IC_{LL}	0.50 ±0.06	-9.0 ±0.1	-13.7 ±0.2	4.8 ±0.2	-0.26	-0.25

[a]Average values are reported with error estimated as the standard deviation of replicates. The binding stoichiometry (n) was 1.04 ± 0.08 for IC_L, 0.96 ± 0.07 for IC_{TL}, and 2.06 ± 0.05 for IC_{LL}. All data were fit to one monomer of either light chain binding to a single IC chain.

[b]ΔCp_{cal} values were computed as described by Spolar and Record (Spolar *et al.* 1994) based on the surfaces buried by a light chain monomer binding to a single IC chain.

[c]No structure is reported for IC with Tctex1 in the absence of LC8, so ΔCp_{calc} for apo-IC_{TL}•Tctex1 was determined from the WT IC•Tctex1•LC8 complex (3FM7).

additional burial of surface area accompanies the second binding event (Spolar et al. 1994).

Interestingly, LC8 binds IC_L and apo-IC_{TL} with indistinguishable affinities and ΔCp_{exp} values (Table 4.1) indicating that binding is limited to the short recognition sequence of IC and that there is no change in rigidity of IC not in direct contact with LC8.

Thermodynamics of IC_{LL}•LC8•LC8 complex formation.

To examine the origin of the binding enhancement associated with pre-bound IC_{TL} relative to apo-IC_{TL}, we engineered an IC construct, $IC_{LL,}$ that has the Tctex1 binding site replaced with the LC8 recognition sequence, giving two sites for binding dimeric LC8 (Figure 4.1b). IC_{LL} serves a dual purpose, allowing the investigation of the thermodynamics of binding enhancement in a simplified system, and also probing the biological relevance of two contiguous sites on IC for two distinct proteins, Tctex1 and LC8, instead of two copies of a single protein given that there exists real protein systems with two or more adjacent LC8 sites. The latter point is intriguing given that Tctex1 and LC8 are homologs with similar tertiary and quaternary structures (Appendix Figure A1.1), and similar binding affinity to IC.

Binding of IC_{LL} to LC8 to form IC_{LL}•LC8•LC8 was measured using ITC. For strong positive enhancement, as expected between the first and second LC8 dimer binding, ITC cannot resolve individual binding events, so the data were fit to a single binding event with a macroscopic K_d of 0.5 μM and a stoichiometry of two IC_{LL} chains per two LC8 dimers (Figure 4.2e, Appendix Figure A1.2f). The single binding event model with $\Delta G°$ of -9.0 kcal/mol, $\Delta H°$ of -13.7, $-T\Delta S°$ of 4.8 kcal/mol and a ΔCp_{exp} of -0.26 kcal/mol/K corresponds to the average of the two binding events. However, distinct thermodynamic parameters for each binding event can be separated if the first binding is assumed to have thermodynamic parameters similar to LC8 binding to apo-IC_{TL}. This assumption is reasonable

because the value for ΔCp_{exp} of -0.26 kcal/mol/K for LC8 with IC_{LL} is the same as for LC8 with IC_L and apo-IC_{TL} (Table 4.1). Using this reasoning, the inferred thermodynamic parameters for the second binding event are a K_d of 0.01 μM, $\Delta G°$ of -11.0, $\Delta H°$ of -13.7, $-T\Delta S°$ of 2.8 kcal/mol and a ΔCp_{exp} of -0.26 kcal/mol/K. The inferred enhanced affinity for the second binding of LC8 to IC_{LL} is considerably higher than that of the second light chain binding to IC_{TL}, and corresponds to a 1000-fold ($\Delta\Delta G°$ of -4.0 kcal/mol) enhancement, arising solely from a favorable change in entropy $\Delta(-T\Delta S°)$ of -4.0 kcal/mol in the 20–35 ˚C temperature range (Table 4.1).

Crystal structures of the ternary complexes.

The crystal structure of a fragment of IC bound to Tctex1 and LC8 solved at 3.5 Å resolution shows homodimers of Tctex1 and LC8 binding two chains of IC (residues 109-135) as extended β-strands in the ligand binding grooves (Figure 4.3a): IC residues 110-122 interact directly with Tctex1, IC residues 123-125 link the Tctex1 and LC8 binding sites, and IC residues 126-135 contact LC8. The IC linker adopts an extended polyproline-II (P_{II}) conformation and no direct IC•IC or light chain•light chain interactions occur.

The crystal structure of IC_{LL}•LC8•LC8 solved at 3.15 Å resolution shows a 4:2 stoichiometric complex in which two chains of IC_{LL} (residues 111-135) are brought together by two LC8 dimers with a linker region consisting of five IC_{LL} residues separating the LC8 dimers (Figure 4.3c). The longer exposed linker observed in this structure reflects the shorter IC•LC8 interface relative to the IC•Tctex1 interface in the WT complex. Although there is visible density for IC_{LL} residues within the linker region, there is no density for residues N- or C-terminal to the LC8 recognition sequences. As with the WT IC•Tctex1•LC8 complex, the IC_{LL} linker adopts a P_{II} conformation and has no IC•IC or light chain•light chain contacts.

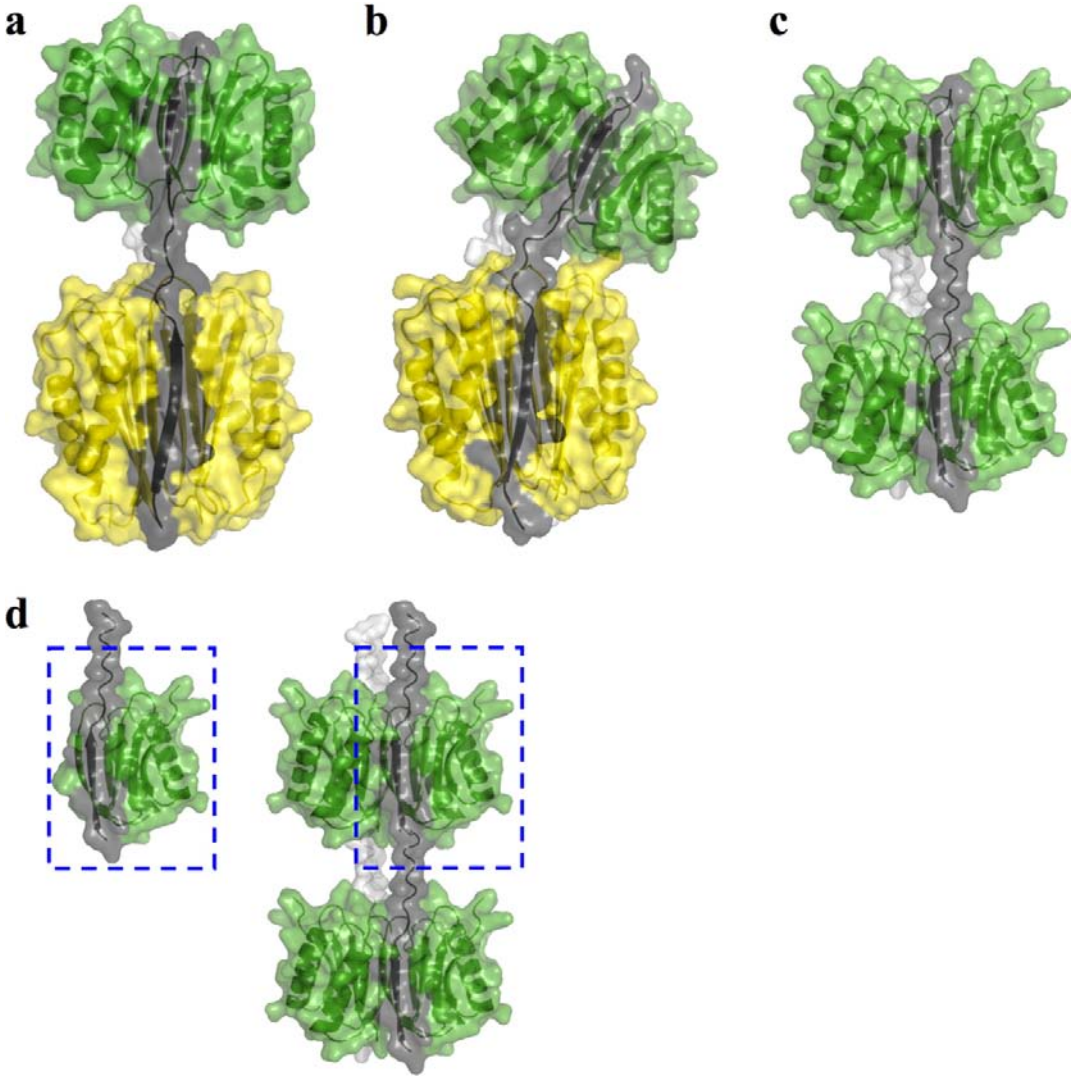

Figure 4.3: Crystal structure of the ternary complexes of IC constructs with light chains. Semi-transparent surface and secondary structural elements are shown for a) the WT IC•Tctex1•LC8 structure reported here (pdb entry 3FM7), b) the IC•Tctex1•LC8 structure previously reported (pdb entry 2PG1) (Williams et al. 2007), and c) the IC_{LL}•LC8•LC8 structure reported here (pdb entry 3GLW). In 2PG1, Tctex1 and LC8 form a small contact surface due to a bend in IC which is not observed in the structures reported here, implying that the IC linker remains flexible in the bound complex. Data collection and refinement statistics are given in Appendix Table A1.2. Figures were generated using Pymol (DeLano 2002).

Discussion

Tctex1 and LC8 have mutually enhanced binding affinities for IC.

Three constructs, IC_{LL} having binding sites for two LC8 subunits, IC_{TL} having binding sites for Tctex1 and LC8, and IC_{L} having a single LC8 binding site, provide a powerful system for quantitatively dissecting bivalency effects in this multicomponent assembly complex. The full thermodynamic cycle for IC_{TL} ternary complex formation is shown in Figure 4.4 along with the corresponding binding steps in IC_{LL} and IC_{L}. The second light chain binds IC_{TL}•Tctex1 or IC_{TL}•LC8 with affinity enhancement of about 50-fold ($\Delta\Delta G°$ of -2.4 kcal/mol). This is consistent with and extends a hydrogen exchange study that indicated enhanced binding of at least 10-fold for the second light chain, i.e. $\Delta\Delta G \leq$ -1.4 kcal/mol (Williams et al. 2007). Interestingly, LC8 binds IC_{LL}•LC8 with affinity enhancement of about 1000-fold ($\Delta\Delta G°$ of -4.0 kcal/mol).

A pure chelate effect in IC_{LL}•LC8 binding.

The 1000-fold affinity enhancement of the second LC8 binding to IC_{LL} agrees well with a 3-order of magnitude enhancement estimated from calculations of the entropic barrier to binding in bivalent small molecules (Murray *et al.* 2002). It is due entirely to a favorable change in the association entropy with a minimal enthalpic change between the first and second binding events ($\Delta\Delta H \approx 0$) (Figure 4.5a). This enhancement is an entropic multivalency effect known in a number of biological systems as the chelate effect (Page *et al.* 1971; Mammen 1998; Breslow 2000; Bertozzi *et al.* 2001). The first LC8 dimer connects two equivalent IC_{LL} chains resulting in a bivalent IC_{LL} duplex that has significantly higher binding affinity for the second LC8 dimer than for the first (Appendix Figure A1.3). The second binding event is of higher affinity because the unfavorable loss of translational and rotational entropy is fully paid in the first binding step, so that the subsequent binding step does not incur this entropic penalty. The enhancement in the IC_{LL}•LC8 system is a remarkable demonstration of the solely entropic origin

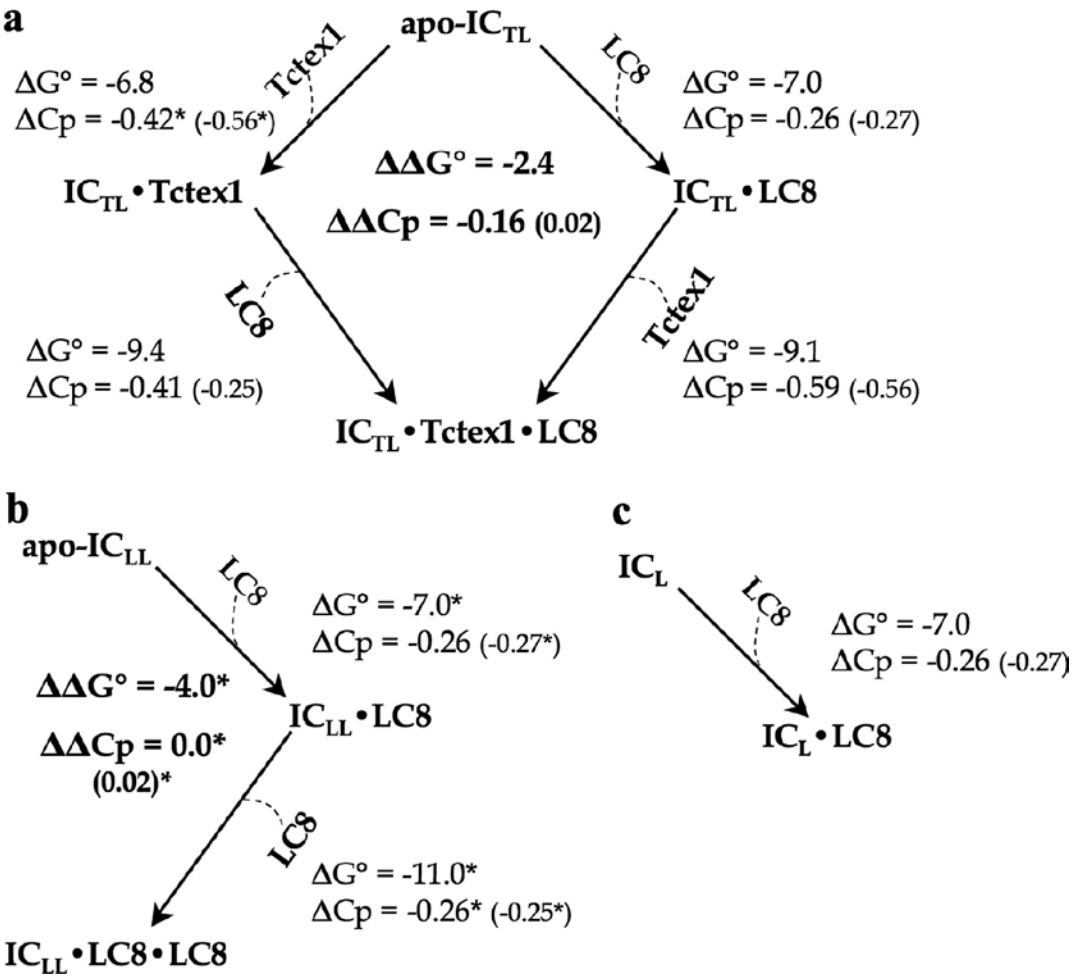

Figure 4.4: Thermodynamic cycle for IC constructs binding to Tctex1 and LC8. Complete thermodynamic parameters on which this figure is based are given in Table 4.1. a) Binding free energies ΔG° (kcal/mol), and experimental ΔCp (kcal/mol/K) for Tctex1 and LC8 binding to IC_{TL}. The computed ΔCp_{calc} are given in parentheses following the experimental ΔCp. The difference in free energy change and heat capacity change between the second and first binding events are expressed as ΔΔG° and ΔΔCp, respectively, and are shown in the center of the cycle. Similar binding parameters are shown for b) LC8 binding to IC_{LL}, which assumes the first IC_{LL}•LC8 binding event has thermodynamic binding parameters equal to the apo-IC_{TL}•LC8 binding event and c) LC8 binding to IC_{L}. All inferred data are labeled by *.

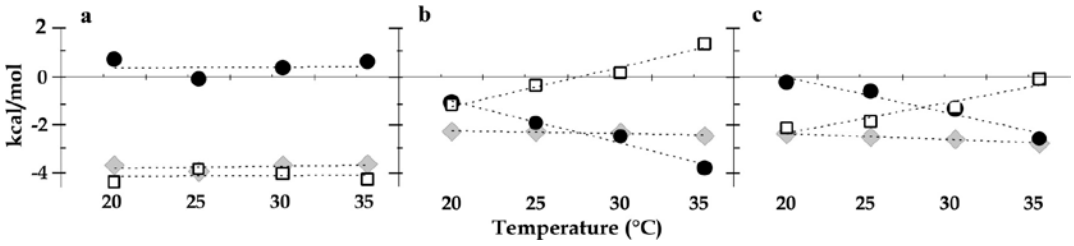

Figure 4.5: Changes in thermodynamic parameters between first and second binding events (ΔΔG°, grey diamonds; ΔΔH°, black circles; and Δ-TΔS°, white squares) for IC ternary complexes. Temperature dependence of the differences in association parameters between a) LC8 with apo-IC_{LL} and LC8 with IC_{LL}•LC8, b) Tctex1 with apo-IC_{TL} and Tctex1 with IC_{TL}•LC8 and c) LC8 with apo-IC_{TL} and LC8 with IC_{TL}•Tctex1.

of the chelate effect in a multisubunit protein assembly. It suggests that the alignment of the two IC arms is optimal for the second LC8 binding.

Deviation from a purely entropic chelate effect in wild-type.

The 50-fold affinity enhancement of LC8 with IC_{TL}•Tctex1 is less than the full chelate enhancement observed for LC8 with IC_{LL}•LC8 and suggests that additional unfavorable interactions occur during the second binding event that offset the full gain from multivalency.

As pointed out by Jencks (Jencks 1981), underestimation of the free energy contribution from the chelate effect is due to destabilizing interactions in a bivalent system that do not occur in the equivalent monovalent systems, since contributions from the chelate effect and the destabilizing interactions are additive. The 2.4 kcal/mol enhancement of binding seen for the IC_{TL} system implies that the full entropic enhancement of 4.0 kcal/mol realized in the IC_{LL} model system is reduced by 1.6 kcal/mol.

The lower enhancement is accompanied by a $\Delta\Delta Cp_{exp}$ of -0.16 kcal/mol/K associated with the second binding (Figure 4.4, 4.5b and c). Since a change in heat capacity is normally associated with burial of nonpolar surface, the implication of the $\Delta\Delta Cp$ value is that the surface area buried in the ternary complex is larger than in the binary complex with either Tctex1 or LC8.

Structural basis for the destabilizing interactions.

To identify the site that undergoes additional structural changes, we compared ΔCp_{exp} for each step in the thermodynamic cycle to ΔCp_{calc} derived from empirical calculations based on surface areas buried in the complexes (Spolar et al. 1994). Crystal structures for IC_{L}•LC8, IC_{TL}•Tctex1•LC8 and IC_{LL}•LC8•LC8 have a similar IC•LC8 interface each yielding a ΔCp_{calc} near -0.26 kcal/mol/K. For Tctex1, the crystal structure of IC_{TL}•Tctex1•LC8 yields a ΔCp_{calc} of -0.56 kcal/mol/K for interactions in the ternary complex, but no crystal

structure is available to guide the calculation for a binary complex of IC_{TL}•Tctex1.

As seen in Figure 4.4, ΔCp_{exp} and ΔCp_{calc} agree very well for apo-IC_{TL} binding LC8, and for IC_{TL}•LC8 binding Tctex1. They are also in good agreement for IC_L with LC8 and apo-IC_{LL} with LC8. The only discrepancies occur on the left side of the IC_{TL} thermodynamic cycle. For apo-IC_{TL} binding Tctex1, ΔCp_{exp} is less negative than the ΔCp_{calc} of -0.56 kcal/mol/K (based on the ternary complex), and for the second step of IC_{TL}•Tctex1 binding LC8, ΔCp_{exp} is more negative than ΔCp_{calc} by a similar difference of 0.16 kcal/mol/K. A simple model explaining these data is that less of IC_{TL} becomes buried when it is in a binary complex with Tctex1 (explaining the less negative ΔCp_{exp} of the first step), and this portion becomes buried during LC8 binding (explaining the more negative ΔCp_{exp} of the second step).

Analysis of the IC_{TL}•Tctex1•LC8 crystal structure suggests that the part of IC not interacting with Tctex1 in the binary complex is the C-terminal end of the recognition site. When LC8 binds IC•Tctex1, the two C-terminal ends of the Tctex1 recognition site would be pulled in closer to the Tctex1 surface, but the N-terminal ends should not be affected. The ΔCp_{calc} values match ΔCp_{exp} if the last four residues of the Tctex1 recognition site (NIPP in *D. melanogaster*) remain solvent exposed in the binary IC_{TL}•Tctex1 complex and then become burried during LC8 binding. Interestingly these last four residues of the Tctex1 recognition site have high sequence conservation (Appendix Table A1.1). We therefore attribute the lower enhancement of LC8 binding to IC_{TL}•Tctex1 versus IC_{LL}•LC8 to additional disorder-to-order transition at the IC_{TL}•Tctex1 interface, with the last four residues of the Tctex1 recognition site acting as an attenuator of the favorable bivalency effects of the system.

Disorder and flexibility in IC complexes.

When natively disordered apo-IC (Benison et al. 2006) binds to dimeric Tctex1 and LC8, the IC recognition sequences form two extended β-strands at the light chain interfaces (Figure 4.3) (Benison et al. 2007; Williams et al. 2007). The linker connecting the interfaces is elongated, but ordered enough to show appreciable electron density in the crystal structure. In WT IC•Tctex1•LC8 and IC_{LL}•LC8•LC8 structures, the IC linker assumes a P_{II} conformation, commonly observed in unfolded peptides (Pappu *et al.* 2002). In a previously reported structure of *Rattus norvegicus* IC peptide bound to *D. melanogaster* Tctex1 and LC8 (Williams et al. 2007), Tctex1 and LC8 contact each other due to a bend in the IC linker (Figure 4.3b). Williams *et al.* noted the contact surface is small and occurs through non-conserved Tctex1 and LC8 residues. In our *D. melanogaster* WT IC•Tctex1•LC8 and IC_{LL}•LC8•LC8 structures no contact is observed (Figure 4.3a, c). Together these results indicate that IC in the linker region of the ternary complex is flexible, and can therefore sample the different orientations observed in both crystal structures of Figure 4.3a and b.

Evolution of adjacent sites.

Tctex1 and LC8 are homologs and have similar IC binding sites in vertebrate IC (e.g. SKVTQV and SKETQT in *Danio rerio*). Both observations raise the prospect that there may have been an ancestral IC that bound either two LC8 dimers or two Tctex1 dimers. Interestingly, adjacent LC8 sites are common in real systems. In guanylate kinase-associated protein (GKAP) (Rodriguez-Crespo et al. 2001) and the nuclear pore protein (Nup159) (Stelter et al. 2007), for example, there are two and six adjacent LC8 recognition sequences, respectively. Since Tctex1 and LC8 bind apo-IC with similar affinities, the evolutionary selection of two distinct light chains is unlikely to be due just to enhanced affinity. Indeed, an enhancement lower than the full multivalent effect suggests affinity has been modulated in the dynein IC assembly to optimize the balance of stability and

reversibility. Consistent with this, contiguous sites for both Tctex1 and LC8 along with the linker separating them are observed in eukaryotes (Appendix Table A1.1).

Poly-bivalency in dynein assembly and regulation.

The emerging picture of dynein IC is one of an elongated, flexible scaffold that contains a number of binding sites for attachment of bivalent dynein light chains (Figure 4.1), dimeric $p150^{Glued}$ subunit of dynactin (King et al. 2003) and various cargo proteins. Bivalency arises because alignment of two IC chains results in a duplex with multiple additional bivalent sites. We refer to this as a poly-bivalent scaffold, which will be created when apo-IC binds *any* of its bivalent ligands, or forms a self-associated coiled-coil (Benison et al. 2006; Williams et al. 2007). Multiple bivalent sites provide the potential for mutual enhancement of affinity for every additional ligand bound, as well as for coiled-coil interchain interactions (Figure 4.1). For any two sites, the extent of binding enhancement depends on the length of the linker between them. A short linker such as that connecting Tctex1 and LC8 will result in higher local effective concentration and higher binding enhancement than a longer linker such as that connecting LC8 and the weakly predicted coiled-coil.

A poly-bivalent system can be quite stable even when the association constant of any single ligand is moderate to weak. Although the assemblage is stable, multivalency, combined with flexibility, provides ready reversibility of ligands, a property very useful for regulation and functional adaptability (Kiessling *et al.* 2006). The resultant dynein N-IC assembly, endowed by multivalency, retains disorder and associated flexibility, which provide versatility and reversibility in response to the local cellular environment.

A poly-bivalent assembled IC can explain the considerably higher binding efficiency of $p150^{Glued}$ to a fragment of IC containing four bivalent sites (the N-terminal predicted coiled-coil, the light chains binding site and the central predicted coiled-coil) relative to a fragment that contains only one bivalent site

(the N-terminal coiled-coil domain) (King et al. 2003). Any of the three additional sites enhances coiled-coil interchain interactions resulting in a tighter binding to $p150^{Glued}$. A similar explanation applies to the more efficient binding to the heavy chain of an IC fragment containing the light chains binding site in addition to the WD repeat C-terminal domain (Ma et al. 1999).

These insights into dynein IC assembly are relevant to other non-dynein proteins that bind LC8. Analysis of these non dynein proteins lead to the hypothesis that LC8 acts as a hub protein that promotes dimerization of its binding partners (Barbar 2008). One such protein, Nup 159 (Stelter et al. 2007), when bound to LC8, is expected to be an aligned and elongated dimer on which one or more additional bivalent binding sites are available (Barbar 2008). We propose that like IC, many of the LC8 binding partners become poly-bivalent scaffolds and that the IC•light chain system is a canonical example of poly-bivalency in the assembly of a new class of intrinsically disordered proteins.

Materials and Methods

Protein preparation.

A synthetic peptide corresponding to IC residues 123-138 was purified as described earlier (Hall et al. 2008). *D. melanogaster* IC_{TL}, Tctex1 and LC8 were prepared as described earlier (Barbar et al. 2001; Makokha et al. 2002; Benison et al. 2006). The IC_{LL} gene was produced by nucleotide synthesis (GeneScript, Piscataway, NJ). Purity was verified by SDS-PAGE and MALDI-TOF mass spectrometry: IC_{LL} M.W. = 7893.1 Da (7897.5 theoretical). Sequence-based calculation of absorptivity at 280 nm was used to measure protein concentrations (Wilkins *et al.* 1999).

Isothermal titration calorimetry.

Proteins were dialyzed in buffer containing 50 mM sodium phosphate, 50 mM sodium chloride, 1 mM sodium azide, pH 7.5. Thermodynamics of binding

were determined at 20, 25, 30 and 35 °C using a VP-ITC calorimeter (MicroCal, Northampton, MA). Data were processed using the manufacturer's supplied software package, Origin 7.0 (OriginLab Corp., Northampton, MA), and fit to a single-site binding model, **A** + **B** → **AB**, where **A** refers to a single IC chain and **B** refers to a single protomer of Tctex1 or LC8. Heat of dilution, estimated to be equal to the enthalpy of the final injection, was subtracted from the binding data prior to fitting. Experiments were conducted with IC in the sample cell, and Tctex1 or LC8 in the syringe. For all experiments the "c value" ($c = [protein]_{sample\ cell} \times K_d^{-1}$) was within the 5 to 500 range required for reliable determination of association constants (Turnbull et al. 2003). Similar experiments were conducted with IC_{TL} saturated with a five-fold excess of either Tctex1 or LC8. Cell and syringe concentrations of 0.07 and 0.8 or 0.025 and 0.4 mM were used for apo- or pre-bound IC_{TL}, respectively. Cell and syringe concentration of 0.07 and 1.35 mM were used for IC_{LL}. Average values are reported with error estimation as the difference between a minimum of two repeats for each temperature.

Changes in heat capacity at constant pressure (ΔCp_{exp}) were determined from the change in enthalpy ($\Delta H°$) as a function of temperature. All ΔCp_{exp} values were obtained with linear correlation coefficients of > 0.98. Calculated changes in heat capacity (ΔCp_{calc}) were computed as described by Spolar and Record (Spolar et al. 1994). Changes in solvent accessible surface area were determined using SURFACE RACER 5.0 (Tsodikov *et al.* 2002). Protein Data Bank structures 2P2T (Benison et al. 2007), 3FM7 (Tctex1 site only), 3FM7 (LC8 site only) and 3GLW were used to model apo-IC_{TL}•LC8, pre-bound IC_{TL}•Tctex1, pre-bound IC_{TL}•LC8 and IC_{LL}•LC8 complexes, respectively.

Size exclusion chromatography and multi-angle light scattering.

Association states were determined from analytical size-exclusion chromatography (Superdex75) with an online multi-angle light scattering detector (miniDawn, Wyatt Technology) in 200 mM sodium sulfate, 50 mM sodium

phosphate, pH 7.3. Data were processed using ASTRA v5.1.9.1 (Wyatt Technology). The molecular mass of apo-IC_{TL} and the IC_{TL}•Tctex1•LC8 complex were 7.7 and 68.7 kDa, respectively, in good agreement with the theoretical molecular mass for a monomer (7.8 kDa) and a dimer of heterotrimers (67.3 kDa), respectively.

X-ray crystallography.

An IC construct (corresponding to residues 92 to 260) bound to Tctex1 and LC8 (WT IC•Tctex1•LC8) and IC_{LL}•LC8•LC8 complex were in buffer containing 15 mM sodium chloride, 5 mM Tris, pH 7.5 and a final protein complex concentration of 0.2 mM. Crystals were obtained at 4 °C using hanging drops setup with a 1µl protein and reservoir solution equilibrated against a 400 µl reservoir.

For WT IC•Tctex1•LC8, hexagonal pyramidal crystals were obtained using a reservoir of 16% PEG 8000, 100 mM sodium cacodylate, 200 mM calcium acetate, pH 6.5. Crystals grew to a final size of 0.16 x 0.16 x 0.3 mm^3. For IC_{LL}•LC8•LC8, blade shaped crystals were obtained using 30% PEG 400, 100 mM Hepes, 200 mM magnesium chloride, pH 7.5. Crystals grew to a final size of 0.15 x 0.15 x 0.5 mm^3 (Appendix Table A1.2). Crystals for both complexes were analyzed by SDS-PAGE after data collection and showed the full length IC constructs were proteolyzed. Therefore both complexes contain an IC domain of unknown length N- and C-terminal to the Tctex1 and LC8 binding sites. IC is natively disordered and sensitive to protease degradation, it seems likely that formation of the crystal lattice occurred opportunistically during *in situ* proteolysis (Dong *et al.* 2007), and future attempts at reproducing these crystals may be aided by the addition of protease to the protein solution.

Crystals were pulled through oil before flash-freezing in loops using liquid nitrogen. For WT IC•Tctex1•LC8, 3.5 Å resolution oscillation data ($\Delta\varphi = 1.0°$) were collected at the Berkeley Advanced Light Source, HHMI beam line 8.2.2.

For IC_{LL}•LC8•LC8, 3.15 Å resolution oscillation data were collected using an in-house Raxis IV system with CuKα-radiation. Data were integrated using Imosflm (Leslie 1992) and scaled using SCALA (Diederichs *et al.* 1997). The WT IC•Tctex1•LC8 and IC_{LL}•LC8•LC8 space groups were $P6_2$ with unit cell of a=b=115.66, c=90.37 Å and $P6_122$ with a=b=44.65, c= 219.38, respectively. Phases were determined for both crystals by molecular replacement using PHASER (McCoy 2007) and 2PG1 and 3BRI as search models.

The WT IC•Tctex1•LC8 crystal had a full IC•Tctex1•LC8 complex (six protein chains) in the asymmetric unit. Molecular replacement placed a dimer of Tctex1 and a dimer of LC8 allowing an electron density map to be calculated that showed density for the IC peptides. IC residues were manually added using Coot (Emsley *et al.* 2004) and the complex was refined using REFMAC (Murshudov *et al.* 1997). The IC_{LL}•LC8•LC8 crystal had just one-fourth of the IC_{LL}•LC8•LC8 complex (one LC8 chain and one half of an IC_{LL} chain) in the asymmetric unit. Molecular replacement placed a protomer of LC8 in the cell and the resulting electron density map revealed density for the portion of IC interacting with LC8 and weaker density for the five residue IC linker connecting LC8 protomers in adjacent unit cells. The five IC linker residues, modeled in an extended P_{II} conformation, fit well in the distance between the LC8 dimers and improved R_{free}. The linker IC residues were modeled at half occupancy because only half of the unit cells should contain these residues (Figure 4.3d, e).

For both structures one domain per chain was used for TLS refinement. Crystallographic data collection and refinement statistics are summarized in Appendix Table A1.2.

Accession Codes.

The atomic coordinates and structure factors for WT IC•Tctex1•LC8 and IC_{LL}•LC8•LC8 have been deposited into the Protein Data Bank with accession numbers 3FM7 and 3GLW.

Acknowledgements

The authors thank Andrea Hall and Dale Tronrud for assistance with X-ray data collection and processing, Yujuan Song for assistance with IC_{LL} gene manipulation and Clare Woodward, Michael Hare, and members of the Barbar lab for valuable discussion. We acknowledge the support of the nucleic acid and protein core and the mass spectrometry facilities and services core in the OSU Environmental Health Sciences Center (NIH/NIEHS 00210) as well as HHMI beam line 8.2.2 of the Advanced Light Source synchrotron.

Chapter 5

The crystal structure of dynein intermediate chainlight chain roadblock complex gives new insights into dynein assembly

Justin Hall, Yujuan Song, P. Andrew Karplus and Elisar Barbar

Published in *Journal of Biological Chemistry*,
In press

Summary

The roadblock/LC7 dynein light chain is a ubiquitous component of all dyneins and is essential for many diverse processes including proper axonal transport and dendrite growth. In addition, LC7 functions in non-dynein transcriptional activation of the transforming growth factor-β complex. Crystal structures of *Drosophila melanogaster* LC7 in the apo form and in complex with a segment of the disordered N-terminal domain of dynein intermediate chain (IC)[4] provide the first definitive identification of the IC sequence recognized by LC7. The site, confirmed by isothermal titration calorimetry studies, overlaps the IC sequence considered in the literature to be an IC self-association domain. The IC peptide binds as two amphipathic helices that lie along an extensive hydrophobic cleft on LC7 and ends with a polar side chain interaction network that includes conserved residues from both proteins. The LC7 recognition sequence on IC and its interface with LC7 are well conserved and thus likely representative of all IC•LC7 structures. Interestingly, the position of bound IC in the IC•LC7 complex mimics a helix that is integrated into the primary structure in distantly related LC7 homologs. The IC•LC7 structure further shows that the naturally occurring *robl*^{Z} deletion mutation contains the majority of the IC binding site, and suggests that promotion of IC binding by phosphorylation of LC7 is an indirect effect.

Introduction

[4]The abbreviations used are: IC, the 74-kDa dynein intermediate chain corresponding to gene *Cdic2b*; N-IC, IC residues 1-289; $IC_{TL\text{-}d7}$, IC residues 92-237; IC_{TL7}, IC residues 92-260; IC_{7}, IC residues 212-260; $IC_{92\text{-}289}$, IC residues 92-289; Tctex1, the 12-kDa dynein light chain corresponding to gene *Dlc90F*; LC8, the 10-kDa dynein light chain corresponding to gene *Cdlc2*; LC7, the 11-kDa dynein light chain corresponding to gene *robl*; *robl*^{Z}, truncation mutant of *D. melanogaster* LC7; PDB, Protein Data Bank; TGF-β, the transforming growth factor-β receptor complex; Mgl, homodimeric gliding protein MglB from *Thermus thermophilus* pdb accession code 1J3W; MP1•p14, mitogen-activated protein kinase interacting heterodimer pdb accession code 1SKO; ITC, isothermal titration calorimetry..

Cytoplasmic dyneins are large multi-subunit protein complexes that are responsible for ATP-driven minus-end directed transport of diverse cargo along microtubules. They play fundamental roles within the cell including mitotic spindle assembly and orientation (Echeverri et al. 1996), chromosome segregation (Compton 2000), and intracellular trafficking of vesicles and mRNA (Mische et al. 2007). Dyneins are essential for the development and maintenance of neurons (Stokin *et al.* 2006), and for this reason dynein dysfunction is associated with several human diseases, such as lissencephaly (Faulkner et al. 2000), neural degeneration (Hafezparast et al. 2003), and male infertility (Zuccarello et al. 2008).

Dynein heavy chains are responsible for motor activity while intermediate chain (IC) and light chain subunits comprise the cargo attachment complex. The N- and C-terminal domains of IC are structurally and functionally independent. The primarily disordered N-terminal domain (N-IC) is central to dynein assembly, regulation and cargo binding as it contains a self-association domain and the binding sites for the three light chains, the $p150^{Glued}$ subunit of dynactin, and several putative cargoes (King et al. 2000; Ye et al. 2000; Ligon et al. 2001; Kardon et al. 2009). Dynein light chains Tctex1, LC8, and LC7 are all integral components of both cytoplasmic and axonemal dyneins (Wickstead et al. 2007) which bind distinct regions of N-IC (Susalka et al. 2000; Makokha et al. 2002) (Figure 5.1). Tctex1 and LC8 are dimeric structural homologs and each binds two chains of IC at its dimer interface (Benison et al. 2007; Williams et al. 2007; Hall et al. 2009). Tctex1 and LC8 show mutually enhanced affinity, as one protein binds two IC chains to form a bivalent IC that has higher affinity for the other light chain (Hall et al. 2009). We recently proposed that Tctex1 and LC8 work together to create a poly-bivalent IC duplex that serves as a stable and versatile scaffold providing tighter IC self-association and higher affinity for multiple bivalent binding partners (Hall et al. 2009). LC7 is less well understood than the others, and this study is focused on the IC•LC7 interaction.

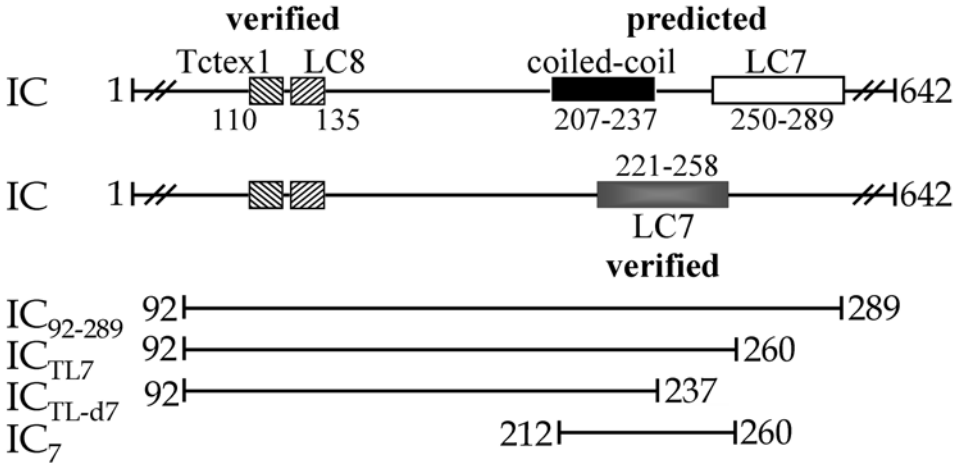

Figure 5.1: IC light chain binding regions and constructs used in this study. The upper IC diagram locates the verified binding sites for Tctex1 and for LC8 (hatched) along with a proposed IC self-association domain (black) and the proposed binding site for LC7 (open). The second diagram updates the model to include the LC7 recognition sequence identified in this study (grey). IC recognition sequences for Tctex1 and LC8 are, respectively, residues 110-122 and 126-135 (Benison et al. 2007; Williams et al. 2007; Hall et al. 2009). The four additional lines define the residue ranges of the IC constructs used in this study. Numbering is relative to amino acids from the *D. melanogaster Cdic*2b gene, subscripts **T**, **L**, **7** and **-d7** stand for **T**ctex1, **L**C8, LC**7** and **d**isrupted LC**7** recognition sequences**,** respectively.

LC7, also called roadblock (Robl) or km23, is a ubiquitous component of cytoplasmic dyneins. The roadblock name originates from knockout mutants in *D. melanogaster* that result in posterior sluggish motility leading to complete paralysis. LC7-null mutants in *D. melanogaster* have mitotic defects and display phenotypes with defective axonal transport, neuronal blast cell division and dendrite growth (Reuter *et al.* 2003). LC7-null mutants result in flagellar assembly and motility defects in *Chlamydomonas reinhardtii* (Pazour *et al.* 2000), and disrupted dynein-mediated nuclear distribution in *Aspergillus nidulans* (Zhang *et al.* 2009).

NMR and X-ray crystal structures of apo-LC7 from *Homo sapiens* and *Rattus norvegicus* (Ilangovan et al. 2005; Song et al. 2005; Liu et al. 2006) show LC7 is a homodimer structurally unrelated to Tctex1 and LC8. LC7 belongs to an ancient protein superfamily that is widely represented in archaea and bacteria and is implicated in regulation of NTPase activity (Koonin et al. 2000). Superfamily members share a common structural fold of five β-strands and three α-helices, except the C-terminal α-helix is missing in LC7. LC7 apparently has multiple non-dynein interaction partners including the Rab6 family of GTPase regulators (Wanschers et al. 2008), the human reduced folate carrier (Ashokkumar et al. 2009) and the transforming growth factor-β (TGF-β) receptor complex (Tang et al. 2002; Jin et al. 2009), but in no case is the molecular-level interaction with a binding partner characterized. The TGF-β complex is central to signaling networks controlling growth, differentiation, extracellular matrix production, apoptosis and oncogenesis. Consistent with a role for LC7 in multiple cellular pathways, mutations of LC7 (Ding et al. 2005) or changes in LC7 isoform expression levels (Jiang et al. 2001) have been observed in ovarian and hepatic cancers.

Phosphorylation is one mechanism that appears to regulate the multiple roles of LC7. LC7 is serine phosphorylated following TGF-β receptor activation and binds IC in response to this activation. Two phosphorylation site mutants disrupt the interaction with IC (Ding et al. 2005) leading to the conclusion that

phosphorylation of LC7 is necessary for IC binding. However, at present there is no clear molecular-level picture of processes associated with LC7 phosphorylation/dephosphorylation or of its involvement in IC binding.

As part of our ongoing effort to elucidate structure-function relationships of dynein light chains, and build a comprehensive understanding of dynein assembly, we report here the first molecular-level structure of an IC•LC7 complex from *D. melanogaster* (79% sequence identity to *H. sapiens* LC7). The IC•LC7 complex structure reveals unexpected insights into dynein assembly and regulation. It also provides interesting evolutionary perspectives. Comparing LC7 to its likely ancestral fold suggests that the multi-functionality of LC7 is the result of its recruitment for new dynein-related function even while ancient functions are maintained.

Results

Crystal structure of apo-LC7.

The apo-LC7 crystal structure was solved to 1.95 Å with two LC7 homodimers in the asymmetric unit, each dimer with the expected LC7 fold seen for *H. sapiens* and *R. norvegicus* apo-LC7 (Ilangovan et al. 2005; Song et al. 2005; Liu et al. 2006): a pair of alpha helices (α_1, α_1') flanking a continuous antiparallel 10-stranded β-sheet (strand order β_2-β_1-β_5-β_4-β_3•$\beta_{3'}$-$\beta_{4'}$-$\beta_{5'}$-$\beta_{1'}$-$\beta_{2'}$) on one face and a 2-helix bundle (α_2•$\alpha_{2'}$) on the opposite face (Figure 5.2a). The four LC7 chains in the asymmetric unit have somewhat different N-terminal electron density, with chain B being the best defined (starting residues are Leu9 for chain A, Met1 for chain B and Val5 for chains C and D). In contrast, the C-terminal density of each chain is equivalent, ending at Asn94 with residues 95-97 too disordered to model. Conformational differences among the four chains are observed for helix α_1 and the loops connecting strands β_1 to β_2 (L_2) and β_4 to β_5 (L_6) (Figure 5.2c). The differences in α_1 among the four chains are due to variations in the angle of the

Figure 5.2: Structures of apo-LC7 and the IC•LC7 complex. a) Two orthogonal views are shown of the LC7 homodimer. Chains B (steel blue) and D (grey) are shown with secondary structural elements labeled for chain B. b) The same two views of the IC•LC7 complex with chains of IC in orange and light orange, and IC α-helix 1 (α_{IC1}, residues 223-230) and 2 (α_{IC2}, residues 233-254) labeled. c) Stereoview of an overlay of the four independent apo-LC7 chains (semi-transparent bright blue) onto one LC7 chain from the IC•LC7 complex as colored in panel "b". Regions moving upon IC binding occur in α-helix 1 (α_1), Loop 2 (L_2) and Loop 6 (L_6). d) Stereoview of the IC•LC7 interface. Side chains for hydrophobic residues burying greater than 5 $Å^2$, and the residues of the fingerprint region are shown. G243 Cα position is indicated.

Figure 5.2: (*Continued*).

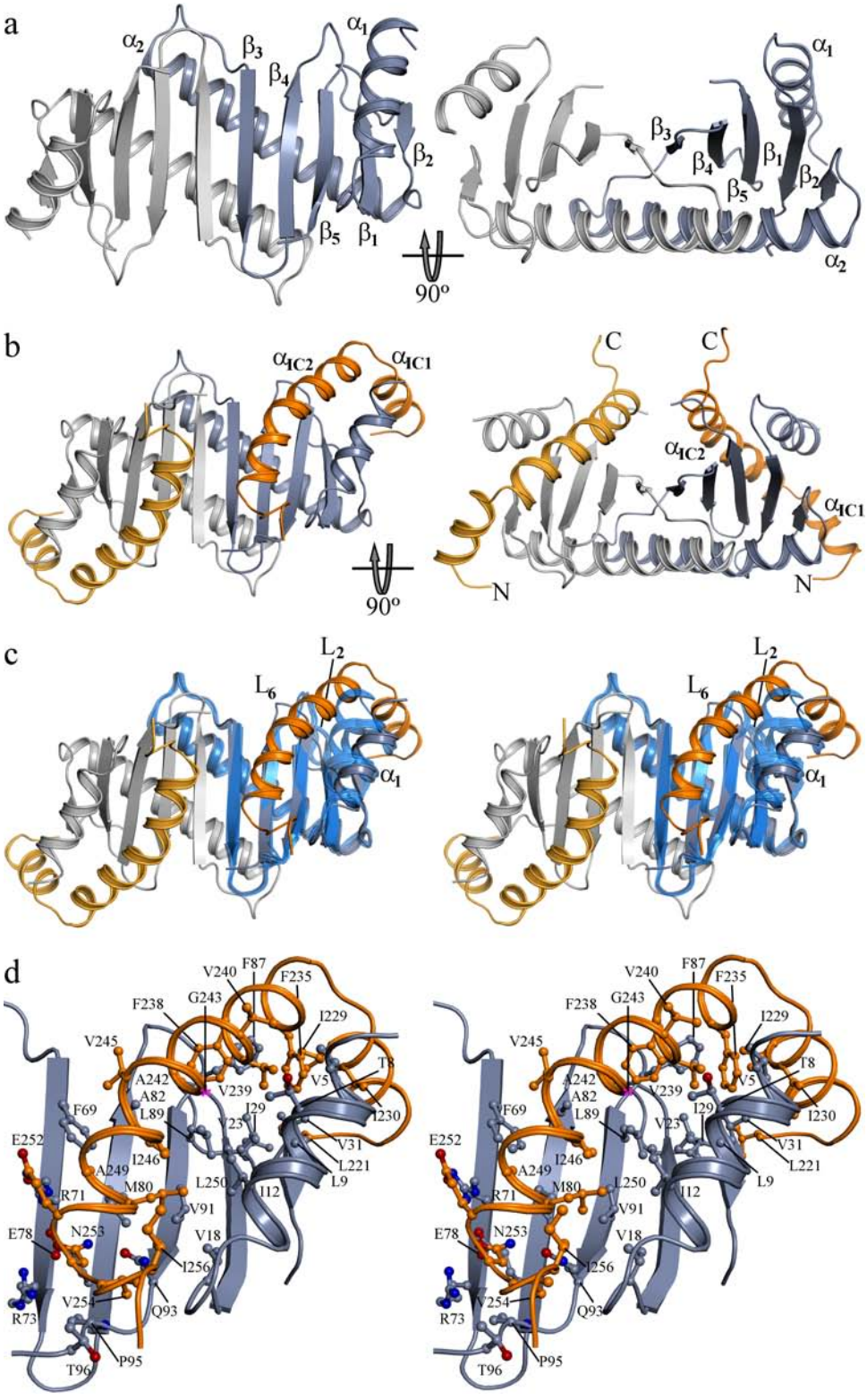

loop connecting α_1 to β_1 (L_1), with α_1 acting as a rigid rod to amplify differences N-terminal to L_1. These differences appear related to crystal packing near L_1.

Interestingly, conformational variations among the four chains in the asymmetric unit recapitulate differences between previously reported structures of apo-LC7, with chain B similar to the average conformation in NMR structures (Ilangovan et al. 2005; Song et al. 2005) and the orientation of α_1 in chain A similar to α_1 in the 2.1 Å *H. sapiens* LC7 crystal structure (Liu et al. 2006). The latter also shows the first five residues and loop L_6 are too disordered to fully model.

Crystal structure of the IC•LC7 complex.

$IC_{92\text{-}289}$ bound to LC7 fortuitously crystallized in the presence of protease added to aid crystal formation (Dong et al. 2007). Using these crystals, the IC•LC7 complex was solved at a nominal resolution of 3.0 Å with the asymmetric unit containing two LC7 homodimers binding two IC chains per dimer. Each chain of IC and LC7 in the asymmetric unit has similar electron density, with IC chains initially observed as helical density not accounted for by LC7. Data interpretation at 3 Å is challenging, so the N-to-C directionality of IC segments was determined by modeling a poly-Ala chain in both directions, with one orientation clearly fitting better to the unbiased electron density. The unique sequence and registry of IC was determined from the pattern of side chain densities, including buried Leu, Ile and Phe residues at the IC•LC7 interface. This ultimately guided the modeling of residues Leu221 through Thr258 for each IC chain and Gln3 through Asp97 for each LC7 chain. A set of unbiased electron density maps provide strong support for the final interpretation (Figure 5.3 and Appendix Figure A2.1). Based on this interpretation, the IC_7 construct, encompassing IC residues 212-260 (Figure 5.1) was designed for use in subsequent studies. As a further verification that the IC segment bound in the IC•LC7 crystals was correctly identified, IC•LC7 crystallization conditions (without *in situ* proteolysis) produce isomorphous

Figure 5.3: Unbiased electron density evidence for the IC•LC7 complex. a) Fo-Fc electron density showing the IC presence in the IC•LC7 complex after molecular replacement with an LC7 model (steel blue). A Cα trace of the final IC model (with 4 residues labeled) and some side chains of LC7 are included for reference. Side chains for residues R71, R73, E78 and Q93 (cyan) are omitted. Density is contoured at 3σ (green) and -3σ (magenta). b) 2Fo-Fc and Fo-Fc maps calculated after inclusion in the refinement of a 19 residue poly-Ala helix (carbon, oxygen and nitrogen atoms are colored orange, red and blue, respectively) modeled into the strong helical density seen in panel "a" with an N-to-C directionality parallel to α_1 of LC7. 2Fo-Fc density is contoured at 2σ (blue), and Fo-Fc density is contoured as in panel "a". Labels are based on the final interpreted model. c) 2Fo-Fc and Fo-Fc density for LC7 side chains R71, R73, E78, Q93 (grey/steel blue) and IC side chains E252 and N253 (light orange/orange) after refinement of a model with the complete IC•LC7 complex except these side chains. Potential hydrogen bonding side chains are connected by dashed lines with the hydrogen bond from E252 drawn halfway between ηN1 and ηN2 of R71 to reflect uncertainty in side chain position in this analysis. 2Fo-Fc density is contoured at 1σ (blue), and Fo-Fc density is contoured as in panel "a".

Figure 5.3: (*Continued*).

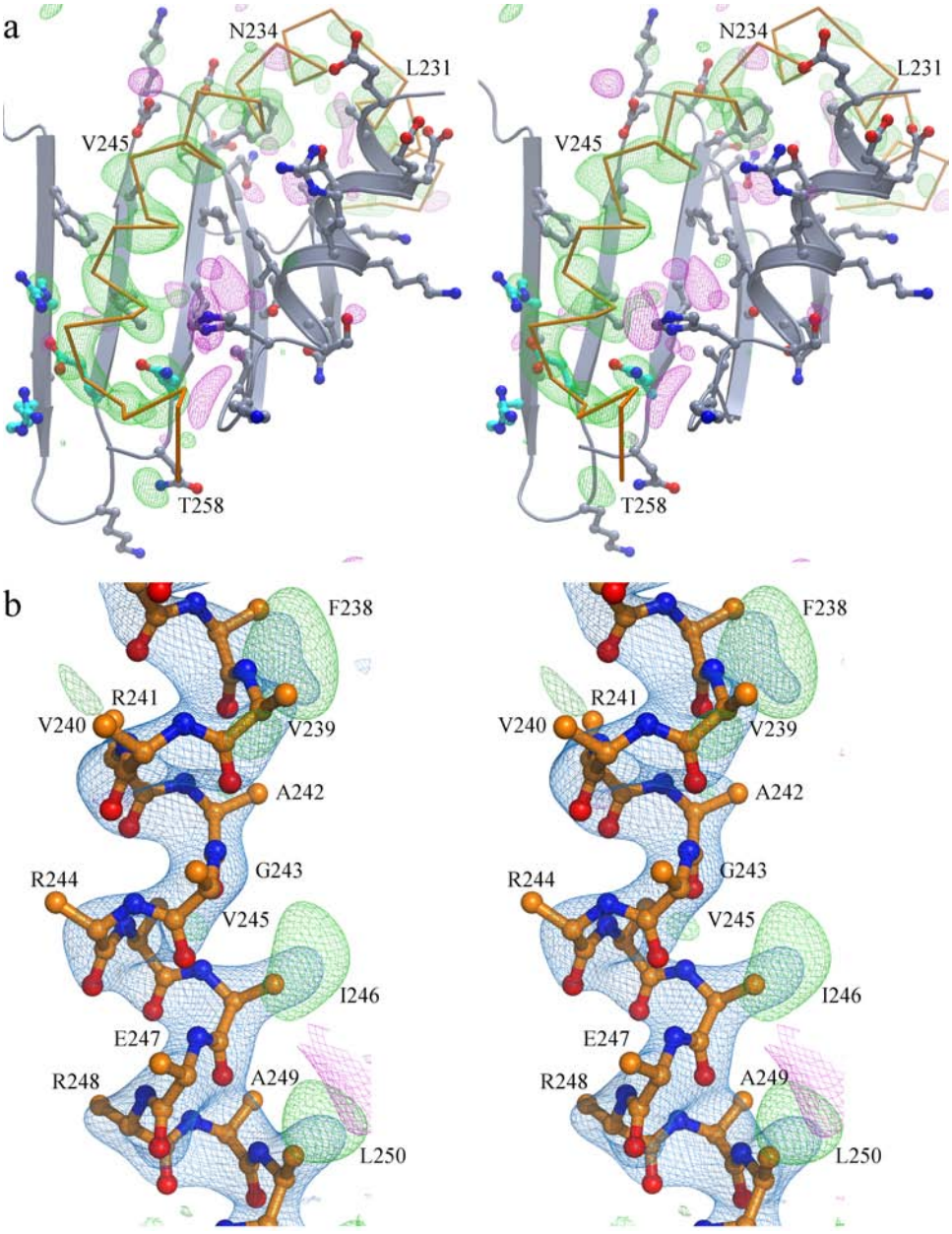

Figure 5.3: (*Continued*).

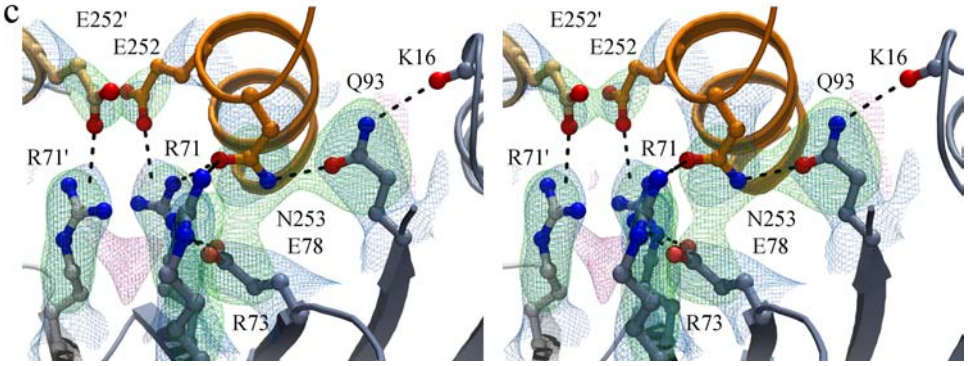

crystals of the IC_7•LC7 complex. The IC_7•LC7 crystals grew within four days and a low resolution data set shows helical density for IC_7 bound to LC7. These crystals diffract similarly to the original IC•LC7 crystals produced from *in situ* proteolysis and thus were not analyzed further.

The final IC•LC7 model shows IC binds LC7 as two amphipathic helices separated by a turn, with IC chains entering and exiting parallel to the LC7 two-fold symmetry axis (Figure 5.2b). The first IC α-helix (α_{IC1}, residues 223-230) packs against β_4 and L_2 of LC7, the turn (residues 231-232) caps α_1 of LC7, and the second α-helix (α_{IC2}, residues 233-254) packs against α_1, β_4, β_5, L_1 and L_6 of LC7. α_{IC1} has weaker electron density (and higher B-factors) than α_{IC2}. α_{IC1} and α_{IC2} have two and five complete helical turns, respectively, with α_{IC2} having a bend after the third helical turn. IC residues 255-258 have a non-regular extended conformation, and interact with residues from L_1 and the C-terminus of LC7 (Figure 5.2b).

The IC•LC7 binding surface is large, comprising 22 IC residues and 27 LC7 residues and accounting for close to 2400 $Å^2$ of surface, of which nearly 75% (≈1800 $Å^2$) is nonpolar (Figure 5.2d, Appendix Figure A2.2, Appendix Table A2.1). Multiple packing interactions are formed by each of the highly conserved residues Phe235, Phe238, Ile246 and Leu250 of IC and Val5, Val31, Phe69, Phe87 and Leu89 of LC7. The C-terminal end of α_{IC2} contains a network of buried inter and intrachain hydrogen bonding and salt bridge interactions which may constitute a specificity-determining fingerprint for IC•LC7 recognition.

The fingerprint region contains well-conserved polar residues including Glu252 and Asn253 of IC and Lys16, Arg71, Arg73, Glu78 and Gln93 of LC7. While side chains in a 3 Å structure are sometimes poorly defined, the residues of the fingerprint region that are largely buried at the IC•LC7 interface have well-defined side chain densities (Figure 5.3c). Glu252 and Arg73 are partially solvent exposed and have the weakest side chain densities, while Arg71 is almost completely buried and has very strong side chain density (Appendix Table A2.1).

Arg71 stacks against Arg71' while interacting with Glu252 and Glu252' at the LC7 two-fold axis (Figure 5.3c) (Soetens 1997; Persson *et al.* 2009). A polar interaction network bridges the Asn253 side chain, Arg71 guanidino group, Gln93 side chain, and the Lys16 backbone (Figure 5.3c).

Whereas α_1, L_2 and L_6 are the most structurally variable regions of apo-LC7 (Figure 5.2c), the four LC7 chains in the asymmetric unit of the IC•LC7 complex have consistent positions and strong electron density for these segments despite the lower resolution of the IC•LC7 complex. Interestingly, the α_1 position in chain A of apo-LC7 is close to that of α_1 in the IC•LC7 complex and also contains a hydrogen bond between Nε of Gln93 and the carbonyl oxygen of Lys16; conversely, the α_1 position in chain B (which also matches the NMR solution structure) undergoes a 7 Å shift in the position of α_1. All four chains have consistent shifts of 2.5 Å for L_2 and 4 Å for L_6 (Figure 5.2c).

Thermodynamics of IC•LC7 complex formation.

Isothermal titration calorimetry (ITC) was used to further confirm the newly determined LC7 recognition sequence and to establish the thermodynamic parameters governing IC•LC7 association (Figure 5.4a, b, Table 5.1). IC constructs used are given in Figure 5.1. The designed IC_7 peptide, containing the crystallographically determined recognition residues 221-258, binds LC7 with moderate affinity of K_d = 5.7 μM. For comparison, LC7 binds to the more physiologically relevant IC_{TL7}•Tctex1•LC8 complex with similar K_d = 2.0 μM. For both complexes, $\Delta G°$, $\Delta H°$ and $-T\Delta S°$ values are quite similar, consistent with the IC_7 segment containing all of the LC7 interactions important in the larger IC_{TL7} construct (Table 5.1). Data for IC_7•LC7 binding show slight deviations from a theoretical best fit for a single-site binding model; however, this is not true for LC7 binding to the IC_{TL7}•Tctex1•LC8 complex. A small (< 3-fold) apparent affinity enhancement is seen for LC7 binding to the IC_{TL7}•Tctex1•LC8 complex relative to IC_7. For further confirmation of the LC7 recognition sequence, we

Figure 5.4: Representative ITC and gel filtration data for LC7 binding to IC at 25 °C. ITC data with thermograms (top panels) and isotherms (bottom panels) for LC7 binding to a) IC_7 and b) IC_{TL7} (pre-bound by a four-fold excess of Tctex1 and LC8). Solid lines correspond to the non-linear least squares fit. c) Sizing gel (Superdex200, 10/300) elution profile for samples of the IC_{TL7}•Tctex1•LC8•LC7 complex produced in ITC experiments (from panel "b") give a single peak for the complex along with peaks for excess Tctex1, LC8 and LC7, dotted lines indicate MALS determined mass for each peak. LC8 and LC7 are not resolved, separate injections of apo-IC_{TL7}, LC8 and LC7 were used to determine individual masses and verify co-elution of LC8 and LC7 (data not shown). The void volume for this column is 10 ml. d) SDS-PAGE analysis of the eluted IC_{TL7}•Tctex1•LC8•LC7 complex (from panel "c"). The quaternary complex (lane 2 from the left) has bands of approximately equal staining density and mobility matching free IC_{TL7} (lane 3), Tctex1 (lane 4), LC7 (lane 5) and LC8 (lane 6).

Figure 5.4: (*Continued*).

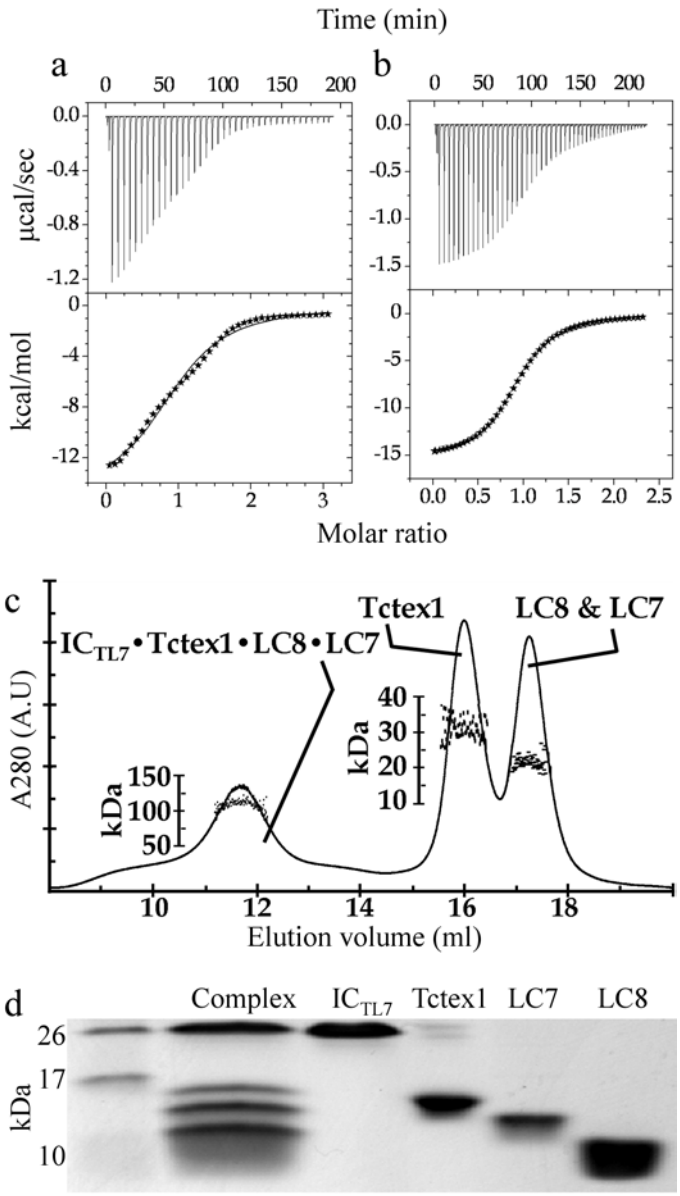

Table 5.1: Thermodynamic parameters for LC7 binding to IC constructs at 25 °C[a].

Cell	Syringe	K_d (μM)	ΔG° (kcal/mol)	ΔH° (kcal/mol)	-TΔS° (kcal/mol)
IC_7	LC7	5.7 ±0.5	-7.2 ±0.1	-15.0 ±0.3	7.8 ±0.3
IC_{TL7}•Tctex1•LC8	LC7	2.0 ±0.1	-7.8 ±0.1	-14.8 ±0.5	7.1 ±0.7

[a]Values are the average plus or minus the standard deviation of three (IC_7) and two (IC_{TL7}) experiments.

determined if LC7 binds IC with a disrupted recognition sequence ($IC_{TL\text{-}d7}$); the absence of detectable binding (data not shown), implies that residues 238-260 are important for binding.

Analytical gel filtration chromatography coupled to multi-angle light scattering (MALS) gave molecular masses of 20.9 and 112.2 kDa, for a monomeric apo-IC_{TL7} and a 2:2:2:2 complex of IC_{TL7}•Tctex1•LC8•LC7 (Figure 5.4c), in good agreement with the 20.5 and 110.6 kDa theoretical masses. SDS-PAGE analysis of the peak corresponding to the quaternary complex shows IC_{TL7}, Tctex1, LC8, and LC7 are present at comparable concentrations (Figure 5.4d). The association state of IC_7 was confirmed to be monomeric as it migrates slower than a similar sized IC construct which is monomeric and disordered (Benison et al. 2006; Hall et al. 2009) (Appendix Figure A2.3).

Discussion

Essential residues for IC•LC7 binding.

Residues in the IC•LC7 interface are well conserved among species (Figure 5.5a, Appendix Figure A2.4), suggesting universality of this interaction mode among *D. melanogaster* and vertebrate dyneins. Two conserved patterns are notable: the first is helix α_{IC2}, which is amphipathic in all IC sequences, and packs into the hydrophobic cleft created by α_1, β_4 and β_5 of LC7. The second is electrostatic interactions between Asn253 of IC with Arg73 and Gln93 of LC7 and between Glu252 and Glu252' from the two IC chains with Arg71 and Arg71' of LC7 (Figure 5.3c). In apo-LC7, Arg73 and Glu78 form an intrachain salt bridge, but Arg71 and Arg71' do not stack (Soetens 1997; Persson et al. 2009). The electrostatic interaction network formed in the complex may explain why IC constructs ending at residue 250 (Susalka et al. 2002; Song et al. 2005; Lo *et al.* 2006) and 237 (this work) do not bind LC7 even though they contain most of the hydrophobic packing interactions. Consistent with a substantial electrostatic interaction, IC•LC7 binding is abolished in 1 M NaCl (Susalka et al. 2002). These

Figure 5.5: Location of residues impacted in the *robl*^{Z} mutant, differences between human LC7 isoforms and phosphorylation sites. a) Sequences of LC7 from *D. melanogaster* (*Dm*), the *robl*^{Z} mutant of *D. melanogaster* (*robl*^{Z}) and *H. sapiens* LC7a and LC7b isoforms (*Hsa* and *Hsb*, respectively). Indicated also are the LC7 secondary structure (above), residues with more than 5 Å^{2} of surface buried by IC (orange bars), *Dm* LC7 residues differing from *Hsa* and *Hsb* LC7 (cyan background), potential phosphorylation sites (Ding et al. 2005) (red background) and conserved sequence differences between *Hsa* and *Hsb* (yellow background) (see Appendix Figure A2.4 for complete sequence comparison of LC7 isoforms in vertebrates). Ser33 (Ding et al. 2005) and Ser38 (Blom *et al.* 1999) are both potential phosphorylation sites and conserved sequence difference. The twelve residue insertion of *robl*^{Z} is shown in lowercase letters. b) Surface representation of LC7 (white) with IC bound (light orange/orange) showing residues with more than 5 Å^{2} surface buried by IC divided into those that are retained in *robl*^{Z} (dark blue), not retained in *robl*^{Z} (bright blue) and those that may be functionally substituted by the twelve residue insertion of *robl*^{Z} (violet). The *robl*^{Z} mutant of LC7 results in the loss of residues essential for the LC7 homodimer, but leaves at least 70% of the IC•LC7 interface (dark blue). c) Potential phosphorylation sites of LC7 (red) and conserved sequence differences between LC7 isoforms (yellow). Solvent accessible surface area calculations were determined using SURFACE RACER 5.0 (Tsodikov et al. 2002), figures generated using Pymol (DeLano 2002).

Figure 5.5: (*Continued*).

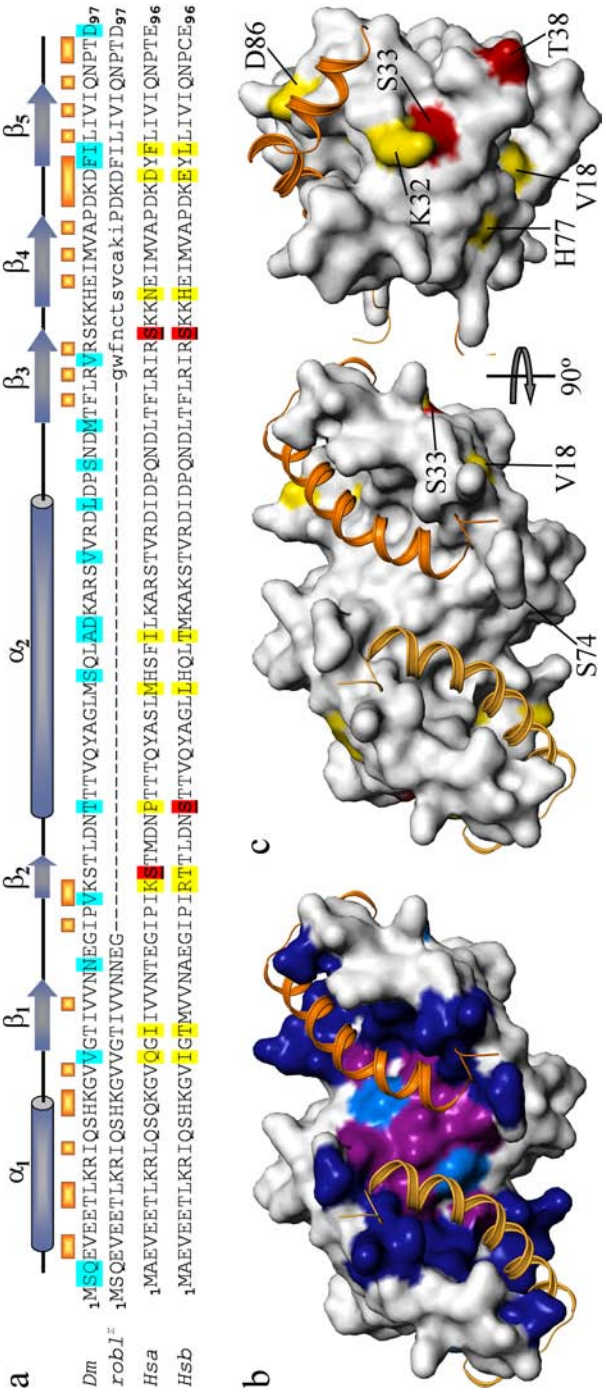

data support the conclusion that the specific interactions between Glu252 and Asn253 of IC with conserved polar residues of LC7 form a fingerprint region necessary for strong IC•LC7 binding.

The newly identified LC7 recognition sequence on IC is different from that expected in the literature.

The crystallographic LC7 recognition sequence corresponds to IC residues 221-258, which is upstream from the sequence implied by truncation mutations (Susalka et al. 2002) and commonly presumed to be the LC7 recognition site (Susalka et al. 2002; Song et al. 2005; Lo et al. 2006). The proposal that the LC7 recognition sequence on IC corresponds to residues 250-289, immediately preceding a WD40 repeat domain, derives from two sets of observations. First, Susalka *et al.* showed that LC7 binds to IC between residues 1- 322, but does not appreciably bind to a construct ending at residue 250, suggesting that the binding sequence begins after IC residue 250 (numbering relative to *D. melanogaster Cdic*2b gene form) (Susalka et al. 2002). Second, the region preceding IC residue 250 maps to the IC self-association domain (Lo et al. 2006). Similarly, others proposed that apo-IC dimerizes through an interchain coiled-coil based on sequence prediction involving residues 207-237 (Figure 5.1) (see Figure 6 of Nurminsky, D. I. *et al.* 1998) (Nurminsky et al. 1998). Experimental data consistent with formation of an IC-IC interchain coiled-coil includes enhanced helix content arising from light chain binding (see Figure 3 of Nyarko, A., *et al.* 2004; Figure 10 of Benison, G. C., *et al.* 2006) (Nyarko et al. 2004; Benison et al. 2006) as well as enhancement of IC•light chain binding with an IC construct that contains the proposed self-association domain (see Figure 4 of Williams, J. C., *et al.* 2007) (Williams et al. 2007).

NMR spectra of LC7 titrated with an IC construct of residues 250-289 show only six LC7 residues with chemical shift changes > 0.08 ppm (Song et al. 2005). Furthermore, the K_d of 100 μM determined by Song *et al*. is 20-50 fold weaker than the binding affinity of IC constructs reported here. The weak

interaction and minimal chemical shift differences support our conclusion that IC residues 250-289 are not the true recognition sequence.

LC7 binding prevents IC self-association at the proposed self-association domain.

Since the LC7 recognition sequence identified here, residues 221-258, overlaps with the predicted IC self-association domain, residues 207-237 (Figure 5.1), any IC self-association in the presence of bound LC7 must occur N-terminal to Leu221, which is the most N-terminal IC residue in the IC•LC7 crystal structure and 50 Å from Leu221' of the other IC chain (Fig 5.2b). Far from positioning the two IC chains for mutual interactions in the self-association domain, it is not possible for LC7 to hold Leu221 and Leu221' further apart. If IC residues N-terminal to residue Leu221 adopt the extended polypeptide-II conformation observed for unstructured peptides (Hollingsworth *et al.* 2009) and head directly toward each other, more than 12 residues from both chains would be required to close the 50 Å gap before any interaction occurs. Thus with LC7 bound, a coiled-coil cannot form between IC residues 207-237.

LC7 induced fit and IC disorder-to-order transition in dynein assembly.

Conformational variations among the four apo-LC7 chains is likely associated with collective motion of the N-terminal helix and disorder in loops 2 and 6 (Fig 5.2c). In IC-bound LC7, these regions accommodate IC in a well defined average conformation in the IC•LC7 complex consistent with induced fit and mass action selection of LC7 forms receptive to IC binding.

To bind LC7, IC undergoes a disorder-to-order transition. In solution, free IC is primarily disordered, but presumably samples helix-like structure in some of its residues (Benison et al. 2006). The IC segment interacting with LC7 adopts a helical structure in the complex that matches its predicted secondary structure remarkably well, including the turn between the two helices (Appendix Figure A2.5). An analogous disorder-to-order transition in IC also accompanies binding

of Tctex1 or LC8, where the recognition sequence acquires a β-strand structure that adds to the β-sheet of the respective light chain (Benison et al. 2007; Williams et al. 2007; Hall et al. 2009). When fully assembled the IC•Tctex1•LC8•LC7 complex forms an IC duplex with two parallel IC chains bound to three homodimeric light chains; non-interacting regions of IC apparently retain disorder and associated flexibility (Nyarko et al. 2004; Benison et al. 2006; Hall et al. 2009).

Pre-binding of Tctex1 or LC8, whose recognition sequences are three residues apart, results in a 50-fold mutual IC affinity enhancement for the other light chain due to multivalent interactions (Hall et al. 2009). Pre-binding of Tctex1 and LC8 is expected to display a similar multivalent enhancement for IC binding to LC7 albeit of lower magnitude due to the longer (85 residue) disordered linker separating the LC8 and LC7 recognition sequences (Appendix Figure A2.5). However, pre-binding of Tctex1 and LC8 increases binding affinity of IC_{TL7} to LC7 by less than 3-fold relative to IC_7 binding to LC7. It is interesting to note that LC7 binding to prebound IC_{TL7} is better fit to a single-site model than with free IC_7, suggesting bound Tctex1 and LC8 may restrict non-productive LC7 binding (Figure 5.4a, b).

Retained interface residues in robl^Z deletion mutation.

A naturally occurring deletion mutation of LC7 (*robl^Z*), with the entire dimer interface missing, has a phenotype more severely affected than the completely null allele (Bowman *et al.* 1999). One possible reason for the severity of the *robl^Z* phenotype is retained binding activity of *robl^Z* sufficient to compete with LC7 dynein interactions (Bowman et al. 1999). While this suggestion seems unlikely considering that *robl^Z* mutation in *D. melanogaster* results in a 54-residue deletion and a 12-residue insertion between β_2 and β_5 (Figure 5.5a) and that a similar mutation in *H. sapiens* LC7 (Ding et al. 2005) which lacks the 12-residue insertion shows no interaction with IC, it is interesting to note that the retained sequence of *robl^Z* accounts for structural elements with more than 70% of the IC

binding surface (Figure 5.5b). This supports the possibility that a small population of *D. melanogaster robl*^{Z} adopts native-like conformations of α_1, β_1 and β_5 that could be stabilized by IC binding.

Regulation by phosphorylation is an indirect effect.

There is an apparent contradiction between *in vivo* and *in vitro* effects of phosphorylation on IC•LC7 binding. For *in vivo* mammalian systems, IC binds only phosphorylated LC7 (Tang et al. 2002) and the S33A or S74A (numbering relative to *D. melanogaster*) single site mutants abolish IC•LC7 binding (Ding et al. 2005). However, in this work and in studies of mammalian IC there is ample evidence that IC binds unphosphorylated LC7 *in vitro* (Susalka et al. 2002; Lo et al. 2006). Based on the sequence conservation of both LC7 and the LC7 recognition sequence on IC (Figure 5.5a and Appendix Figure A2.4), it is likely that in other organisms IC binds unphosphorylated LC7 *in vitro* as well. In the IC•LC7 structure, the two potential LC7 phosphorylation sites are distant from the IC binding site (Figure 5.5c) suggesting that phosphorylation does not directly affect LC7 binding to IC but may modulate LC7 binding to other proteins. It is possible that interactions between unphosphorylated LC7 and an as yet unidentified protein(s) can either directly block the IC binding site or indirectly prevent IC binding by limiting the structural transitions of α_1, L_2 and L_6 seen between apo and IC-bound LC7.

Vertebrates have two LC7 isoforms (LC7a and LC7b) that are expressed simultaneously in most tissues (Jiang et al. 2001), but at varying levels (Bowman et al. 1999; Jiang et al. 2001; Nikulina *et al.* 2004). Interestingly, the few residues that have conserved sequence differences between paralogs (Appendix Figure A2.4) are primarily located on LC7 surfaces distant from the IC binding interface (Figure 5.5c). The different phosphorylation sites between isoforms and their distance from the IC binding interface suggests that functional differences between isoforms could be modulated by phosphorylation.

The helix segment of bound IC is analogous to an integral part of LC7-related proteins.

LC7, homodimeric Mgl and the heterodimeric MP1•p14 are structural homologs belonging to an ancient superfamily of small subcellular adaptor proteins (Koonin et al. 2000; Ilangovan et al. 2005; Song et al. 2005) (Figure 5.6). A major structural difference between these homologs and LC7 is that Mgl and MP1•p14 contain an amphipathic C-terminal helix (α_3) not present in apo-LC7. Interestingly, α_3 packs in the spot occupied by α_{IC2} in the IC•LC7 complex, although α_3 and α_{IC2} lie in opposite directions. In addition, the orientation of α_1 in the IC•LC7 structure is similar to the orientation of α_1 in Mgl and MP1•p14 (Figure 5.6). Binding of IC to LC7 adds an element of secondary structure to the apo-LC7 fold to make it more like its homologs. Addition of an element of secondary structure to the fold of a light chain also occurs in IC binding to apo-Tctex1 and apo-LC8 (Benison et al. 2008). In these cases a disordered segment of IC is incorporated as a single β-strand into each of the folds of apo-Tctex1 or apo-LC8, and in a manner analogous to IC•LC7, IC completes their fold topology. Integration of a secondary structural elements into the fold of its binding partners appears to be a common theme for assembly of disordered IC with dimeric light chains and may exemplify a general mechanism for assembly of an elongated flexible scaffold in multisubunit complexes.

Assuming the common ancestor of this superfamily has the C-terminal helix, then the IC binding function of LC7 is a relatively recent adaptation for this superfamily. The remarkable placement of α_{IC2} at the position of α_3 in other superfamily members suggests that LC7 or even the IC•LC7 complex might bind Rab6, the human reduced folate carrier or the TGF-β receptor complex at sites different from the IC binding site and equivalent to where other LC7 superfamily proteins bind their partners. The conformational diversity of apo-LC7 suggests that structural flexibility plays a role in its development of new specialized function(s) while retaining ancestral function(s) (James *et al.* 2003). In this view, the loss of

Figure 5.6: Bound IC mimics a helix contained in LC7 homologs. a) The IC•LC7 complex (light orange/orange and grey/steel blue, respectively), b) the homodimeric Mgl complex (grey/steel blue) and c) the heterodimeric MP1•p14 complex (grey and steel blue, respectively). Arrows indicate the N-to-C directionality of helices α_{IC1} and its cognate helix in the other complexes. Figures generated using Pymol with pdb accession codes 1J3W and 1SKO for Mgl and MP1•p14, respectively (DeLano 2002).

Figure 5.6: (*Continued*).

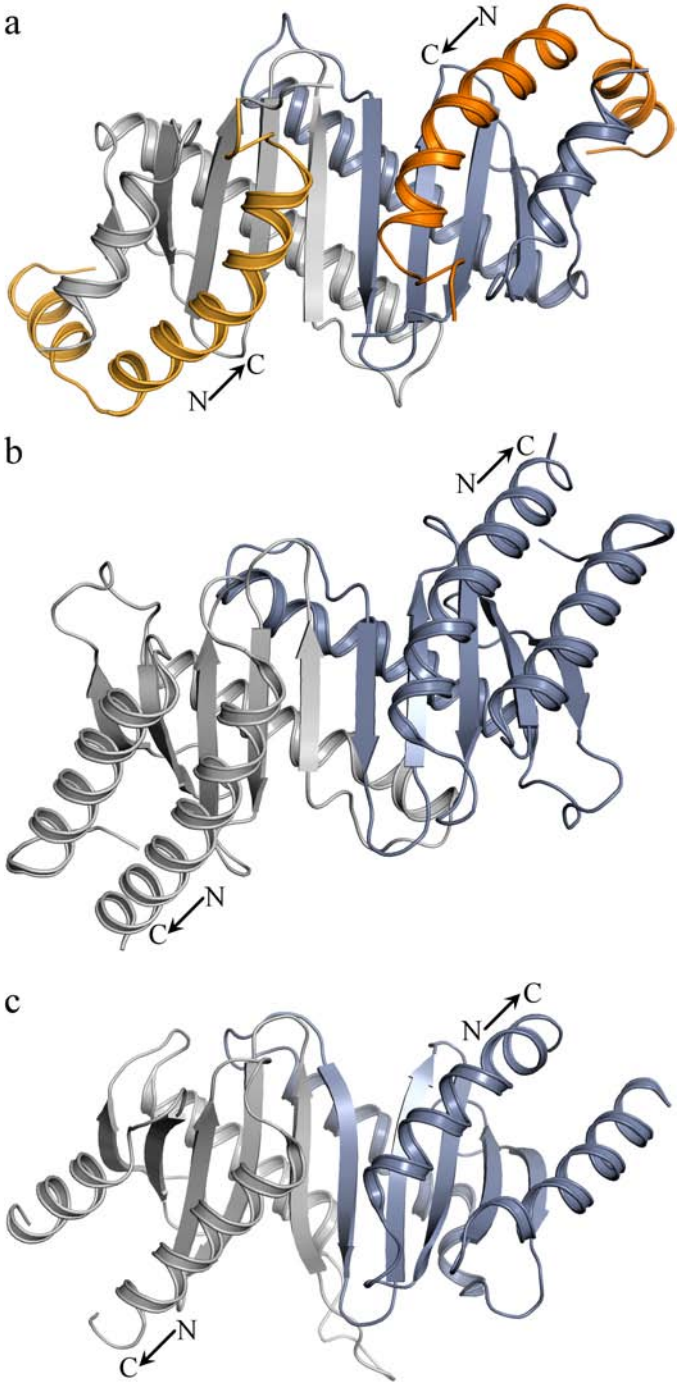

the C-terminal helix was a key step in the evolution of conformational and functional diversity of LC7.

Materials and Methods

Protein preparation.

The gene for *D. melanogaster* LC7 was a generous gift from Dr. T. Hays (University of Minnesota). The LC7 construct and IC constructs were cloned into pCR2.1 TOPO using the TOPO TA cloning kit (Invitrogen, Eugene, OR), then subcloned into pET15d (Novagen, Darmstadt, Germany). The IC construct corresponding to residues 212-260 (IC_7) was cloned into pET SUMO (Invitrogen) which contains an N-terminal SUMO fusion protein. All proteins included an N-terminal hexahistidine tag. Sequences were verified by automated sequencing.

Recombinant proteins were expressed in *Escherichia coli* BL21(DE3) host cell lines. Cells expressing LC7, $IC_{TL\text{-}d7}$, IC_{TL7}, and $IC_{92\text{-}289}$ were grown in LB medium, and cells expressing IC_7 were grown in TB medium. All cells were grown at 37 °C to an A_{600} of ~0.6 and protein expression was induced by addition of isopropyl-1-thio-β-D-galactopyranoside (IPTG). LC7 was induced with 0.4 mM IPTG at 22 °C and IC constructs were induced as previously described and formed inclusion bodies (Makokha et al. 2002). Proteins were initially purified using a nickel-NTA column (Qiagen); the IC constructs were refolded on the column by decreasing the urea concentration. The hexahistidine tag was cleaved from LC7 using FactorXa protease (Novagen) and the SUMO tag was cleaved from IC_7 using Ulp1-Sumo protease (Mossessova *et al.* 2000). Final purification of LC7, $IC_{TL\text{-}d7}$, IC_{TL7}, and $IC_{92\text{-}289}$ was done using size-exclusion chromatography (HiLoad Superdex75 26/60, GE Healthcare). Final purification of IC_7 was done using high performance liquid chromatography on a YMC C-18 column in 0.1% trifluoroacetic acid with a linear gradient (40-65%) of acetonitrile. Protein purity was verified by SDS-PAGE and MALDI-TOF mass spectrometry: LC7 M.W. = 10,823.6 Da (10,823.4 theoretical), IC_{TL7} M.W. = 20,401.8 Da (20,518.5

theoretical), IC_7 = 5,803.6 Da (5,804.5 theoretical) and $IC_{92\text{-}289}$ = 24,122.0 Da (23,935.4 theoretical). The deviation from theoretical mass for IC_{TL7} may be due to N-terminal demethionation and retention of a Na^+ ion. The higher mass of $IC_{92\text{-}289}$ could be due to its low signal to noise and ambiguous centroid mass, or a covalent difference as in IC_{TL7}. Protein concentrations were determined from sequence-based calculation of absorptivity at 280 nm (Wilkins et al. 1999).

X-ray crystallography.

Apo-LC7 and the $IC_{92\text{-}289}$•LC7 complex were stored in 15 mM sodium chloride, 5 mM Tris at pH 7.5. The monomeric concentration of LC7 in both apo-LC7 and the $IC_{92\text{-}289}$•LC7 complex was 0.5 mM, with a two-fold excess of $IC_{92\text{-}289}$. Crystals were obtained at 4 °C using 2 µl hanging drops with an equal volume of reservoir solution equilibrated against a 400 µl reservoir.

In attempts to crystallize a supercomplex of $IC_{92\text{-}289}$•Tctex1•LC8•LC7, $IC_{92\text{-}289}$ was proteolytically degraded, but some apo-LC7 crystals formed. Optimization of these crystals was done using LC7 alone, and diffraction quality apo-LC7 crystals were grown using a reservoir of 20% iso-propanol, 20% PEG 4000, 100 mM sodium citrate at pH 5.6. Rectangular crystals grew to a final size of 0.1 x 0.12 x 0.05 mm^3. For IC•LC7, a 1:500 (v:v) of FactorXa protease (Novagen) was added to a stock solution of $IC_{92\text{-}289}$•LC7 to aid opportunistic crystal lattice formation during *in situ* proteolysis (Dong et al. 2007). Hexagonal rod crystals were obtained using a reservoir of 1 M sodium citrate, 100 mM sodium chloride, 100 mM Tris at pH 7.0. Crystals grew to a final size of 0.25 x 0.06 x 0.06 mm^3 within two weeks. Mass spectrometry analysis of IC•LC7 crystals showed $IC_{92\text{-}289}$ was proteolyzed with no fragments larger than 9 kDa present. Crystals of the IC_7•LC7 complex having the same morphology and diffraction properties as those of IC•LC7 were reproducibly grown using the same crystallization conditions but with a 1.1-fold excess of IC_7 replacing $IC_{92\text{-}289}$ and with no FactorXa protease added.

Crystals were pulled through oil before flash-freezing in loops using liquid nitrogen. For apo-LC7, 1.95 Å resolution oscillation data ($\Delta\varphi$ (= 1.0°) were collected using an in-house Raxis IV system with CuKα-radiation. For IC•LC7, oscillation data ($\Delta\varphi$ = 1.0°) were collected using HHMI beam line 5.0.1 at the Berkeley Advanced Light Source. Data were integrated using Imosflm (Leslie 1992) and scaled using SCALA (Diederichs et al. 1997). For IC•LC7, data were input into the Diffraction Anisotropy Server without B-factor sharpening (Strong *et al.* 2006), and an elliptical resolution boundary of 2.7 x 3.0 x 3.0 Å (a*, b* and c* respectively) was chosen based on the default 3 Fo/σFo cutoff. Thus the IC•LC7 complex has a nominal resolution of 3.0 Å but includes data to 2.7 Å in the a* lattice direction. The apo-LC7 space group was $P2_1$ with unit cell of β =101.8°, a=56.22, b=58.69, c= 65.10 Å; that for IC•LC7 was $P3_2$ with unit cell a=b=107.13, c=65.29 Å. Crystallographic data collection and refinement statistics are summarized in Table 5.2.

Phases were determined for both crystals by molecular replacement using PHASER (McCoy 2007) with PDB structure 2HZ5 (Liu et al. 2006) as the search model. In each case two dimers of LC7 were placed. Electron density maps calculated for the IC•LC7 complex show extra helical density for four IC chains. Model building was performed in Coot (Emsley et al. 2004) and both apo-LC7 and the IC•LC7 complex were refined using restrained isotropic B-factor refinement with one TLS domain per chain in REFMAC (Murshudov et al. 1997). NCS restraints were applied to the four IC and LC7 chains in the IC•LC7 complex. To confirm the accuracy of the model, unbiased electron density maps were generated starting with a molecular replacement model leaving out side chains for residues R71, R73, E78 and Q93. Refinement of this model with poly-Ala helices for α_{IC2}, and the final model, show unbiased density for residues R71, R73, E78 and Q93 of LC7 and E252 and N253 of IC.

Solvent accessible surface area buried upon complex formation was calculated using SURFACE RACER 5.0 (Tsodikov et al. 2002). The atomic

Table 5.2: Data collection and refinement statistics for apo-LC7 and the IC•LC7 complex.

Data	**apo-LC7**	**IC•LC7[a]**
Resolution (Å)	63.72 - 1.95 (2.00 - 1.95)[b]	53.6 - 3.0 (3.15 - 3.0)
Completeness (%)	98.9 (98.9)	100 (100)
I/σ	9.15 (2.5)	6.4 (0.80)
R_{meas}	0.14 (0.46)	0.09 (1.12)
R_{pim}	0.07 (0.23)	0.04 (0.47)
Total Reflections	271,466	95,560
Unique Reflections	27,041	15,919
Refinement		
Resolution (Å)	63.72 - 1.95 (2.00 - 1.95)	53.6 - 2.7 (3.15 - 3.0 / 2.86- 2.7)
No. Reflections Used	27,041 (1,802)	17,314 (839 / 393)
R_{cryst}	0.19 (0.28)	0.20 (0.31 / 0.42)
R_{free}	0.25 (0.37)	0.24 (0.40 / 0.47)
Average B-factor (all atoms) (Å^2)[c]	27	103
RMSD from ideal:		
Bond length (Å)	0.022	0.018
Bond angles (°)	1.9	1.9
φ,ψ prefered (%)[d]	95.5	86.1
φ,ψ allowed (%)	100	99.2

[a]Data statistics are reported for a nominal resolution limit of 3.0 Å for which all collected data were used; as refinement included some additional data to 2.7 Å (see Methods), the refinement statistics are reported with that cutoff, and information is given for both the 3 Å and 2.7 Å highest resolution bins.
[b]Values in parentheses are for the highest resolution bin.
[c]Average B-factors are within the acceptable range for their resolution (Sarma *et al.* 2003).
[d]Reported values are based on MOLPROBITY (Lovell *et al.* 2003). The values using PROCHECK (Laskowski 1993) are within 4% of the MOLPROBITY values. The only φ,ψ-outlier is Lys85 in loop 6, which has weak density and so is not reliably determined. Lys85 has (φ,ψ) ≈ (-115°,55°) in apo-LC7 and (φ,ψ) ≈ (-80°,100) in the IC•LC7 complex.

coordinates and structure factors for apo-LC7 and the IC•LC7 complex have been deposited into the PDB with accession numbers 3L7H and 3L9K, respectively.

Isothermal titration calorimetry.

Proteins were dialyzed into 50 mM sodium phosphate, 50 mM sodium chloride, 1 mM sodium azide at pH 7.5. Thermodynamics of binding were determined at 25 °C using a VP-ITC isothermal titration calorimeter (MicroCal, Northampton, MA). Experiments were conducted with IC_7 and IC_{TL7} in the sample cell and LC7 in the syringe. IC_{TL7} was pre-bound by a 4-fold excess of Tctex1 and

LC8. Data were processed using the manufacturer's supplied software package, Origin 7.0 (OriginLab Corp., Northampton, MA). Heat of dilution, estimated to be equal to the enthalpy of the final injection, was subtracted from the binding data prior to fitting. LC7 binds IC_7 or IC_{TL7}•Tctex1•LC8 with a stoichiometry of 1.0 ± 0.1, but whereas IC_{TL7}•Tctex1•LC8 is well fit by a single-site binding model (**A + B** → **AB**, where **A** and **B** refer to a single chain of IC and LC7, respectively), IC_7 data show small deviations from the best fit. Nonetheless, a single-site binding model was chosen for IC_7•LC7 in the absence of further information justifying additional fitting parameters. For all experiments the "c value" ($c = [protein]_{sample\ cell} \times K_d^{-1}$) was within the 5 to 500 range required for reliable determination of association constants (Turnbull et al. 2003) using cell/syringe concentrations of 0.028/0.55 and 0.045/0.55 mM for IC_7 and IC_{TL7}, respectively. Average values are reported with error estimation from the difference between experimental repeats (Table 5.1).

Size exclusion chromatography and multi-angle light scattering.

To determine association states, samples from ITC were run on an analytical size-exclusion column (Superdex200 10/300, GE Healthcare) at 0.5 ml/min in 200 mM sodium sulfate, 50 mM sodium phosphate, 1 mM sodium azide

at pH 7.3. The monomeric concentrations of Tctex1, LC8, LC7 and the IC_{TL7}•Tctex1•LC8•LC7 complex were 0.135, 0.135, 0.068 and 0.045 mM at loading, respectively. Multi-angle light scattering (MALS) (mini-Dawn, Wyatt Technology) and refractive index (ProStar 350, Varian) data were collected and processed using ASTRA v5.1.9.1 (Wyatt Technology). The peak corresponding to the IC_{TL7}•Tctex1•LC8•LC7 complex was collected during elution and concentrated 10-fold for SDS-PAGE analysis.

Acknowledgements

The authors thank Andrea Hall, Dale Tronrud, and Leslie Coonrod for assistance with X-ray data collection and processing. Funding support was provided by the AHA and NSF. We acknowledge the support of HHMI beam line 5.0.1 of the Advanced Light Source synchrotron and the nucleic acid, protein and mass spectrometry facilities and services core in the OSU Environmental Health Sciences Center (NIH/NIEHS 00210).

Chapter 6

Summary and future work

Summary

The cargo binding sub-domain of dynein is comprised of IC and associated light chain proteins Tctex1, LC8 and LC7. The studies described herein were undertaken to elucidate the function of these proteins with the ultimate goal of better understanding the role of each in the assembly and regulation of the dynein cargo binding sub-domain. This final chapter will summarize the results presented in previous chapters and describe the aim of future projects designed to take up where these works end.

Changes in LC8 internal dynamics are partner dependent.

Tctex1 and LC8 are homodimers with a distinct crossover β-strand at the dimer interface (β_3) (Fig. 1.4a, b). When Tctex1 or LC8 binds IC, β_3 and $\beta_{3'}$ directly contact IC, which folds into a 6^{th} strand at the dimer interface (Fig. 2.1a). Phosphorylation of Tctex1 or LC8 disrupts IC association, and in the case of LC8 results in monomerization (Song et al. 2007; Song et al. 2008). LC8 backbone dynamics show β_3 is disordered in the H55K monomer of LC8 (Fig. 2.7), and becomes increasingly ordered in the LC8 dimer or LC8 complexes with peptides from Bim, IC, nNOS or Swa (Fig 2.9, Fig 3.4). Interestingly, LC8 backbone heterogeneity is differentially retained between peptides, with IC or nNOS complexes retaining more heterogeneity than Bim or Swa complexes. These results demonstrate LC8 backbone dynamics are important for partner recognition, and raise the possibility that differences in LC8 internal dynamics may play a role in differential downstream regulation of LC8•partners complexes.

Furthermore, changes in LC8 backbone dynamics upon peptide binding correlate with ITC determined entropies, with a large unfavorable entropic cost accompanying Bim or Swa binding relative to IC and nNOS (Table 3.1). ITC data also shows LC8 binds the first and second peptide of Bim or Swa with distinct thermodynamic parameters (Fig. 3.4), with the large unfavorable entropy change occurring during the second binding event. The correlation between measured

dynamics and entropy suggest the unfavorable entropy of the second peptide binding event may be due to changes in LC8 dynamics, with the second binding event locking LC8 into the lower entropic state seen in NMR experiments. This model for LC8 binding is therefore consistent with an allosteric interaction containing contributions from dynamics.

Adjacent Tctex1 and LC8 binding sites provide reciprocal binding enhancement.

Tctex1 and LC8 are homologs which bind IC with similar affinities ($K_d \approx 8$ μM, Table 4.1), and in an analogous manner both fold natively-disordered IC into a β-strand at their binding sites. Additionally, Tctex1 and LC8 are bound at adjacent sites on IC (Fig. 4.3) which contain similar sequences in vertebrates (SKVTQV and SKETQT in *D. rerio*, Appendix Table A1.1). Interestingly, while IC is the only example of a protein with adjacent Tctex1 and LC8 binding sites, two or more adjacent LC8 binding sites exist in several proteins (Rodriguez-Crespo et al. 2001; Stelter et al. 2007), suggesting an ancestral IC might have had two adjacent LC8 sites. Interestingly, for adjacent Tctex1 and LC8 sites (IC_{TL}), there is a 50-fold binding enhancement for Tctex1 or LC8 binding to IC if the other light chain is pre-bound to IC. In contrast, IC engineered to contain a second LC8 site in place of the Tctex1 site (IC_{LL}) enjoys a 1000-fold binding enhancement arising purely from a favorable change in system entropy (Fig. 4.5).

There are no examples of adjacent LC8 sites in naturally occurring IC sequences, instead adjacent Tctex1 and LC8 sites exist without exception. Selective pressures must therefore exist to maintain adjacent Tctex1 and LC8 binding sites, presumably in favor of the 50-fold enhancement over the 1000-fold potential offered by adjacent LC8 sites.

For both IC_{TL} and IC_{LL}, binding enhancement is due to an entropic effect known in a number of biological processes as the chelate effect. The first light chain dimer connects two monomeric IC chains, reducing IC translational and rotational entropies and resulting in a higher affinity (Appendix Figure A1.3). The

purely entropic enhancement seen for IC_{LL} is a remarkable proof of principle for the entropic origin of the chelate effect. The smaller enhancement seen for IC_{TL} is due to additional destabilizing interactions occurring during the second binding event which offset some of the favorable enhancement from the chelate effect.

A clue for the origin of the additional destabilizing effects in IC_{TL} is seen in the heat capacity change between the first and second binding events (Fig. 4.4, 4.5b and c). A change in heat capacity is normally associated with nonpolar surface burial, suggesting additional contact area is created during the second binding event, presumably at the IC•Tctex1 interface.

Analysis of the IC•Tctex1•LC8 complex suggests when LC8 binds the IC•Tctex1 complex, the two C-terminal ends of the Tctex1 recognition site would be held more tightly to the Tctex1 surface, but the N-terminal ends should not be affected (Fig. 4.3). If the observed change in heat capacity is due to additional IC•Tctex1 contact, this would correspond to the last four residues of the Tctex1 recognition site. Comparison of Tctex1 binding sequences on IC show the four C-terminal residues have the highest conservation between species (Appendix Table A1.1). These results therefore suggest the last four C-terminal residues of the Tctex1 recognition sequences may be responsible for attenuating some of favorable enhancement from the chelate effect to fit the functional needs of the dynein system.

LC7 recruitment to dynein is an indirect effect of phosporylation.

The last protein of the cargo binding sub-domain of dynein, LC7, binds IC approximately 85 residues C-terminal to the LC8 binding site (Appendix Figure A2.5). Potentially because of the longer linker separating light chain binding sites, Tctex1 and LC8 pre-bound to IC do not significantly enhance IC•LC7 association, despite evidence that Tctex1 and LC8 affect the nature of the IC•LC7 interaction (Fig. 5.4).

Like Tctex1 and LC8, LC7 is also a homodimer though it is not related to Tctex1 or LC8 (Fig. 1.4c). LC7 belongs to an ancient protein superfamily with members thought to be involved in regulation of NTPase activity (Koonin et al. 2000). LC7 has multiple non-dynein interaction partners, and the IC•LC7 structure presented here is the first glimpse of the molecular details of LC7 interacting with any of its partners.

While IC binding to Tctex1 or LC8 is disrupted by light chain phosphorylation, the opposite is true for LC7, which only binds IC after phosporylation *in vivo* (Tang et al. 2002). Studies described here provide ample evidence that IC is able to bind unphosphorylated LC7 *in vitro*; furthermore, analysis of the IC•LC7 structure shows the potential LC7 phosphorylation sites do not interact with IC (Fig. 5.5c). These two observations lead us to conclude phosphorylation does not directly affect IC•LC7 interaction, but instead must modulate LC7 binding to an as yet unidentified *in vivo* factor(s) which prevents IC•LC7 association in the absence of phosphorylation.

Previous work aimed at determining the LC7 recognition sequence on IC identified a sequence starting 30 residues upstream of the crystallographic LC7 recognition sequence (Susalka et al. 2002). Additionally, the LC7 recognition sequence identified here partially overlaps the C-terminal half of a region previously identified as the IC self-association domain (Fig. 5.1) (Nurminsky et al. 1998; Lo et al. 2006). Since LC7 is constitutively present in dynein, if IC does self-associate, it must do so N-terminal to the LC7 recognition sequence. Strikingly, the most N-terminal residues of the two IC chains are 50 Å apart in the IC•LC7 structure (Fig 5.2b). Far from positioning the two IC chains for mutual interaction, LC7 holds the two IC chains as far away from each other as possible, such that it is not possible for the residues remaining in the IC self-association domain to contact each other. Thus these results provide valuable information on the function of LC7 as well as correcting decade long misconceptions about the nature of the IC•LC7 interaction.

In conclusion, the results of these experiments provide three important insights into the dynein cargo attachment sub-domain. First, changes in LC8 internal dynamics are partner dependent and may play a role in differential downstream regulation. Secondly, adjacent Tctex1 and LC8 binding sites have evolved to reciprocally provide tighter binding tuned to the functional needs of the system. Lastly, LC7 recruitment to dynein is an indirect effect of phosporylation and appears to prevent the formation of a coiled-coil immediately N-terminal to the LC7 recognition sequence.

Future work

Previous experiments have shown Tctex1 mutants in *D. melanogaster* result in male sterility through an unknown mechanism (Caggese et al. 2001; Li et al. 2004). My data shows Tctex1 enhances LC8 affinity for IC by 50-fold, suggesting the sterile phenotype may be due to impaired assembly of the dynein cargo binding sub-domain.

To determine whether the sterile phenotype is due to impaired dynein function, future experiments could be performed to test the *in vivo* effect of IC mutants that have the Tctex1 binding site replaced with a poly-alanine sequence or a second LC8 binding motif. A poly-alanine mutant is expected to have impaired dynein assembly relative to wild-type IC, whereas IC with a second LC8 binding site will not. If the sterile phenotype is due to Tctex1 involvement in dynein assembly, the poly-alanine IC mutant should also have a sterile phenotype.

IC has two distinct domains, a primarily disordered N-terminal domain containing light chain binding sites, and an ordered C-terminal domain containing the heavy chain binding site (Habura et al. 1999) (Fig 1.1). Sequence prediction strongly suggests IC folds into a β-propeller shortly after the LC7 recognition sequence (Wilkerson et al. 1995; Nurminsky et al. 1998); thus, LC7 marks the beginning of the boundary separating the two domains of IC. N-terminal to the LC7 binding site, the two IC chains are held apart by LC7, but C-terminal to the

LC7 binding site, the two IC chains are positioned closer together (Fig 5.2b). Since the β-propeller region of IC is the point of connection between the cargo binding and motor sub-domains, future experiments could be performed to determine what role LC7 plays in the formation of the predicted β-propeller and the connecting point of the two dynein sub-domains.

Our strategy till now has been to separately analyze components of the dynein complex; future efforts should build on our successes while the focus onward to the C-terminal domain of IC, but also incorporate an outward expansion to *in vivo* test systems. Armed with this information, a complete picture of the assembly and regulation of the dynein cargo binding sub-domain will emerge.

Bibliography

Ashokkumar, B., S. M. Nabokina, T. Y. Ma and H. M. Said (2009). "Identification of dynein light chain road block-1 as a novel interaction partner with the human reduced folate carrier." Am J Physiol Gastrointest Liver Physiol **297**(3): G480-7.

Barbar, E. (2008). "Dynein Light Chain LC8 Is a Dimerization Hub Essential in Diverse Protein Networks." Biochemistry **47**(2): 503-508.

Barbar, E. and M. Hare (2004). "Characterization of the cargo attachment complex of cytoplasmic dynein using NMR and mass spectrometry." Methods Enzymol **380**: 219-41.

Barbar, E., B. Kleinman, D. Imhoff, M. G. Li, T. S. Hays and M. Hare (2001). "Dimerization and folding of LC8, a highly conserved light chain of cytoplasmic dynein." Biochemistry **40**(6): 1596-1605.

Bauch, A., K. S. Campbell and M. Reth (1998). "Interaction of the CD5 cytoplasmic domain with the Ca2+/calmodulin-dependent kinase II delta." European Journal Of Immunology **28**(7): 2167.

Benison, G., D. S. Berkholz and E. Barbar (2007). "Protein assignments without peak lists using higher-order spectra." J Magn Reson **189**(2): 173-81.

Benison, G., P. A. Karplus and E. Barbar (2007). "Structure and dynamics of LC8 complexes with KXTQT-motif peptides: Swallow and dynein intermediate chain compete for a common site." JMB **371**: 457-468.

Benison, G., P. A. Karplus and E. Barbar (2008). "The interplay of ligand binding and quaternary structure in the diverse interactions of dynein light chain LC8." JMB **384**(4): 954-66.

Benison, G., A. Nyarko and E. Barbar (2006). "Heteronuclear NMR Identifies a Nascent Helix in Intrinsically Disordered Dynein Intermediate Chain: Implications for Folding and Dimerization." JMB **362**: 1082-1093.

Bertozzi, C. R. and L. L. Kiessling (2001). "Chemical glycobiology." Science **291**(5512): 2357-64.

Blom, N., S. Gammeltoft and S. Brunak (1999). "Sequence and structure-based prediction of eukaryotic protein phosphorylation sites." J Mol Biol **294**(5): 1351-62.

Bowman, A. B., R. S. Patel-King, S. E. Benashski, J. M. McCaffery, L. S. Goldstein and S. M. King (1999). "Drosophila roadblock and Chlamydomonas LC7: a conserved family of dynein-associated proteins involved in axonal transport, flagellar motility, and mitosis." JCB **146**(1): 165-80.

Boylan, K. L. M. and T. S. Hays (2002). "The gene for the intermediate chain subunit of cytoplasmic dynein is essential in Drosophila." Genetics **162**(3): 1211-1220.

Breslow, R., Belvedere, S.,Gershell, L., and Leung, D. (2000). "The Chelate Effect in Binding, Catalysis, and Chemotherapy." Pure Applied Chemistry **72**(3): 333-342.

Brokaw, C. J. (1972). "Flagellar movement: a sliding filament model." Science **178**(60): 455-62.

Burgess, S. A., M. L. Walker, H. Sakakibara, P. J. Knight and K. Oiwa (2003). "Dynein structure and power stroke." Nature **421**(6924): 715-8.

Caggese, C., R. Moschetti, G. Ragone, P. Barsanti and R. Caizzi (2001). "dtctex-1, the Drosophila melanogaster homolog of a putative marine t-complex distorter encoding a dynein light chain, is required for production of functional sperm." Molecular Genetics and Genomics **265**(3): 436-444.

Campbell, K. S., S. Cooper, M. Dessing, S. Yates and A. Buder (1998). "Interaction of p59(fyn) kinase with the dynein light chain, Tctex-1, and colocalization during cytokinesis." Journal Of Immunology **161**(4): 1728.

Carter, A. P., J. E. Garbarino, E. M. Wilson-Kubalek, W. E. Shipley, C. Cho, R. A. Milligan, R. D. Vale and I. R. Gibbons (2008). "Structure and functional role of dynein's microtubule-binding domain." Science **322**(5908): 1691-5.

Chatterjee, A., P. M. Krishna Mohan, A. Prabhu, A. Ghosh-Roy and R. V. Hosur (2007). "Equilibrium unfolding of DLC8 monomer by urea and guanidine hydrochloride: Distinctive global and residue level features." Biochimie **89**(1): 117-34.

Chen, Y. M., C. Gerwin and Z. H. Sheng (2009). "Dynein light chain LC8 regulates syntaphilin-mediated mitochondrial docking in axons." J Neurosci **29**(30): 9429-38.

Cheng, X., M. L. Gonzalez and J. C. Lee (1993). "Energetics of intersubunit and intrasubunit interactions of Escherichia coli adenosine cyclic 3',5'-phosphate receptor protein." Biochemistry **32**(32): 8130-9.

Cho, C., S. L. Reck-Peterson and R. D. Vale (2008). "Regulatory ATPase sites of cytoplasmic dynein affect processivity and force generation." JBC **283**(38): 25839-45.

Clore, G. M., Szabo, A., Bax, A., Kay, L. E., Driscoll, P. C., Gronenborn, A. M. (1990). "Deviations from the Simple Two-Parameter Model-Free Approach to the Interpretation of Nitrogen-15 Nuclear Magnetic Relaxation of Proteins." JACS **112**: 4989–4991.

Cole, C., J. D. Barber and G. J. Barton (2008). "The Jpred 3 secondary structure prediction server." Nucleic Acids Res **36**(Web Server issue): W197-201.

Compton, D. A. (2000). "Spindle assembly in animal cells." Annual Review of Biochemistry **69**: 95-114.

Crepieux, P., H. Kwon, N. Leclerc, W. Spencer, S. Richard, R. T. Lin and J. Hiscott (1997). "I kappa B alpha physically interacts with a cytoskeleton-associated protein through its signal response domain." Molecular and Cellular Biology **17**(12): 7375.

Crooks, G. E., G. Hon, J. M. Chandonia and S. E. Brenner (2004). "WebLogo: a sequence logo generator." Genome Res **14**(6): 1188-90.

Delaglio, F., S. Grzesiek, G. W. Vuister, G. Zhu, J. Pfeifer and A. Bax (1995). "NMRPipe: a multidimensional spectral processing system based on UNIX pipes." J Biomol NMR **6**(3): 277-93.

DeLano, W. L. (2002). The PyMOL Molecular Graphics System. San Carlos, CA, DeLano Scientific.

Dhani, S. U., R. Mohammad-Panah, N. Ahmed, C. Ackerley, M. Ramjeesingh and C. E. Bear (2003). "Evidence for a functional interaction between the CIC-2 chloride channel and the retrograde motor dynein complex." JBC **278**(18): 16262-16270.

Dick, T., K. Ray, H. K. Salz and W. Chia (1996). "Cytoplasmic dynein (ddlc1) mutations cause morphogenetic defects and apoptotic cell death in Drosophila melanogaster." Molecular and Cellular Biology **16**(5): 1966-1977.

Diederichs, K. and P. A. Karplus (1997). "Improved R-factors for diffraction data analysis in macromolecular crystallography." Nat Struct Biol **4**(4): 269-75.

Ding, W., Q. Tang, V. Espina, L. A. Liotta, D. T. Mauger and K. M. Mulder (2005). "A transforming growth factor-beta receptor-interacting protein frequently mutated in human ovarian cancer." Cancer Res **65**(15): 6526-33.

Dong, A., X. Xu, A. M. Edwards, C. Chang, M. Chruszcz, M. Cuff, M. Cymborowski, et al. (2007). "In situ proteolysis for protein crystallization and structure determination." Nat Methods **4**(12): 1019-21.

Dosset, P., J. C. Hus, D. Marion and M. Blackledge (2001). "A novel interactive tool for rigid-body modeling of multi-domain macromolecules using residual dipolar couplings." J Biomol NMR **20**(3): 223-31.

Dunker, A. K., M. S. Cortese, P. Romero, L. M. Iakoucheva and V. N. Uversky (2005). "Flexible nets. The roles of intrinsic disorder in protein interaction networks." FEBS J **272**(20): 5129-48.

Echeverri, C. J., B. M. Paschal, K. T. Vaughan and R. B. Vallee (1996). "Molecular characterization of the 50-kd subunit of dynactin reveals function for the complex in chromosome alignment and spindle organization during mitosis." JCB **132**(4): 617-633.

Emsley, P. and K. Cowtan (2004). "Coot: model-building tools for molecular graphics." Acta Crystallogr D Biol Crystallogr **60**(Pt 12 Pt 1): 2126-32.

Epstein, E., A. Sela-Brown, I. Ringel, R. Kilav, S. M. King, S. E. Benashski, J. K. Yisraeli, J. Silver and T. Naveh-Many (2000). "Dynein light chain binding to a 3 '-untranslated sequence mediates parathyroid hormone mRNA association with microtubules." Journal of Clinical Investigation **105**(4): 505-512.

Fan, J. S., Q. Zhang, H. Tochio, M. Li and M. J. Zhang (2001). "Structural basis of diverse sequence-dependent target recognition by the 8 kDa dynein light chain." JMB **306**(1): 97-108.

Fan, J. S., Q. Zhang, H. Tochio and M. Zhang (2002). "Backbone dynamics of the 8 kDa dynein light chain dimer reveals molecular basis of the protein's functional diversity." J Biomol NMR **23**(2): 103-14.

Fan, J. S., Q. A. Zhang, M. Li, H. Tochio, T. Yamazaki, M. Shimizu and M. J. Zhang (1998). "Protein inhibitor of neuronal nitric-oxide synthase, PIN,

binds to a 17-amino acid residue fragment of the enzyme."JBC **273**(50): 33472-33481.

Farrow, N. A., O. Zhang, J. D. Forman-Kay and L. E. Kay (1994). "A heteronuclear correlation experiment for simultaneous determination of 15N longitudinal decay and chemical exchange rates of systems in slow equilibrium." J Biomol NMR **4**(5): 727-34.

Faulkner, N. E., D. L. Dujardin, C. Y. Tai, K. T. Vaughan, C. B. O'Connell, Y. Wang and R. B. Vallee (2000). "A role for the lissencephaly gene LIS1 in mitosis and cytoplasmic dynein function." Nat Cell Biol **2**(11): 784-91.

Frederick, K. K., M. S. Marlow, K. G. Valentine and A. J. Wand (2007). "Conformational entropy in molecular recognition by proteins." Nature **448**(7151): 325-9.

Fuhrmann, J. C., S. Kins, P. Rostaing, O. El Far, J. Kirsch, M. Sheng, A. Triller, H. Betz and M. Kneussel (2002). "Gephyrin interacts with Dynein light chains 1 and 2, components of motor protein complexes." J Neurosci **22**(13): 5393-402.

Gepner, J., M. G. Li, S. Ludmann, C. Kortas, K. Boylan, S. J. P. Iyadurai, M. McGrail and T. S. Hays (1996). "Cytoplasmic Dynein Function Is Essential In Drosophila Melanogaster." Genetics **142**(3): 865-878.

Gibbons, I. R., J. E. Garbarino, C. E. Tan, S. L. Reck-Peterson, R. D. Vale and A. P. Carter (2005). "The affinity of the dynein microtubule-binding domain is modulated by the conformation of its coiled-coil stalk." JBC **280**(25): 23960-5.

Gill, S., D. Cleveland and T. Schroer (1994). "Characterization Of Dlc-a and Dlc-B, 2 Families Of Cytoplasmic Dynein Light-Chain Subunits." Molecular Biology Of the Cell **5**(6): 645.

Gorshkova, I., J. L. Moore, K. H. McKenney and F. P. Schwarz (1995). "Thermodynamics of cyclic nucleotide binding to the cAMP receptor protein and its T127L mutant." JBC **270**(37): 21679-83.

Habura, A., I. Tikhonenko, R. L. Chisholm and M. P. Koonce (1999). "Interaction mapping of a dynein heavy chain. Identification of dimerization and intermediate-chain binding domains." JBC **274**(22): 15447-53.

Hafezparast, M., R. Klocke, C. Ruhrberg, A. Marquardt, A. Ahmad-Annuar, S. Bowen, et al. (2003). "Mutations in dynein link motor neuron degeneration to defects in retrograde transport." Science **300**(5620): 808-12.

Hall, J., A. Hall, N. Pursifull and E. Barbar (2008). "Differences in dynamic structure of LC8 monomer, dimer, and dimer-peptide complexes." Biochemistry **47**(46): 11940-52.

Hall, J., P. A. Karplus and E. Barbar (2009). "Multivalency in the assembly of intrinsically disordered Dynein intermediate chain." JBC **284**(48): 33115-21.

Harrison, A., P. Olds-Clarke and S. M. King (1998). "Identification of the t complex-encoded cytoplasmic dynein light chain Tctex1 in inner arm I1

supports the involvement of flagellar dyneins in meiotic drive." JCB **140**(5): 1137-1147.

Herzig, R. P., U. Andersson and R. C. Scarpulla (2000). "Dynein light chain interacts with NRF-1 and EWG, structurally and functionally related transcription factors from humans and Drosophila." Journal of Cell Science **113**(23): 4263-4273.

Hodi, Z., A. L. Nemeth, L. Radnai, C. Hetenyi, K. Schlett, A. Bodor, A. Perczel and L. Nyitray (2006). "Alternatively spliced exon B of myosin Va is essential for binding the tail-associated light chain shared by dynein." Biochemistry **45**(41): 12582-95.

Hollingsworth, S. A., D. S. Berkholz and P. A. Karplus (2009). "On the occurrence of linear groups in proteins." Protein Sci **18**(6): 1321-5.

Houtman, J. C., P. H. Brown, B. Bowden, H. Yamaguchi, E. Appella, L. E. Samelson and P. Schuck (2007). "Studying multisite binary and ternary protein interactions by global analysis of isothermal titration calorimetry data in SEDPHAT: application to adaptor protein complexes in cell signaling." Protein Sci **16**(1): 30-42.

Houtman, J. C., H. Yamaguchi, M. Barda-Saad, A. Braiman, B. Bowden, E. Appella, P. Schuck and L. E. Samelson (2006). "Oligomerization of signaling complexes by the multipoint binding of GRB2 to both LAT and SOS1." Nat Struct Mol Biol **13**(9): 798-805.

Hwang, T. L., P. C. van Zijl and S. Mori (1998). "Accurate quantitation of water-amide proton exchange rates using the phase-modulated CLEAN chemical EXchange (CLEANEX-PM) approach with a Fast-HSQC (FHSQC) detection scheme." J Biomol NMR **11**(2): 221-6.

Ilangovan, U., W. Ding, Y. Zhong, C. L. Wilson, J. C. Groppe, J. T. Trbovich, J. Zuniga, B. Demeler, Q. Tang, G. Gao, K. M. Mulder and A. P. Hinck (2005). "Structure and dynamics of the homodimeric dynein light chain km23." JMB **352**(2): 338-54.

Imamula, K., T. Kon, R. Ohkura and K. Sutoh (2007). "The coordination of cyclic microtubule association/dissociation and tail swing of cytoplasmic dynein." PNAS USA **104**(41): 16134-9.

Jacob, Y., H. Badrane, P. E. Ceccaldi and N. Tordo (2000). "Cytoplasmic dynein LC8 interacts with lyssavirus phosphoprotein." Journal of Virology **74**(21): 10217-10222.

Jaffrey, S. R. and S. H. Snyder (1996). "PIN: An associated protein inhibitor of neuronal nitric oxide synthase." Science **274**(5288): 774.

James, L. C. and D. S. Tawfik (2003). "Conformational diversity and protein evolution--a 60-year-old hypothesis revisited." Trends Biochem Sci **28**(7): 361-8.

Jencks, W. P. (1981). "On the attribution and additivity of binding energies." PNAS USA **78**(7): 4046-4050.

Jiang, J. M., L. Yu, X. H. Huang, X. S. Chan, D. Li, Y. Z. Zhang, L. Tang and S. Y. Zhao (2001). "Identification of two novel human dynein light chain

genes, DNLC2A and DNLC2B, and their expression changes in hepatocellular carcinoma tissues from 68 Chinese patients." Gene **281**(1-2): 103-113.

Jin, Q., W. Ding and K. M. Mulder (2007). "Requirement for the dynein light chain km23-1 in a Smad2-dependent transforming growth factor-beta signaling pathway." JBC **282**(26): 19122-32.

Jin, Q., G. Gao and K. M. Mulder (2009). "Requirement of a dynein light chain in TGFbeta/Smad3 signaling." J Cell Physiol **221**(3): 707-715.

Kaiser, F. J., K. Tavassoli, G. J. Van den Bemd, G. T. Chang, B. Horsthemke, T. Moroy and H. J. Ludecke (2003). "Nuclear interaction of the dynein light chain LC8a with the TRPS1 transcription factor suppresses the transcriptional repression activity of TRPS1." Hum Mol Genet **12**(11): 1349-58.

Kardon, J. R., S. L. Reck-Peterson and R. D. Vale (2009). "Regulation of the processivity and intracellular localization of Saccharomyces cerevisiae dynein by dynactin." PNAS USA **106**(14): 5669-74.

Kiessling, L. L., J. E. Gestwicki and L. E. Strong (2006). "Synthetic multivalent ligands as probes of signal transduction." Angew Chem Int Ed Engl **45**(15): 2348-68.

King, S. J., C. L. Brown, K. C. Maier, N. J. Quintyne and T. A. Schroer (2003). "Analysis of the dynein-dynactin interaction in vitro and in vivo." Molecular Biology of the Cell **14**(12): 5089-5097.

King, S. J. and T. A. Schroer (2000). "Dynactin increases the processivity of the cytoplasmic dynein motor." Nature Cell Biology **2**(1): 20-24.

King, S. M. (2010). "Sensing the mechanical state of the axoneme and integration of Ca2+ signaling by outer arm dynein." Cytoskeleton (Hoboken) **67**(4): 207-13.

King, S. M., E. Barbarese, J. F. Dillman, R. S. PatelKing, J. H. Carson and K. K. Pfister (1996). "Brain cytoplasmic and flagellar outer arm dyneins share a highly conserved M(r) 8,000 light chain." JBC **271**(32): 19358-19366.

Kon, T., K. Imamula, A. J. Roberts, R. Ohkura, P. J. Knight, I. R. Gibbons, S. A. Burgess and K. Sutoh (2009). "Helix sliding in the stalk coiled coil of dynein couples ATPase and microtubule binding." Nat Struct Mol Biol **16**(3): 325-33.

Kon, T., M. Nishiura, R. Ohkura, Y. Y. Toyoshima and K. Sutoh (2004). "Distinct functions of nucleotide-binding/hydrolysis sites in the four AAA modules of cytoplasmic dynein." Biochemistry **43**(35): 11266-74.

Koonin, E. V. and L. Aravind (2000). "Dynein light chains of the Roadblock/LC7 group belong to an ancient protein superfamily implicated in NTPase regulation." Current Biology **10**(21): R774-R776.

Krishna Mohan, P. M. (2007). "Unfolding energetics and conformational stability of DLC8 monomer." Biochimie **89**(11): 1409-15.

Krishna Mohan, P. M., M. Barve, A. Chatterjee, A. Ghosh-Roy and R. V. Hosur (2008). "NMR comparison of the native energy landscapes of DLC8 dimer and monomer." Biophys Chem **134**(1-2): 10-9.

Laskowski, R. A., MacArthur, M. W., Moss, D. S., Thornton, J. M., (1993). "PROCHECK: a program to check the stereochemical quality of protein structures." J. App. Cryst. **26**(2): 283-291.

Lee, A. L., S. A. Kinnear and A. J. Wand (2000). "Redistribution and loss of side chain entropy upon formation of a calmodulin-peptide complex." Nat Struct Biol **7**(1): 72-7.

Lee, K. H., S. Lee, B. Kim, S. Chang, S. W. Kim, J. S. Paick and K. Rhee (2006). "Dazl can bind to dynein motor complex and may play a role in transport of specific mRNAs." Embo Journal **25**(18): 4263-4270.

Leslie, A. (1992). "Mosflm 7.0.1 and its new interface - iMosflm 0.5.3." Joint CCP4+ESF-EAMCB Newsletter on Protein Crystallography **6**.

Leung, D. H., R. G. Bergman and K. N. Raymond (2008). "Enthalpy-entropy compensation reveals solvent reorganization as a driving force for supramolecular encapsulation in water." JACS **130**(9): 2798-805.

Li, M., M. Serr, E. A. Newman and T. S. Hays (2004). "The Drosophila tctex-1 light chain is dispensable for essential cytoplasmic dynein functions but is required during spermatid differentiation." Molecular Biology of the Cell **15**: 3005-14.

Liang, J., S. R. Jaffrey, W. Guo, S. H. Snyder and J. Clardy (1999). "Structure of the PIN/LC8 dimer with a bound peptide." Nat Struct Biol **6**(8): 735-40.

Lightcap, C. M., S. Sun, J. D. Lear, U. Rodeck, T. Polenova and J. C. Williams (2008). "Biochemical and structural characterization of the Pak1-LC8 interaction." JBC **283**(40): 27314-24.

Ligon, L. A., S. Karki, M. Tokito and E. L. F. Holzbaur (2001). "Dynein binds to beta-catenin and may tether microtubules at adherens junctions." Nature Cell Biology **3**(10): 913-917.

Lipari, G., Szabo A. (1982). "Model-Free Approach to the Interpretation of Nuclear Magnetic Resonance Relaxation in Macromolecules. 1. Theory and Range of Validity." JACS **104**: 4546.

Liu, J. F., Z. X. Wang, X. Q. Wang, Q. Tang, X. M. An, L. L. Gui and D. C. Liang (2006). "Crystal structure of human dynein light chain Dnlc2A: structural insights into the interaction with IC74." Biochem Biophys Res Commun **349**(3): 1125-9.

Lo, K. W., H. M. Kan, L. N. Chan, W. G. Xu, K. P. Wang, Z. Wu, M. Sheng and M. Zhang (2005). "The 8-kDa dynein light chain binds to p53-binding protein 1 and mediates DNA damage-induced p53 nuclear accumulation." JBC **280**(9): 8172-9.

Lo, K. W. H., H. M. Kan and K. K. Pfister (2006). "Identification of a novel region of the cytoplasmic dynein intermediate chain important for dimerization in the absence of the light chains." JBC **281**(14): 9552-9559.

Lo, K. W. H., S. Naisbitt, J. S. Fan, M. Sheng and M. J. Zhang (2001). "The 8-kDa dynein light chain binds to its targets via a conserved (K/R)XTQT motif." JBC **276**(17): 14059-14066.

Lovell, S. C., I. W. Davis, W. B. Arendall, 3rd, P. I. de Bakker, J. M. Word, M. G. Prisant, J. S. Richardson and D. C. Richardson (2003). "Structure validation by Calpha geometry: phi,psi and Cbeta deviation." Proteins **50**(3): 437-50.

Lukashok, S. A., L. Tarassishin, Y. G. Li and M. S. Horwitz (2000). "An adenovirus inhibitor of tumor necrosis factor alpha-induced apoptosis complexes with dynein and a small GTPase." Journal of Virology **74**(10): 4705-4709.

Ma, S., L. Trivinos-Lagos, R. Graf and R. L. Chisholm (1999). "Dynein intermediate chain mediated dynein-dynactin interaction is required for interphase microtubule organization and centrosome replication and separation in Dictyostelium." JCB **147**(6): 1261-1273.

Machado, R. D., N. Rudarakachana, C. Atkinson, J. A. Flanagan, R. Harrison, N. W. Morrel and R. C. Trembath (2003). "Functional interaction between BMPR-II and Tctex-1, a light chain of Dynein, is isoform-specific and disrupted by mutations underlying primary pulmonary hypertension." Human Molecular Genetics **12**(24): 3277-86.

Makokha, M., M. Hare, M. G. Li, T. Hays and E. Barbar (2002). "Interactions of cytoplasmic dynein light chains Tctex-1 and LC8 with the intermediate chain IC74." Biochemistry **41**(13): 4302-4311.

Makokha, M., Y. J. Huang, G. Montelione, A. S. Edison and E. Barbar (2004). "The Solution Structure of the pH Induced Monomer of Dynein Light Chain from Drosophila." Protein Science **13**: 727-734.

Mammen, M., Choi, S., Whitesides, G. M. (1998). "Polyvalent Interactions in Biological Systems: Implications for Design and Use of Multivalent Ligands and Inhibitors." Angew Chem Int Ed Engl **37**(20): 2754-2794.

Mandel, A. M., M. Akke and A. G. Palmer, 3rd (1995). "Backbone dynamics of Escherichia coli ribonuclease HI: correlations with structure and function in an active enzyme." JMB **246**(1): 144-63.

McCoy, A. J. (2007). "Solving structures of protein complexes by molecular replacement with Phaser." Acta Crystallogr D Biol Crystallogr **63**(Pt 1): 32-41.

Mische, S., M. Li, M. Serr and T. S. Hays (2007). "Direct observation of regulated ribonucleoprotein transport across the nurse cell/oocyte boundary." Mol Biol Cell **18**(6): 2254-63.

Mohan, P. M., M. Barve, A. Chatterjee and R. V. Hosur (2006). "pH driven conformational dynamics and dimer-to-monomer transition in DLC8." Protein Sci **15**(2): 335-42.

Mohan, P. M. and R. V. Hosur (2008). "NMR characterization of structural and dynamics perturbations due to a single point mutation in Drosophila DLC8 dimer: functional implications." Biochemistry **47**(23): 6251-9.

Mossessova, E. and C. D. Lima (2000). "Ulp1-SUMO crystal structure and genetic analysis reveal conserved interactions and a regulatory element essential for cell growth in yeast." Mol Cell **5**(5): 865-76.

Mueller, S., X. M. Cao, R. Welker and E. Wimmer (2002). "Interaction of the poliovirus receptor CD155 with the dynein light chain Tctex-1 and its implication for poliovirus pathogenesis." JBC **277**(10): 7897-7904.

Murray, C. W. and M. L. Verdonk (2002). "The consequences of translational and rotational entropy lost by small molecules on binding to proteins." J Comput Aided Mol Des **16**(10): 741-53.

Murshudov, G. N., A. A. Vagin and E. J. Dodson (1997). "Refinement of macromolecular structures by the maximum-likelihood method." Acta Crystallogr D Biol Crystallogr **53**(Pt 3): 240-55.

Nadano, D., J. Nakayama, S. Matsuzawa, T. A. Sato, T. Matsuda and M. N. Fukuda (2002). "Human tastin, a proline-rich cytoplasmic protein, associates with the microtubular cytoskeleton." Biochem J **364**(Pt 3): 669-77.

Nagano, F., S. Orita, T. Sasaki, A. Naito, G. Sakaguchi, M. Maeda, T. Watanabe, E. Kominami, Y. Uchiyama and Y. Takai (1998). "Interaction of Doc2 with tctex-1, a light chain of cytoplasmic dynein - Implication in dynein-dependent vesicle transport." JBC **273**(46): 30065.

Navarro, C., H. Puthalakath, J. M. Adams, A. Strasser and R. Lehmann (2004). "Egalitarian binds dynein light chain to establish oocyte polarity and maintain oocyte fate." Nat Cell Biol **6**(5): 427-35.

Nikulina, K., R. S. Patel-King, S. Takebe, K. K. Pfister and S. M. King (2004). "The Roadblock light chains are ubiquitous components of cytoplasmic dynein that form homo- and heterodimers." Cell Motil Cytoskeleton **57**(4): 233-45.

Nurminsky, D. I., M. V. Nurminskaya, E. V. Benevolenskaya, Y. Y. Shevelyov, D. L. Hartl and V. A. Gvozdev (1998). "Cytoplasmic dynein intermediate-chain isoforms with different targeting properties created by tissue-specific alternative splicing." Molecular and Cellular Biology **18**(11): 6816-6825.

Nyarko, A., L. Cochrun, S. Norwood, N. Pursifull, A. Voth and E. Barbar (2005). "Ionization of His 55 at the Dimer Interface of Dynein Light-Chain LC8 Is Coupled to Dimer Dissociation." Biochemistry **44**(43): 14248-55.

Nyarko, A., M. Hare, T. S. Hays and E. Barbar (2004). "The intermediate chain of cytoplasmic dynein is partially disordered and gains structure upon binding to light-chain LC8." Biochemistry **43**(49): 15595-603.

Okamura, S. M., C. E. Oki-Idouchi and P. S. Lorenzo (2006). "The exchange factor and diacylglycerol receptor RasGRP3 interacts with dynein light chain 1 through its C-terminal domain." JBC **281**(47): 36132-9.

Page, M. I. and W. P. Jencks (1971). "Entropic contributions to rate accelerations in enzymic and intramolecular reactions and the chelate effect." PNAS USA **68**(8): 1678-83.

Pappu, R. V. and G. D. Rose (2002). "A simple model for polyproline II structure in unfolded states of alanine-based peptides." Protein Sci **11**(10): 2437-55.

Pazour, G. J. and G. B. Witman (2000). "Forward and reverse genetic analysis of microtubule motors in Chlamydomonas." Methods-a Companion to Methods in Enzymology **22**(4): 285-298.

Persson, B. D., S. Muller, D. M. Reiter, B. B. Schmitt, M. Marttila, C. V. Sumowski, S. Schweizer, U. Scheu, C. Ochsenfeld, N. Arnberg and T. Stehle (2009). "An arginine switch in the species B adenovirus knob determines high-affinity engagement of cellular receptor CD46." J Virol **83**(2): 673-86.

Pfarr, C. M., M. Coue, P. M. Grissom, T. S. Hays, M. E. Porter and J. R. McIntosh (1990). "Cytoplasmic Dynein Is Localized to Kinetochores During Mitosis." Nature **345**(6272): 263-265.

Pfister, K. K., E. M. Fisher, I. R. Gibbons, T. S. Hays, E. L. Holzbaur, J. R. McIntosh, M. E. Porter, T. A. Schroer, K. T. Vaughan, G. B. Witman, S. M. King and R. B. Vallee (2005). "Cytoplasmic dynein nomenclature." JCB **171**(3): 411-3.

Pfister, K. K., B. E. Haley and G. B. Witman (1984). "The photoaffinity probe 8-azidoadenosine 5'-triphosphate selectively labels the heavy chain of Chlamydomonas 12 S dynein." JBC **259**(13): 8499-504.

Pfister, K. K., P. R. Shah, H. Hummerich, A. Russ, J. Cotton, A. A. Annuar, S. M. King and E. M. Fisher (2006). "Genetic analysis of the cytoplasmic dynein subunit families." PLoS Genet **2**(1): e1.

Phillis, R., D. Statton, P. Caruccio and R. K. Murphey (1996). "Mutations in the 8 kDa dynein light chain gene disrupt sensory axon projections in the Drosophila imaginal CNS." Development **122**(10): 2955-2963.

Poisson, N., E. Real, Y. Gaudin, M. C. Vaney, S. King, Y. Jacob, N. Tordo and D. Blondel (2001). "Molecular basis for the interaction between rabies virus phosphoprotein P and the dynein light chain LC8: dissociation of dynein-binding properties and transcriptional functionality of P." J Gen Virol **82**(Pt 11): 2691-6.

Popovych, N., S. Sun, R. H. Ebright and C. G. Kalodimos (2006). "Dynamically driven protein allostery." Nat Struct Mol Biol **13**(9): 831-8.

Puthalakath, H., D. C. S. Huang, L. A. O'Reilly, S. M. King and A. Strasser (1999). "The proapoptotic activity of the Bcl-2 family member Bim is regulated by interaction with the dynein motor complex." Molecular Cell **3**(3): 287-296.

Reuter, J. E., T. M. Nardine, A. Penton, P. Billuart, E. K. Scott, T. Usui, T. Uemura and L. Luo (2003). "A mosaic genetic screen for genes necessary for Drosophila mushroom body neuronal morphogenesis." Development **130**(6): 1203-13.

Rodriguez-Crespo, I., B. Yelamos, F. Roncal, J. P. Albar, P. R. Ortiz de Montellano and F. Gavilanes (2001). "Identification of novel cellular proteins that bind to the LC8 dynein light chain using a pepscan technique." FEBS Lett **503**(2-3): 135-41.

Sachdev, P., S. Menon, D. B. Kastner, J. Z. Chuang, T. Y. Yeh, C. Conde, A. Caceres, C. H. Sung and T. P. Sakmar (2007). "G protein betagamma subunit interaction with the dynein light-chain component Tctex-1 regulates neurite outgrowth." Embo J **26**(11): 2621-32.

Sale, W. S. and P. Satir (1977). "Direction of active sliding of microtubules in Tetrahymena cilia." PNAS USA **74**(5): 2045-9.

Santoro, M. M. and D. W. Bolen (1988). "Unfolding free energy changes determined by the linear extrapolation method. 1. Unfolding of phenylmethanesulfonyl alpha-chymotrypsin using different denaturants." Biochemistry **27**(21): 8063-8.

Sarma, G. N., S. N. Savvides, K. Becker, M. Schirmer, R. H. Schirmer and P. A. Karplus (2003). "Glutathione reductase of the malarial parasite Plasmodium falciparum: crystal structure and inhibitor development."JMB **328**(4): 893-907.

Schlunegger, M. P., M. J. Bennett and D. Eisenberg (1997). "Oligomer formation by 3D domain swapping: a model for protein assembly and misassembly." Adv Protein Chem **50**: 61-122.

Schnorrer, F., K. Bohmann and C. Nusslein-Volhard (2000). "The molecular motor dynein is involved in targeting Swallow and bicoid RNA to the anterior pole of Drosophila oocytes." Nature Cell Biology **2**(4): 185-190.

Schwarzer, C., S. Barnikol-Watanabe, F. P. Thinnes and N. Hilschmann (2002). "Voltage-dependent anion-selective channel (VDAC) interacts with the dynein light chain Tctex1 and the heat-shock protein PBP74." Int J Biochem Cell Biol **34**(9): 1059-70.

Soetens, J., Millot, C., Chipot, C., Jansen, G., Ángyán, J., Maigre, B. (1997). "Jean-Christophe Soetens,†‡ Claude Millot,*† Christophe Chipot,† Georg Jansen,‡ János G. Ángyán,† and Bernard Maigre." The Journal of Physical Chemistry, B. **101**: 10910-10917.

Song, C., W. Wen, S. K. Rayala, M. Chen, J. Ma, M. Zhang and R. Kumar (2008). "Serine 88 Phosphorylation of the 8-kDa Dynein Light Chain 1 Is a Molecular Switch for Its Dimerization Status and Functions." JBC **283**(7): 4004-13.

Song, J., R. C. Tyler, M. S. Lee, E. M. Tyler and J. L. Markley (2005). "Solution structure of isoform 1 of Roadblock/LC7, a light chain in the dynein complex." JMB **354**(5): 1043-51.

Song, Y., G. Benison, A. Nyarko, T. S. Hays and E. Barbar (2007). "Potential role for phosphorylation in differential regulation of the assembly of dynein light chains." JBC **282**(23): 17272-9.

Spolar, R. S. and M. T. Record (1994). "Coupling of Local Folding to Site-Specific Binding of Proteins to Dna." Science **263**(5148): 777-784.

Steffen, W., S. Karki, K. T. Vaughan, R. B. Vallee, E. L. F. Holzbaur, D. G. Weiss and S. A. Kuznetsov (1997). "The involvement of the intermediate chain of cytoplasmic dynein in binding the motor complex to membranous

organelles of Xenopus oocytes." Molecular Biology Of the Cell **8**(10): 2077.

Stelter, P., R. Kunze, D. Flemming, D. Hopfner, M. Diepholz, P. Philippsen, B. Bottcher and E. Hurt (2007). "Molecular basis for the functional interaction of dynein light chain with the nuclear-pore complex." Nat Cell Biol **9**(7): 788-96.

Stokin, G. B. and L. S. Goldstein (2006). "Axonal transport and Alzheimer's disease." Annu Rev Biochem **75**: 607-627.

Strong, M., M. R. Sawaya, S. Wang, M. Phillips, D. Cascio and D. Eisenberg (2006). "Toward the structural genomics of complexes: crystal structure of a PE/PPE protein complex from Mycobacterium tuberculosis." PNAS USA **103**(21): 8060-5.

Sugai, M., M. Saito, I. Sukegawa, Y. Katsushima, Y. Kinouchi, N. Nakahata, T. Shimosegawa, T. Yanagisawa and J. Sukegawa (2003). "PTH/PTH-related protein receptor interacts directly with Tctex-1 through its COOH terminus." Biochemical and Biophysical Research Communications **311**(1): 24-31.

Susalka, S. J., K. Nikulina, M. W. Salata, P. S. Vaughan, S. M. King, K. T. Vaughan and K. K. Pfister (2002). "The roadblock light chain binds a novel region of the cytoplasmic dynein intermediate chain." JBC **277**(36): 32939-32946.

Susalka, S. J. and K. K. Pfister (2000). "Cytoplasmic dynein subunit heterogeneity: implications for axonal transport." Journal of Neurocytology **29**(11-12): 819-829.

Talbott, M., M. Hare, A. Nyarko, T. S. Hays and E. Barbar (2006). "Folding is coupled to dimerization of Tctex-1 dynein light chain." Biochemistry **45**(22): 6793-800.

Tan, G. S., M. A. Preuss, J. C. Williams and M. J. Schnell (2007). "The dynein light chain 8 binding motif of rabies virus phosphoprotein promotes efficient viral transcription." PNAS USA **104**(17): 7229-34.

Tang, Q., C. M. Staub, G. F. Gao, Q. Y. Jin, Z. K. Wang, W. Ding, R. E. Aurigemma and K. M. Mulder (2002). "A novel transforming growth factor-beta receptor-interacting protein that is also a light chain of the motor protein dynein." Biochemistry **13**(12): 4484-4496.

Tjandra N., F. S. E., Pastor R. W., Bax A. (1995). "Rotational Diffusion Anisotropy of Human Ubiquitin from 15NNMR Relaxation."JACS **11**: 12562-12566.

Toke, O., J. D. Monsey, G. T. DeKoster, G. P. Tochtrop, C. Tang and D. P. Cistola (2006). "Determinants of cooperativity and site selectivity in human ileal bile acid binding protein." Biochemistry **45**(3): 727-37.

Tsodikov, O. V., M. T. Record, Jr. and Y. V. Sergeev (2002). "Novel computer program for fast exact calculation of accessible and molecular surface areas and average surface curvature." J Comput Chem **23**(6): 600-9.

Turnbull, W. B. and A. H. Daranas (2003). "On the value of c: can low affinity systems be studied by isothermal titration calorimetry?" JACS **125**(48): 14859-66.

Vadlamudi, R. K., R. Bagheri-Yarmand, Z. Yang, S. Balasenthil, D. Nguyen, A. A. Sahin, P. den Hollander and R. Kumar (2004). "Dynein light chain 1, a p21-activated kinase 1-interacting substrate, promotes cancerous phenotypes." Cancer Cell **5**(6): 575-85.

Vallee, R. B., J. C. Williams, D. Varma and L. E. Barnhart (2004). "Dynein: An ancient motor protein involved in multiple modes of transport." **58**(2): 189-200.

Varma, D., A. Dawn, A. Ghosh-Roy, S. J. Weil, K. M. Ori-McKenney, Y. Zhao, J. Keen, R. B. Vallee and J. C. Williams (2010). "Development and application of in vivo molecular traps reveals that dynein light chain occupancy differentially affects dynein-mediated processes." PNAS USA **107**(8): 3493-8.

Vaughan, K. T. and R. B. Vallee (1995). "Cytoplasmic dynein binds dynactin through a direct interaction between the intermediate chains and pl50(glued)." JCB **131**: 1507-1516.

Vaughan, P. S., J. D. Leszyk and K. T. Vaughan (2001). "Cytoplasmic dynein intermediate chain phosphorylation regulates binding to dynactin." JBC **276**(28): 26171-9.

Wang, L., M. Hare, T. S. Hays and E. Barbar (2004). "Dynein light chain LC8 promotes assembly of the coiled-coil domain of swallow protein." Biochemistry **43**(15): 4611-20.

Wang, W., K. W. Lo, H. M. Kan, J. S. Fan and M. Zhang (2003). "Structure of the monomeric 8-kDa dynein light chain and mechanism of the domain-swapped dimer assembly." JBC **278**(42): 41491-9.

Wanschers, B., R. van de Vorstenbosch, M. Wijers, B. Wieringa, S. M. King and J. Fransen (2008). "Rab6 family proteins interact with the dynein light chain protein DYNLRB1." Cell Motil Cytoskeleton **65**(3): 183-96.

Wickstead, B. and K. Gull (2007). "Dyneins across eukaryotes: a comparative genomic analysis." Traffic **8**(12): 1708-21.

Wilkerson, C. G., S. M. King, A. Koutoulis, G. J. Pazour and G. B. Witman (1995). "The 78,000 M(R) Intermediate Chain of Chlamydomonas Outer Arm Dynein Is a Wd-Repeat Protein Required for Arm Assembly."JCB **129**(1): 169-178.

Wilkins, M. R., E. Gasteiger, A. Bairoch, J. C. Sanchez, K. L. Williams, R. D. Appel and D. F. Hochstrasser (1999). "Protein identification and analysis tools in the ExPASy server." Methods Mol Biol **112**: 531-52.

Williams, J. C., P. L. Roulhac, A. G. Roy, R. B. Vallee, M. C. Fitzgerald and W. A. Hendrickson (2007). "Structural and thermodynamic characterization of a cytoplasmic dynein light chain-intermediate chain complex." PNAS USA **104**(24): 10028-33.

Williams, J. C., H. Xie and W. A. Hendrickson (2005). "Crystal structure of dynein light chain TCTEX-1." JBC **280**(23): 21981-6.

Wishart, D. S., C. G. Bigam, J. Yao, F. Abildgaard, H. J. Dyson, E. Oldfield, J. L. Markley and B. D. Sykes (1995). "1H, 13C and 15N chemical shift referencing in biomolecular NMR." J Biomol NMR **6**(2): 135-40.

Wishart, D. S., B. D. Sykes and F. M. Richards (1992). "The chemical shift index: a fast and simple method for the assignment of protein secondary structure through NMR spectroscopy." Biochemistry **31**(6): 1647-51.

Yang, Z., U. S. Tulu, P. Wadsworth and C. L. Rieder (2007). "Kinetochore dynein is required for chromosome motion and congression independent of the spindle checkpoint." Curr Biol **17**(11): 973-80.

Yano, H., F. S. Lee, H. Kong, J. Z. Chuang, J. C. Arevalo, P. Perez, C. H. Sung and M. V. Chao (2001). "Association of Trk neurotrophin receptors with components of the cytoplasmic dynein motor." Journal of Neuroscience **21**(3): U7-U13.

Ye, G. J., K. T. Vaughan, R. B. Vallee and B. Roizman (2000). "The herpes simplex virus 1 U(L)34 protein interacts with a cytoplasmic dynein intermediate chain and targets nuclear membrane." Journal of Virology **74**(3): 1355-1363.

Yeh, T. Y., J. Z. Chuang and C. H. Sung (2005). "Dynein light chain rp3 acts as a nuclear matrix-associated transcriptional modulator in a dynein-independent pathway." J Cell Sci **118**(Pt 15): 3431-43.

Yeh, T. Y., D. Peretti, J. Z. Chuang, E. Rodriguez-Boulan and C. H. Sung (2006). "Regulatory dissociation of Tctex-1 light chain from dynein complex is essential for the apical delivery of rhodopsin." Traffic **7**(11): 1495-502.

Zhang, J., S. Li, S. Musa, H. Zhou and X. Xiang (2009). "Dynein light intermediate chain in Aspergillus nidulans is essential for the interaction between heavy and intermediate chains." JBC **284**(50): 34760-8.

Zuccarello, D., A. Ferlin, C. Cazzadore, A. Pepe, A. Garolla, A. Moretti, G. Cordeschi, S. Francavilla and C. Foresta (2008). "Mutations in dynein genes in patients affected by isolated non-syndromic asthenozoospermia." Hum Reprod **23**(8): 1957-62.

Appendices

Appendix 1

Multivalency in the assembly of intrinsically disordered dynein intermediate chain - supplemental information

Justin Hall, P. Andrew Karplus and Elisar Barbar

Published in *Journal of Biological Chemistry*,
2008, 284 (48), 33115-33121

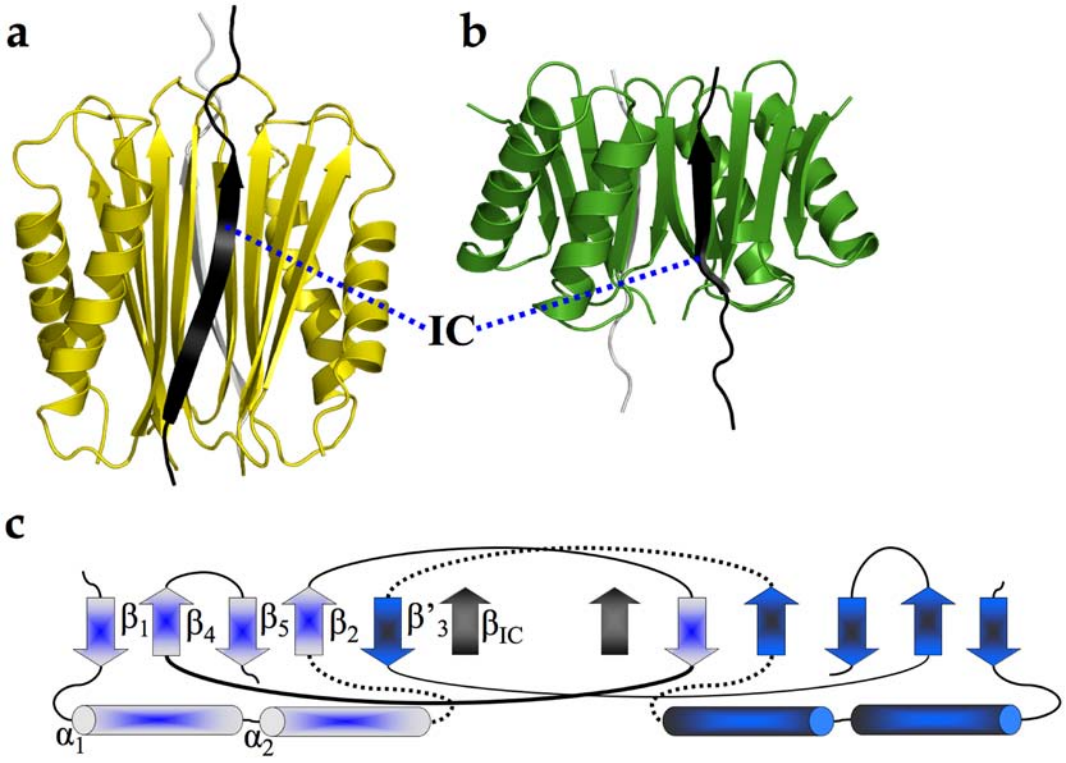

Figure A1.1: Tctex1 and LC8 are homologs which bind IC in a similar way and share a common fold. Secondary structural elements of a) the Tctex1 dimer (yellow) and b) the LC8 dimer (green) with IC segments (black and grey). c) The topology of Tctex1 and LC8 dimers showing the crossover β-strand at the dimer interface (β'_3). The Tctex1 fold does not contain a strand β_1. The two subunits of the homodimer are light and dark blue, and the strands of bound IC (β_{IC}) are charcoal. Panels a and b were generated using Pymol (DeLano 2002), pdb code 3FM7.

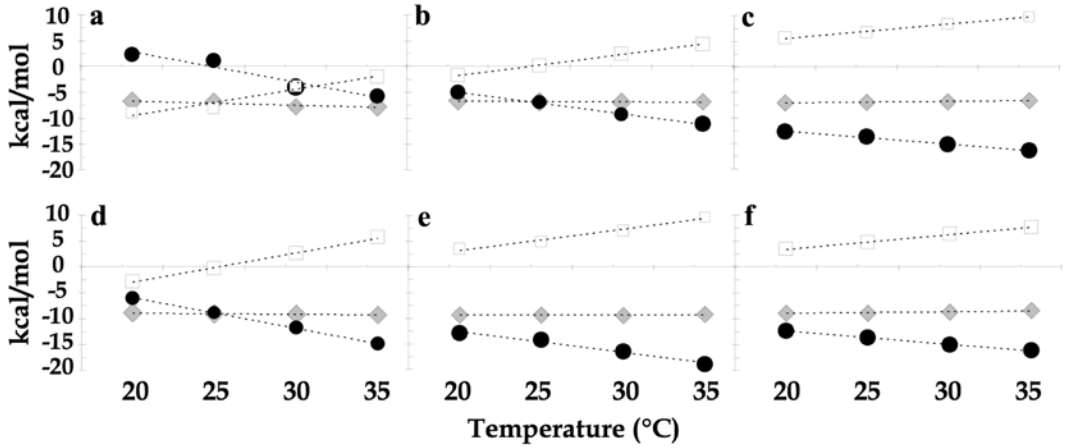

Figure A1.2: Plots of thermodynamics association parameters (ΔG°, grey diamonds; ΔH°, black circles; and -TΔS°, white squares) versus temperature. a) LC8 binding to IC_L; b) Tctex1 binding to apo-IC_{TL}; c) LC8 binding to apo-IC_{TL}; d) Tctex1 binding to pre-bound IC_{TL}; e) LC8 binding to pre-bound IC_{TL}; f) LC8 binding to IC_{LL}. Thermodynamic association parameters for IC_L at 30 and 35 °C were reported previously by Hall *et al.* (Hall et al. 2008).

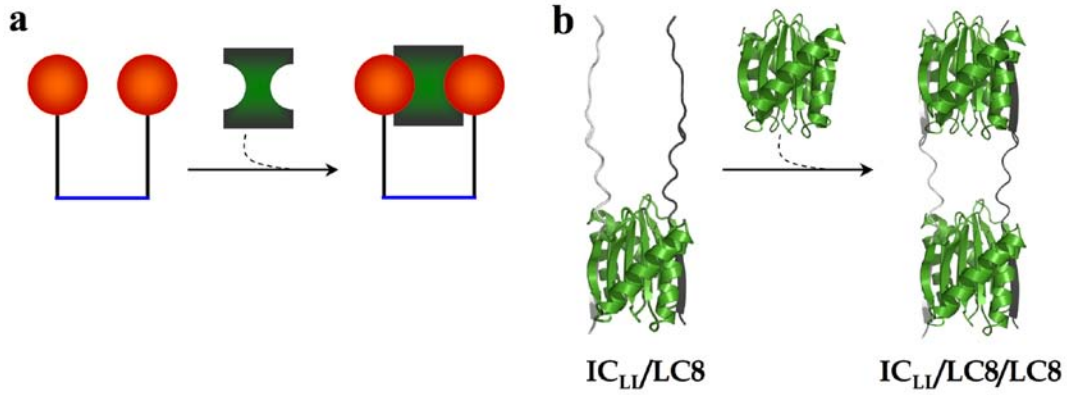

Figure A1.3: Pre-bound IC as a bivalent ligand. a) Diagram of a generic bivalent ligand (left), with two binding sites (orange spheres) connected by a flexible linker (blue), binds to a green molecule (over arrow) with dual symmetric binding sites. b) Illustrative example of IC_{LL} (black and white chains) pre-bound to LC8 (green). Here the IC_{LL}•LC8 complex forms a bivalent IC duplex presenting equivalent ends for binding another LC8 molecule. Equivalent illustrations could be prepared for IC_{TL} pre-bound to Tctex1 or LC8. Panel b figures generated using Pymol (DeLano 2002), pdb code 3GLW.

Table A1.1: IC sequence similarity in model organisms for the region binding Tctex1 and LC8.

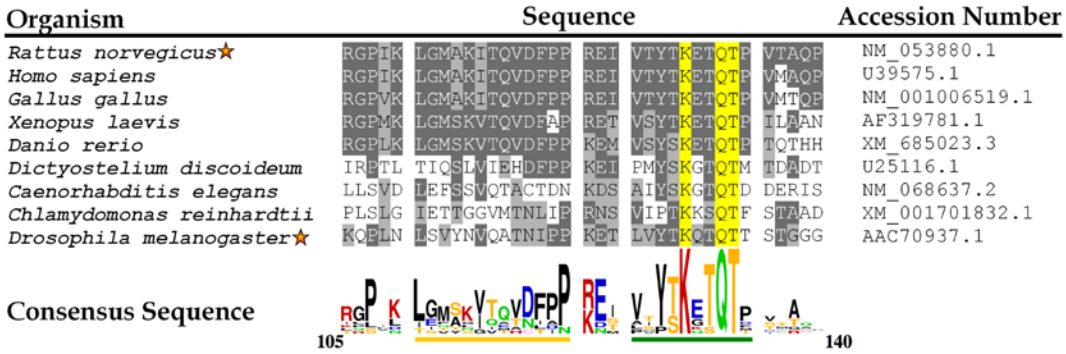

A 36 residue segment of IC from nine model organisms is shown along with a consensus sequence prepared by WebLogo (Crooks *et al.* 2004) (*D. melanogaster* numbering). For clarity the Tctex1 (gold bar) and LC8 (green bar) binding segments are separated by a space from adjacent residues. The most frequently occurring residue (dark grey background), residues similar to the most frequently occurring residue (light grey background), and globally conserved residues (yellow background) are indicated. The core LC8 binding residues are highly similar between species, with the three residue linker segment being the next highest similar region with an R/K-E-I/S/T pattern. In contrast, aside from the vertebrate sequences, the core Tctex1 binding residues have lower sequence similarity; the most similar residues are the first, the fifth and the last four residues (L, V and NIPP in *D. melanogaster*, respectively). Interestingly, despite the lower sequence similarity of the putative Tctex1 binding sites, the difference between any two IC sequences is no greater than the difference between *R. norvegicus* and *D. melanogaster* sequences (stars), and structures determined for *D. melanogaster* Tctex1 binding IC from both *R. norvegicus* and *D. melanogaster* prove recognition occurs despite poor sequence similarity. These results indicate that IC•Tctex1 recognition has a higher plasticity than IC•LC8 recognition, and the level of sequence similarity of the last four residues which bind Tctex1 and the three residue linker support the conclusion that the Tctex1 site is conserved among these organisms.

Table A1.2: Data collection and refinement statistics, values in parentheses are for the highest resolution shell.

Data	IC/Tctex1/LC8	IC_{LL}/LC8/LC8
Resolution (Å)	37.9 - 3.5 (3.59 - 3.5)	38.66 - 3.15 (3.23 - 3.15)
Completeness (%)	99.9 (99.9)	100 (99.9)
R_{meas}	0.10 (0.35)	0.10 (0.41)
Total Reflections	257,493	69,639
Unique Reflections	8,803	2,695
Refinement		
Resolution (Å)	37.9 - 3.5 (3.59 - 3.5)	38.66 - 3.15 (3.23 - 3.15)
No. Reflections Used	8,803 (1,267)	2,520 (362)
Rcryst (%)	17.0 (26.5)	20.3 (26.3)
Rfree (%)	27.5 (28.1)	27.1 (30.1)
Average B-factor (all atoms) ($Å^2$)	67.1	22.3
RMSD from ideal:		
Bond length (Å)	0.01	0.01
Bond angles (°)	0.06	0.05
ϕ, φ outliers (%) [a]	6.4	4.2
ϕ, φ most favored (%) [a]	93.6	95.8

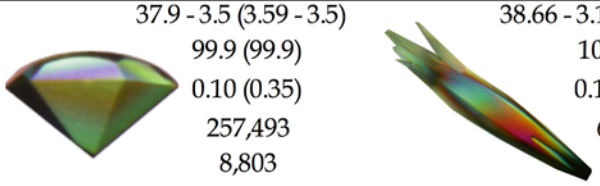

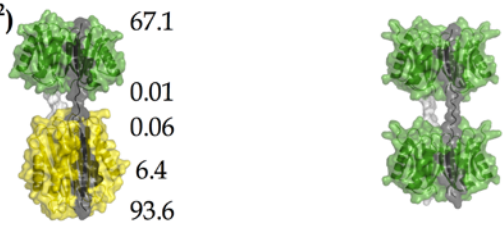

[a]As defined by Lovell, S. C., *et al*. (Lovell et al. 2003)

Appendix 2

The crystal structure of dynein intermediate chain•light chain roadblock complex gives new insights into dynein assembly – supplemental information

Justin Hall, Yujuan Song, P. Andrew Karplus and Elisar Barbar

Published in *Journal of Biological Chemistry*,
In press

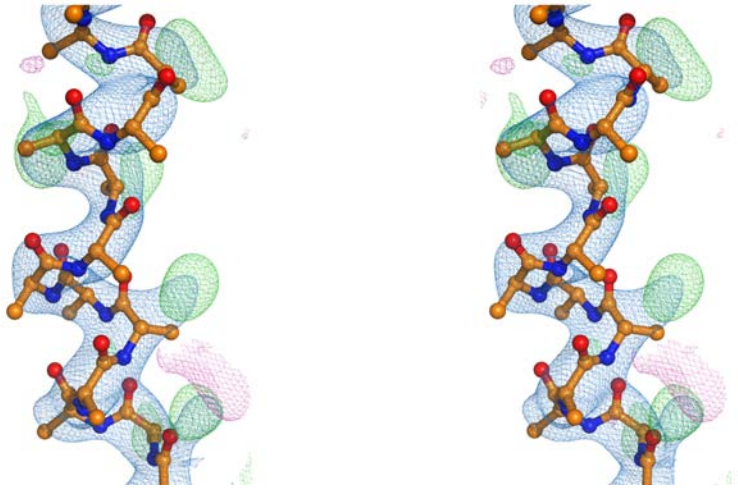

Figure A2.1: Electron density does not support an α_{IC2} directionality antiparallel to α_1 of LC7. 2Fo-Fc and Fo-Fc maps calculated after inclusion in the refinement of a 19 residue poly-Ala helix (carbon, oxygen and nitrogen atoms are colored orange, red and blue, respectively) modeled into the strong helical density seen in Figure 5.3a with an N-to-C directionality antiparallel to α_1 of LC7. 2Fo-Fc density is contoured at 2σ (blue), Fo-Fc density is contoured at 3σ (green) and -3σ (magenta). The backbone model fit in this direction agrees much more poorly with the density than the helix modeled in the other direction (see Fig. 5.3b). For example, in some residues the carbonyl oxygen, rather than the Cα, point into the missing side-chain density. No residue positions are labeled in this figure, as there is no correct sequence for a chain modeled in this direction.

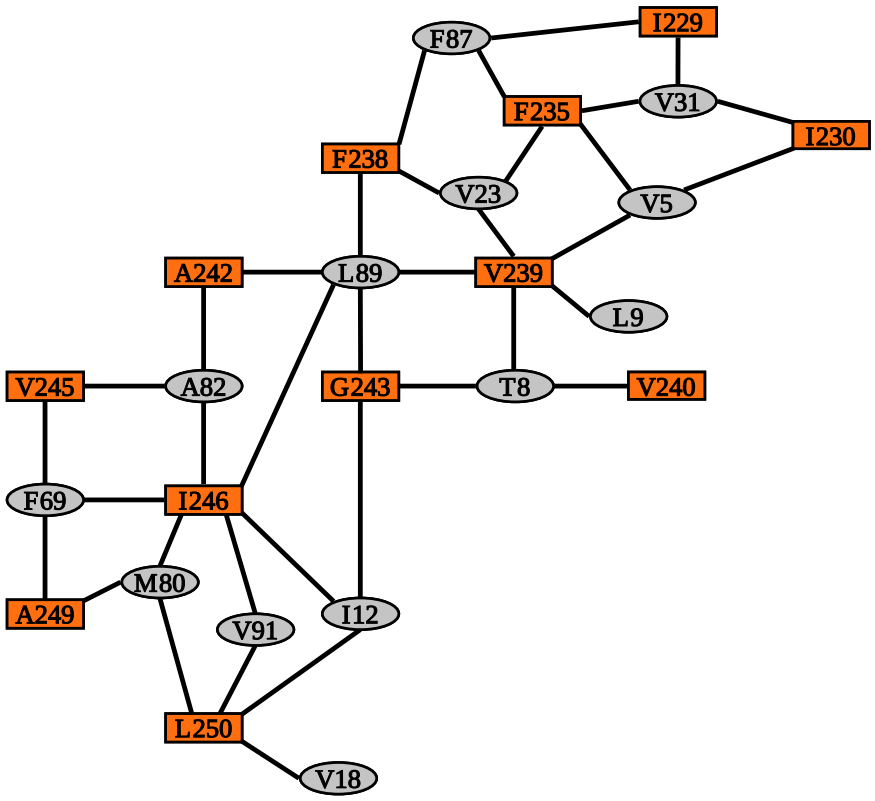

Figure A2.1: The nonpolar packing network at the IC•LC7 interface. Nonpolar side chains of IC (orange) and LC7 (grey) that have greater than 5 $Å^2$ of surface area buried at the interface are shown. Interactions between IC and LC7 side chains in the large contiguous nonpolar network as viewed in Figure 5.2d are indicated with black lines.

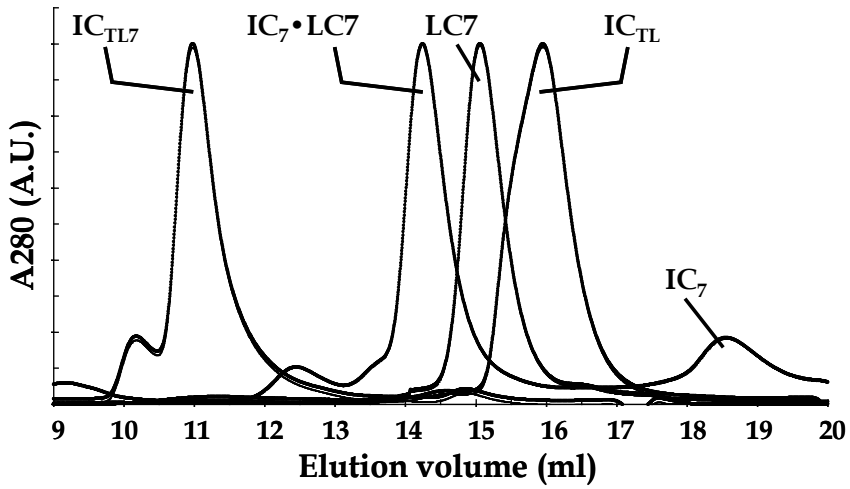

Figure A2.3: Representative gel filtration data for LC7 and IC constructs at 25 °C. Elution profile for IC constructs corresponding to residues 84-143 (IC_{TL}) (Benison et al. 2006; Hall et al. 2009), 92-260 (IC_{TL7}), 212-260 (IC_7), LC7 and the IC_7•LC7 complex show IC_7 elutes after the similarly sized IC_{TL} which is monomeric. The protein component of each peak was verified by MALDI-TOF MS. Data collected in 200 mM sodium sulfate, 50 mM sodium phosphate, 1 mM sodium azide at pH 7.3 using an Superdex75 10/300 (GE Healthcare) with a void volume of 10 ml.

Figure A2.4: Sequence conservation of IC and LC7. a) Sequences of LC7 shown are from *D. melanogaster* (*Dm*) and LC7a and LC7b isoforms from *H. sapiens* (*Hs*), *R. norvegicus* (*Rn*), *G. gallus* (*Gg*), *X. (Silurana) tropicalis* (*Xt*) and *D. rerio* (*Dr*); LC7 secondary structure (above), residues burying more than 5 $Å^2$ of surface area when bound to IC (orange bar), amino acid differences between *Dm* and *Hs* LC7 (cyan background), the conserved sequence differences between LC7 paralogs (yellow background) and potential phosphorylation sites (Ding et al. 2005) (red background) are shown. b) Sequence comparison of the *Dm* IC isoform 2 with IC1 and IC2 isoforms from vertebrates; IC secondary structure when bound to LC7 (above), sequence coloring as in panel "a". Vertebrates contain two alternate LC7 recognition sequences while *Dm* contains ten IC isoforms which have identical LC7 recognition sequences. LC7 from *Dm* is 72 and 73% identical to *Hs* LC7a and LC7b, respectively; the LC7 recognition sequence of *Dm* IC_{2B} is 55 and 47% identical to the LC7 recognition sequence of *Hs* IC_1 and IC_2, respectively; *Hs* IC_1 and IC_2 are 73% identical to each other.

Figure A2.4: (*Continued*).

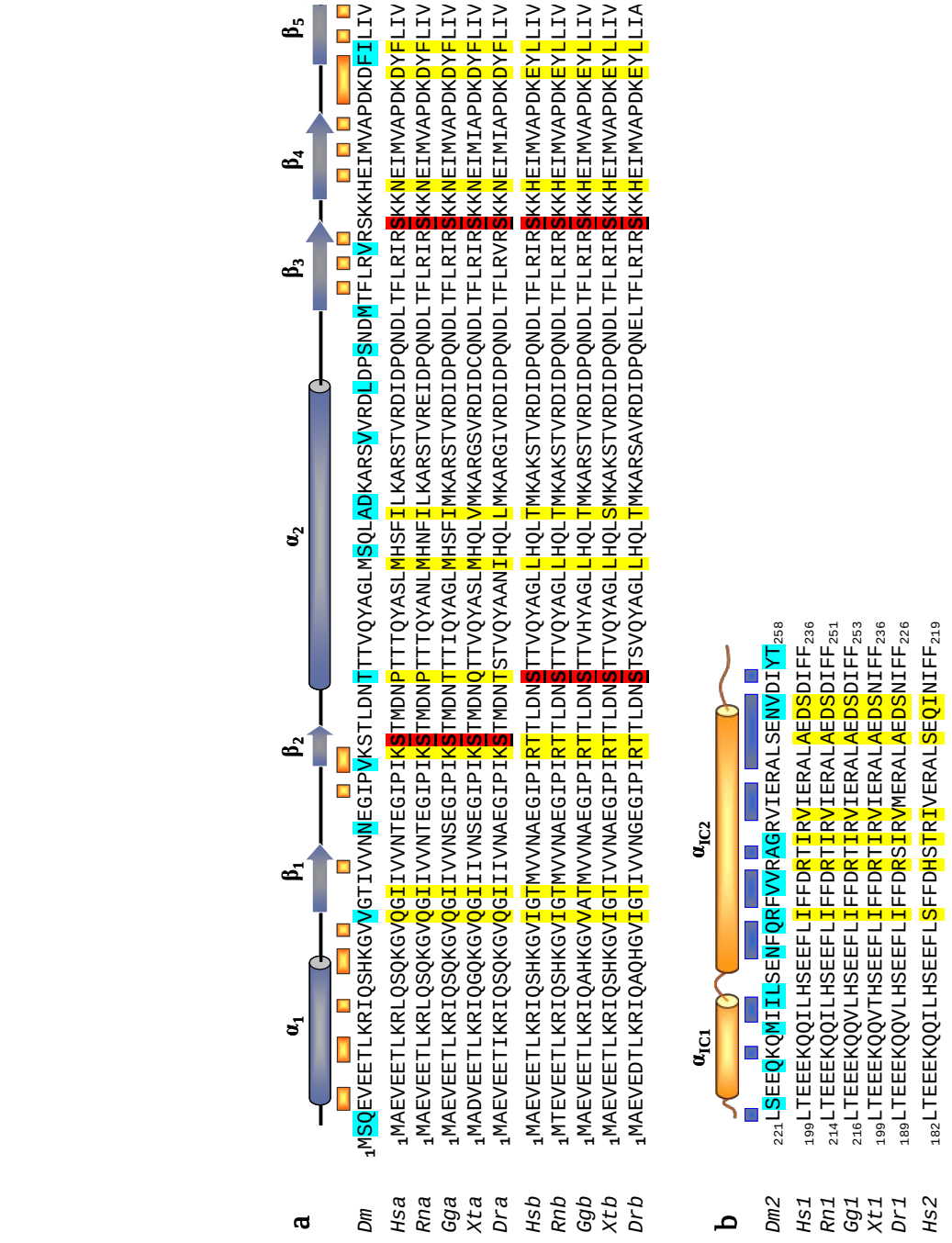

Figure A2.5: The predicted secondary structure of IC matches the structure it adopts when bound to light chains. The sequence of IC_{92-289} is shown above the predicted secondary structure elements from Jpred (Cole *et al.* 2008) (an arrow for a β-strand, a cylinder for an α-helix and dashed lines for disordered) and their confidence scores (with most confident predictions shown in red). Above the IC_{92-289} sequence are the secondary structures adopted by IC segments when bound to Tctex1 (residues 110-122, yellow), LC8 (residues 126-135, green) and LC7 (residues 221-258, blue).

Figure A2.5: (*Continued*)

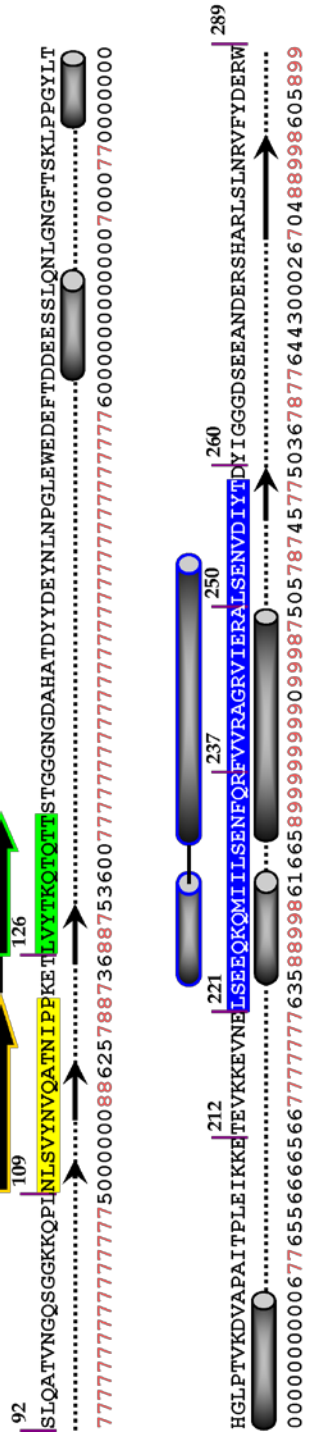

Table A2.1: Surface area buried in the IC•LC7 complex[a].

LC7		IC	
Residue	**ASA (Å^2)**	**Residue**	**ASA (Å^2)**
E4	41 (40)[b]	L221	47 (32)
V5	97 (94)	K226	65 (64)
T8	41 (41)	I229	42 (42)
L9	16 (16)	I230	53 (51)
I12	48 (46)	N234	48 (45)
H15	82 (82)	F235	61 (56)
K16	73 (71)	Q236	55 (54)
V18	4 (4)[a]	F238	113 (107)
V23	28 (28)	V239	73 (68)
I29	62 (62)	V240	55 (52)
V31	92 (69)	A242	32 (25)
K32	18 (18)	G243	21 (0)
F69	43 (43)	V245	60 (58)
R71	48 (47)	I246	90 (89)
R73	18 (18)	E247	66 (66)
E78	7 (7)	A249	46 (44)
M80	48 (48)	L250	97 (93)
A82	32 (29)	S251	5 (4)
D84	40 (38)	E252	21 (20)
K85	77 (77)	N253	114 (82)
D86	22 (22)	V254	77 (70)
F87	90 (87)	I256	52 (24)
L89	52 (49)		
V91	11 (11)		
Q93	37 (37)		
P95	8 (3)		
T96	63 (57)		

[a] Solvent accessible surface area for residues burying ≥ 5 Å^2, and V18, which is part of the large contiguous nonpolar network shown in Appendix Figure A2.2. Calculations performed using SURFACE RACER 5.0 (Tsodikov et al. 2002).
[b] Values in parenthesis are for side chains.

Appendix 3

Hydrogen/deuterium exchange rates for LC8, nNOS•LC8 and Swa•LC8 complexes

Justin Hall

Table A3.1: Hydrogen/deuterium exchange rates for LC8, nNOS•LC8 and Swa•LC8 in 50 mM NaPO4, 50 mM NaCl, 3% (v/v) glycerol, pH 6.7 at 30 °C.

2° Str.	Residue Number	Apo-LC8[a] PF ± Error	Nos•LC8b PF ± Error	Swa•LC8[c] PF ± Error
Loop	5	FAST[d]	FAST	FAST
Strand	6	FAST	5.0 ± 0.2	FAST
	7	FAST	4.4 ± 2.1	FAST
	8	4.3 ± 0.5	FAST	FAST
	9	FAST	3.7 ± 0.6	FAST
	10	3.9 ± 0.4	4.1 ± 0.3	FAST
Helix	16	4.0 ± 0.2	FAST	N.A.
	17	FAST	2.9 ± 0.3	FAST
	18	4.8 ± 0.1	6.2 ± 1.5	5.2 ± 2.7
	19	3.7 ± 0.1	5.7 ± 3.3	4.5 ± 0.2
	20	4.0 ± 0.1	6.3 ± 1.7	4.7 ± 0.1
	21	5.0 ± 0.5	6.0 ± 3.1	SLOW
	22	5.0 ± 1.8	3.9 ± 5.4	SLOW
	23	4.1 ± 0.2	4.8 ± 2.6	4.8 ± 0.2
	24	6.3 ± 2.1	5.7 ± 1.6	6.0 ± 0.3
	25	6.2 ± 4.9	SLOW	SLOW
	26	5.1 ± 0.5	SLOW	7.0 ± 0.5
	27	3.8 ± 0.6	5.5 ± 0.6	4.5 ± 0.2
	28	4.8 ± 1.1	5.6 ± 0.7	5.5 ± 0.4
	29	4.5 ± 0.2	5.3 ± 0.9	5.4 ± 0.4
	30	FAST	3.0 ± 0.2	FAST
	31	4.9 ± 0.2	3.9 ± 0.2	FAST
Loop	32	5.1 ± 0.4	4.9 ± 0.3	3.2 ± 0.9
	33	FAST	FAST	FAST
	34	FAST	3.1 ± 0.2	FAST
Helix	35	FAST	FAST	4.8 ± 0.3
	36	FAST	4.3 ± 0.3	FAST
	37	3.0 ± 0.3	5.2 ± 0.9	4.8 ± 0.2
	38	3.4 ± 0.2	SLOW	4.6 ± 1.0
	39	SLOW[e]	5.4 ± 1.6	SLOW
	40	5.1 ± 0.4	SLOW	SLOW
	41	5.6 ± 1.5	4.9 ± 2.6	SLOW
	42	5.0 ± 2.4	5.6 ± 0.9	SLOW
	43	SLOW	SLOW	SLOW
	44	5.0 ± 3.6	5.6 ± 3.5	SLOW
	45	5.2 ± 2.2	5.1 ± 1.6	SLOW
	46	4.2 ± 3.3	5.0 ± 0.6	SLOW
	47	5.6 ± 1.6	SLOW	SLOW
	48	5.0 ± 0.5	SLOW	5.5 ± 0.3
	49	3.6 ± 0.2	5.8 ± 1.3	4.2 ± 0.2
	50	5.5 ± 1.5	SLOW	5.5 ± 0.3

2° Str.	Residue Number	Apo-LC8[a] PF ± Error	Nos•LC8b PF ± Error	Swa•LC8[c] PF ± Error
Strand	54	5.0 ± 0.6	4.9 ± 2.4	5.1 ± 0.5
	55	6.4 ± 2.5	SLOW	SLOW
	56	6.6 ± 0.8	SLOW	6.9 ± 0.6
	57	5.1 ± 1.6	SLOW	SLOW
	58	FAST	SLOW	SLOW
	59	4.8 ± 0.4	FAST	5.7 ± 1.0
Strand	63	FAST	FAST	5.8 ± 0.9
	64	FAST	FAST	4.9 ± 0.2
	65	FAST	4.7 ± 0.5	4.6 ± 0.3
	66	FAST	SLOW	N.A.
	67	FAST	SLOW	4.6 ± 0.3
	68	FAST	7.2 ± 1.6	4.2 ± 1.7
Loop	69	FAST	5.2 ± 0.9	N.A.
	70	5.0 ± 1.1	4.0 ± 0.5	FAST
	71	FAST	FAST	FAST
Strand	72	5.1 ± 0.3	6.0 ± 2.5	6.4 ± 0.3
	73	5.1 ± 0.2	SLOW	6.5 ± 1.7
	74	4.9 ± 1.9	SLOW	SLOW
	75	4.8 ± 0.8	SLOW	SLOW
	76	5.2 ± 1.6	5.2 ± 2.6	SLOW
	77	5.0 ± 0.8	4.8 ± 2.5	5.8 ± 0.8
Loop	78	FAST	3.4 ± 0.2	4.3 ± 0.1
	79	FAST	5.4 ± 1.0	FAST
	80	FAST	5.1 ± 0.4	5.4 ± 0.2
Strand	81	FAST	4.4 ± 0.4	3.2 ± 0.1
	82	N.A.[f]	SLOW	SLOW
	83	4.1 ±0.2	2.9 ± 0.3	SLOW
	84	5.4 ± 2.1	4.2 ± 1.7	SLOW
	85	4.9 ± 3.9	SLOW	SLOW
	86	N.A.	2.5 ± 0.8	SLOW
	87	3.5 ± 0.4	SLOW	SLOW
	88	FAST	3.7 ± 0.6	4.1 ± 0.8

[a] Data available at /home/justin/nmr-data/jh-an.
[b] Data available at /home/justin/nmr-data/jh-ao.
[c] Data available at /home/justin/nmr-data/jh-aq.
[d] Exchange rate too fast to measure.
[e] Exchange rate too slow to measure.
[f] Peak overlap prohibits exchange rate measurement.

Appendix 4

Protocol for growth and purification of His-SUMO-IC$_{212-260}$

Buffers to prepare:

1 L TB media, Lysis Buffer, Affinity Buffer with 0, 10 and 350 mM imidazole, Affinity Buffer with 8 M Urea, 5% Acetonitrile and .1% TFA in H_2O (Buffer A) and 95% Acetonitrile and .1% TFA in H_2O (Buffer B).

Day 1:

i) Streak LB with Kanomyacin ("Kan") plate using His-SUMO-$IC_{212-260}$ glycerol stock in BL21DE3 cells with a pet15da (Kan+) expression vector. Place in oven at 37 °C overnight ("o/n", 12-15 h).

ii) Prepare 1 L TB media either in a single 4 L flask or 500 ml split between two 2 L flasks, autoclave 35 m liquid.

Day 2:

i) Select a colony from the plate and inoculate 10 ml LB with 0.5 mg of Kan (500 μg/ml final concentration). Grow at 37 °C at 200 rpm o/n.

Day 3:

i) Add Kan to your 1 L TB media to a final concentration of 50 μg/ml and set aside 0.5 ml of media for a sample blank.

ii) Spin down the 10 ml culture (4000 rcf for 15 m), pour off supernatant into ethanol to kill non-pelleted cells.

iii) Dissolve cells in 1 ml of the fresh TB media and inoculate the 1 L TB.

iv) Grow at 37 °C, 200 rpm until the optical density ("OD") is ≅ 0.6 at 600 nm. Take 1 ml of sample for "pre-induction sample" (Appendix Figure A4.1).

v) Induce protein production by adding IPTG to a final concentration of 0.8 mM. Grow for 4 h.

vi) Harvest cells by placing 1 L TB media in centrifuge bottle, spin at 4000 rpm (rcf unknown for the 1 L bucket centrifuge) for 30 m.

vii) Pour off supernatant into 2 L beaker, add bleach to kill non-pelleted cells. Save cell pellet at -80 °C.

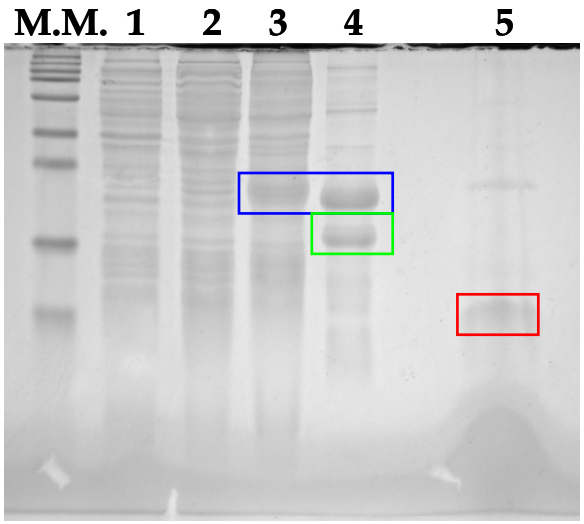

Figure A4.1: SDS-PAGE analysis of $IC_{212-260}$ purification. Gel labels are Protein plus molecular marker (M.M.), pre induction (1), supernatant (2), pellet with band corresponding to Sumo outlined in blue (3), post Ni-column cleaning with incomplete Sumo cleavage product in outlined in green (4), and pure $IC_{212-260}$ outlined in red after C-18 purification (5).

Day 4:

i) Resuspend cells in “Lysis Buffer” (see Barbar lab recipes) using 200 ml per 1 L of media grown. Use the vortex to resuspend and homogenize cells.

ii) Make sure the resuspended cells are in a plastic beaker, a glass beaker may break during cell sonication (next step).

iii) Add PMSF to 1:400 (PMSF:lysis buffer) and sonicate your cells using a duty cycle of 60 and an output control of 6 for 2 m. Make sure to turn the resuspended cells during sonication so that lysis is homogenous.

iv) Spin your sonicated sample at 14000 rcf for 30 m to pellet debris.

v) Save “supernatant”, and resuspend “pellet” in “Affinity Buffer” (see Barbar lab recipes) containing 8 M Urea and no imidazole.

vi) Spin your sonicated sample at 14000 rcf for 45 m to pellet debris.

vii) While the pellet is spinning, prepare the nickel column beads by washing with Affinity Buffer using 10 ml affinity buffer per 1 ml of column volume. Allow beads to go dry, transfer dry beads to a beaker large enough to hold the supernatant from your pellet resupension.

viii) Apply your supernatant to the dry nickel beads making sure to break up any clumps of dry beads (try swirling or shaking), add a stir bar to mix bead/supernatant for 30 m.

ix) Apply the beads to the column using a Pasteur pipette. Wash the beads with 10 ml of 8 M Urea Affinity Buffer, then 10 progressive mixtures of 1ml decreasing 8 M Urea Affinity and 1ml increasing Affinity Buffer at final volume of 10 ml (e.g. 9:1, 8:2… 1:9, 0:10).

x) Elute the protein off the column by adding 4 times your bed volume of 350 mM imidazole containing Affinity Buffer. Take a 0.05 ml sample for “pre-cleavage sample”.

xi) Add 0.02 ml of ULP1-Sumo protease stock and let cleavage reaction occur at room temperature for ≈ 1 h.

xii) Load half of your sample onto the C-18 column. $IC_{212-260}$ elutes at 36-39 m followed closely by an impurity (Appendix Figure A4.2).

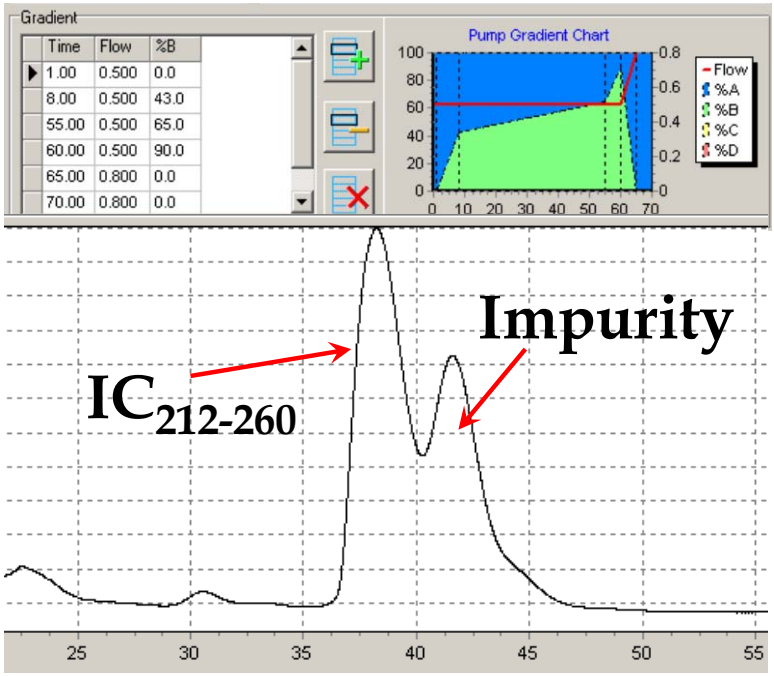

Figure A4.2: Elution profile for $IC_{212\text{-}260}$ on a C-18 column. Protocol for time, flow rate, and percent acetonitrile (top panel) with resultant elution profile for $IC_{212\text{-}260}$ on a C-18 column (bottom panel).

Appendix 5

ITC data for IC_{TT} binding to Tctex1

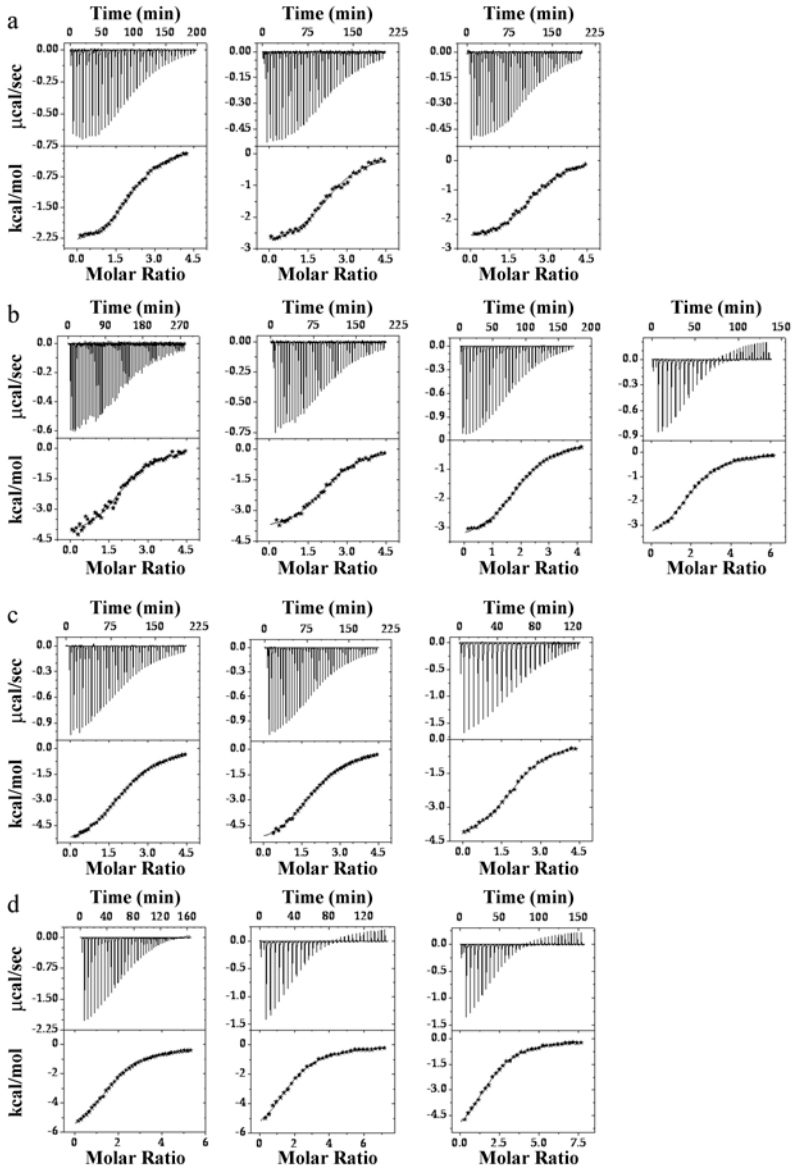

Figure A5.1: Representative ITC data for IC_{TT} binding to Tctex1. Thermograms (top panels) and binding isotherms (bottom panels) are shown for the titration of Tctex1 into IC_{TT} at a) 20 °C, b) 25 °C, c) 30 °C, and d) 35°C. Solid lines correspond to the non-linear least squares fit for an **A + B → AB** binding model. Data were collected in 50 mM sodium phosphate, 50 mM sodium chloride, pH 7.5.

Table A5.1: Thermodynamic association parameters for IC_{TT} binding to Tctex1 in 50 mM sodium phosphate, 50 mM sodium chloride, pH 7.5[a].

Temperature (K)	K_D (μM)	"c" value (K_A x [cell])	ΔG° (kcal/mol)	ΔH° (kcal/mol)	-TΔS° (kcal/mol)
293.15	9.3 ± 4.5	5	-6.7 ± 0.5	-2.7 ± 0.2	-4.0 ± 0.2
298.15	11.0 ± 4.5	4	-6.8 ± 0.4	-3.9 ± 0.4	-2.8 ± 0.2
303.15	13.2 ± 4.4	4	-6.8 ± 0.2	-5.5 ± 0.7	-1.3 ± 0.5
308.15	27.1 ± 9.0	2	-6.4 ± 0.3	-6.9 ± 0.3	0.5 ± 0.1

[a]Average values are reported with error estimated as the standard deviation of replicates (see Appendix Figure A5.1). The average binding stoichiometry (n) was 2.11 ± 0.20 over all experiments. All data were fit to one monomer of either light chain binding to a single IC chain.

Table A5.2: Thermodynamic association parameters for Tctex1 binding to the IC_{TT}•Tctex1 complex in 50 mM sodium phosphate, 50 mM sodium chloride, pH 7.5[a].

Temperature (K)	K_D (μM)	ΔG° (kcal/mol)	ΔH° (kcal/mol)	-TΔS° (kcal/mol)
293.15	7.8 ± 3.8	-6.9 ± 0.5	-0.5 ± 0.1	-6.3 ± 0.3
298.15	12.5 ± 5.1	-6.7 ± 0.4	-1.0 ± 0.1	-5.7 ± 0.4
303.15	15.9 ± 5.3	-6.7 ± 0.4	-1.6 ± 0.2	-5.0 ± 1.9
308.15	50.8 ± 16.9	-6.1 ± 0.2	-2.8 ± 0.1	-3.3 ± .04

[a]Average values are reported with error estimated as the standard deviation of replicates (see Appendix Figure A5.1).